

FRACTURE TOUGHNESS OF PORTLAND CEMENT CONCRETES

by

Dan Naus  
James Lott

Prepared as a Part of an Investigation

Conducted by

THE ENGINEERING EXPERIMENT STATION

UNIVERSITY OF ILLINOIS

In Cooperation with

THE DIVISION OF HIGHWAYS

STATE OF ILLINOIS

and

BUREAU OF PUBLIC ROADS

U. S. DEPARTMENT OF TRANSPORTATION

Project IHR-92

THE CONTROL OF CRACKING OF CONCRETE

February 1968

## ACKNOWLEDGMENTS

This study was conducted as a part of the research under the Illinois Cooperative Highway Research Program Project IHR-92, "The Control of Cracking of Concrete." The project has been undertaken by the Engineering Experiment Station of the University of Illinois, in cooperation with the Illinois Division of Highways of the State of Illinois and the U. S. Department of Transportation, Federal Highway Administration, Bureau of Public Roads.

On the part of the University, the work covered by this report was carried out under the general administrative supervision of W. L. Everitt, Dean of the College of Engineering, R. J. Martin, Director of the Engineering Experiment Station, T. J. Dolan, Head of the Department of Theoretical and Applied Mechanics, and Ellis Danner, Director of the Illinois Cooperative Highway Research Program and Professor of Civil Engineering.

On the part of the Division of Highways of the State of Illinois, the work was under the administrative direction of Virden Staff, Chief Highway Engineer and J. E. Burke, Engineer of Research and Development.

Technical advice was provided by a Project Advisory Committee consisting of the following personnel:

Representing the Illinois Division of Highways:

J. E. Burke, Engineer of Research and Development

R. L. Duncan, Field Engineer

W. Griffin, Structural Design Engineer

Representing the University of Illinois:

C. E. Kesler, Professor of Theoretical and Applied Mechanics  
and Civil Engineering

G. M. Sinclair, Professor of Theoretical and Applied Mechanics

J. L. Lott, Assistant Professor of Theoretical and Applied Mechanics  
and David Raecke, Research Assistant in the Department of Theoretical and Applied Mechanics, served as Chairman and Secretary, respectively, of the Project Advisory Committee.

The opinions, findings, and conclusions expressed in this publication are those of the authors and not necessarily those of the State of Illinois, Division of Highways, or the U. S. Department of Transportation, Federal Highway Administration, Bureau of Public Roads.

## TABLE OF CONTENTS

	<u>Page</u>
1. INTRODUCTION. . . . .	1
1.1 General. . . . .	1
1.2 Object . . . . .	1
1.3 Scope. . . . .	1
1.3.1 Experimental Program. . . . .	1
1.3.2 Analytical Study. . . . .	1
1.3.3 Application . . . . .	1
1.4 Notation . . . . .	2
2. FRACTURE MECHANICS. . . . .	4
2.1 Linear-Elastic Fracture Mechanics. . . . .	4
2.1.1 General . . . . .	4
2.1.2 Crack Extension Behavior. . . . .	4
2.1.3 Elastic Solution to Stress Field Associated with a Crack. . . . .	5
2.1.4 Crack Extension Force . . . . .	6
2.2 Inelastic Deformation in Region of Crack Tip . . . . .	7
2.2.1 Strip-Yield Zone Concept. . . . .	7
2.2.2 Rice's Rigid-Plastic Strip Model. . . . .	7
2.3 Applications of Fracture Mechanics to Concrete . . . . .	8
3. EXPERIMENTAL INVESTIGATION. . . . .	11
3.1 General. . . . .	11
3.2 Materials. . . . .	11
3.2.1 Cement. . . . .	11
3.2.2 Aggregate . . . . .	11
3.2.3 Admixtures. . . . .	11
3.2.4 Paste, Mortar, and Concrete Mixes . . . . .	11
3.3 Description of Specimens . . . . .	12
3.3.1 Paste and Mortar Series . . . . .	12
3.3.2 Concrete Series . . . . .	12
3.4 Fabrication and Curing . . . . .	12
3.4.1 Mixing. . . . .	12
3.4.2 Casting . . . . .	13
3.4.2.1 Paste and Mortar Series. . . . .	13
3.4.2.2 Concrete Series. . . . .	13



	<u>Page</u>
3.4.3 Curing. . . . .	13
3.5 Equipment. . . . .	14
3.6 Procedure. . . . .	14
4. EXPERIMENTAL RESULTS. . . . .	16
4.1 Strengths and Dynamic Modulus of Elasticity. . . . .	16
4.2 Test Data for Flexural Specimens . . . . .	16
4.2.1 Load-Deformation Curves . . . . .	16
4.2.2 Loads . . . . .	16
4.2.3 Stress Intensity Factor . . . . .	16
5. ANALYSIS AND DISCUSSION OF EXPERIMENTAL RESULTS . . . . .	18
5.1 Behavior of Fracture Toughness Specimens . . . . .	18
5.2 Stress Intensity Factor. . . . .	18
5.2.1 Fracture Toughness. . . . .	18
5.2.2 Initiation of Stable Crack Propagation. . . . .	19
5.3 Effect of Concrete Parameters on $\overline{K}_C^I$ . . . . .	19
5.3.1 Water-Cement Ratio. . . . .	19
5.3.2 Air Content . . . . .	20
5.3.3 Curing Time and Curing Conditions . . . . .	20
5.3.4 Fine Aggregate Content and Gradation. . . . .	21
5.3.5 Gravel Content, Gradation, and Type . . . . .	22
6. RIGID-PLASTIC CRACKED STRIP MODEL . . . . .	23
6.1 Development of Model . . . . .	23
6.2 Analysis of Model. . . . .	23
6.3 Model for Fracture of Portland Cement Paste. . . . .	24
6.3.1 Strength of Paste . . . . .	24
6.3.2 Model for Fracture. . . . .	24
7. SUMMARY AND CONCLUSIONS . . . . .	27
7.1 Object and Scope . . . . .	27
7.2 Experimental Results . . . . .	27
7.3 Model for Fracture of Cement Paste . . . . .	28
7.4 Significance . . . . .	28
REFERENCES. . . . .	30
TABLES. . . . .	32
FIGURES . . . . .	52



## 1. INTRODUCTION

### 1.1 General

Concrete is a heterogeneous material composed of a matrix of hydrated portland cement paste and fine and coarse aggregate. Engineering properties of the concrete are closely related to the properties of the cement paste matrix. Concrete and paste both behave as brittle materials and their tensile and compressive properties depend on fracture mechanisms.

Several applications of fracture mechanics have been made to mortars and concretes (1-6)\*. In each instance the material was assumed to be homogeneous and a material resistance property was evaluated experimentally. Interaction of matrix and aggregates affects the stress field in the region of the crack tip in concrete (4).

### 1.2 Object

The objective of this investigation is to develop a better understanding of the fracture mechanism of concrete and to determine the concrete parameters effect on concrete fracture toughness.

### 1.3 Scope

#### 1.3.1 Experimental Program

The fracture toughness of several pastes, mortars, and concretes was determined by flexural tests of specimens containing flaws of various depths cast at the center of the tensile surface. Variables in the investigation were the water-cement ratio, sand-cement ratio, gravel-cement ratio, degree of hydration (age of specimens at testing), curing conditions, air content, sand gradation, and gradation and type of coarse aggregate.

#### 1.3.2 Analytical Study

Several stress distributions in the region of the crack tip of a rigid-plastic cracked strip model were assumed to yield approximations for inelastic phenomena at the crack tip. The experimental results were then correlated to the model.

#### 1.3.3 Application

The effect of concrete parameters on the fracture toughness of

---

\*Numbers in parentheses refer to entries in the References.

concrete was related to mix design procedures so that a high or low material resistance to propagation of a flaw could be attained.

#### 1.4 Notation

$B$	= flexure specimen width
$E$	= Young's modulus, also the energy of the system
$G$	= rate of release of energy with respect to increasing crack surface
$G_c$	= critical energy-release rate at the onset of rapid crack propagation
$K$	= stress intensity factor at the tip of a crack
$K_c$	= critical stress intensity factor at the onset of rapid, unstable crack propagation
$K_e$	= elastic stress intensity factor at the tip of a crack
$K_i$	= stress intensity factor at the initiation of slow, stable crack propagation
$K', K'_c, K'_i$	= effective stress intensity factors in the matrix of a heterogeneous material that is assumed to be homogeneous
$M$	= applied bending moment
$P$	= applied load
$P_i$	= load at initiation of slow crack propagation
$P_{max}$	= maximum applied load
$a$	= crack length of an edge-cracked specimen or half the crack length of a center-cracked specimen
$r$	= polar coordinate
$r_y$	= plastic zone radius
$s_o$	= equilibrium spacing between gel particles in the absence of applied stress
$w$	= flexure specimen depth
$\alpha$	= stress distribution constant
$\gamma_s$	= surface energy
$\Delta a$	= incremental change in crack surface

$\Delta E$	= incremental release of energy
$\delta_z$	= displacement component in z-direction
$\theta$	= polar coordinate
$\mu$	= Poisson's ratio
$\sigma$	= nominal stress
$\sigma_c$	= theoretical cohesive strength
$\sigma_{xx}$	= stress normal to y-z plane in x-direction
$\sigma_{yy}$	= stress normal to x-z plane in y-direction
$\sigma_{zz}$	= stress normal to x-y plane in z-direction
$\sigma_{th}$	= threshold stress for yielding or microcracking
$\tau_{xy}$	= shear stress on plane perpendicular to x-axis in y-direction
$\omega$	= length of plastic zone



## 2. FRACTURE MECHANICS

### 2.1 Linear-Elastic Fracture Mechanics

#### 2.1.1 General

Linear-elastic fracture mechanics is a study of stress and displacement fields near the tip of a flaw in an ideal, homogeneous, elastic material at the onset of fracture. Its concepts are most applicable to brittle materials in which the inelastic region near the crack tip is small compared to specimen and flaw dimensions so that elastic stress field equations provide a good approximation (7, 8, 9). The stress and displacement fields can be expressed in terms of a stress intensity factor,  $K$ , which is a function of load and geometry only.

As the ratio of plastic zone size to specimen dimensions increases, the inelastic region becomes significant and adjustments must be made to correct for effects of plastic strains adjacent to the crack tip (10, 11, 12). An exact solution to correct for the zone of yielding is presently unknown; however, an approximate solution can be attained by assuming a crack tip extension to the central portion of the inelastic region and solving the problem with elastic stress field equations for the increased crack length.

#### 2.1.2 Crack Extension Behavior

Fracture occurs by extension of a pre-existing flaw in a material. The importance of a specific size flaw depends on the nominal stress normal to the crack and the fracture toughness of the material. It should be noted that the observed fracture phenomena is a function of the type of load system. In a soft system the load drops off slowly and the crack speed approaches a limiting value of approximately 0.5 the shear wave velocity of the material. This condition of maximum crack speed is generally accompanied by crack division tendencies; i.e., forking. With a hard loading system the load diminishes rapidly as the crack extends and a condition of crack arrest may develop abruptly.

Crack extension occurs in three stages: subcritical or slow extension, critical (transition from slow to fast crack speed), and running (rapid crack propagation). Subcritical crack extension is very slow and is measured as an incremental length change per second for static loads and an incremental length change per cycle for fatigue

loading. In most situations subcritical crack extension is considered as a steady state phenomena in which the crack speed responds directly to applied stress and crack length. Its main significance is that slow crack extension progressively increases the crack size toward a critical size and the ensuing rapid propagation. At critical crack extension there is an abrupt transition from a slowly propagating crack to a rapidly running crack that responds directly to instantaneous crack length and load. With increasing crack speed the crack surface separation also increases, and a maximum load point followed by a drop in load results.

Primary interest is centered on the transition from slow to fast crack extension. The elastic fields associated with the crack tip at this transition are used to characterize the material resistance to rapid crack extension and rupture.

### 2.1.3 Elastic Solution to Stress Field Associated with a Crack

For a material which is a homogeneous, isotropic, elastic solid the elastic stresses in the x-y plane at a point  $(r, \theta)$  in the region of the crack tip for either plane stress or plane strain conditions are (13, 14):

$$\begin{aligned}\sigma_{xx} &= \frac{K}{\sqrt{2\pi r}} \cos \frac{\theta}{2} \left[ 1 - \sin \frac{\theta}{2} \sin \frac{3\theta}{2} \right] \\ \sigma_{yy} &= \frac{K}{\sqrt{2\pi r}} \cos \frac{\theta}{2} \left[ 1 + \sin \frac{\theta}{2} \sin \frac{3\theta}{2} \right] \\ \tau_{xy} &= \frac{K}{\sqrt{2\pi r}} \sin \frac{\theta}{2} \cos \frac{\theta}{2} \cos \frac{3\theta}{2} .\end{aligned}\tag{1}$$

The stress intensity factor,  $K$ , a function of loading and geometry, denotes the stress and displacement fields in the region of the crack tip. At the onset of unstable crack growth the stress intensity factor is evaluated as a critical value,  $K_c$ , which is assumed to be a material property called the fracture toughness; i.e., material's resistance to propagation of an existing flaw.

At the crack tip a stress singularity exists in the elastic solution for the stresses. Since an infinite stress cannot exist in a real material, an inelastic deformation such as yielding or microcracking must occur to deform the material at the crack tip; i.e. blunt the crack tip, and provide stress relief. Thus the elastic stress field

equations provide only approximate solutions for the stress field in a real material.

Different phenomena result when a plane strain condition  $\{\sigma_{zz} = \mu (\sigma_{xx} + \sigma_{yy}); \delta_z = 0\}$  develops instead of a plane stress condition  $\{\sigma_{zz} = 0\}$ . The lateral restraint that develops with plane strain produces a biaxial stress condition at the critical point of fracture. For steels the lateral restraint reduces the zone of inelastic deformation to yield a minimum value for the material's fracture toughness. In such a situation where the region of yielding is small compared to specimen and flaw dimensions, an estimate of the plastic zone radius,  $r_y$ , is given by (10, 11, 15):

$$r_y = \frac{1}{2\pi} \left[ \frac{K}{\sigma_y} \right]^2 \quad (2)$$

where  $\sigma_y$  is the yield strength (Fig. 1). By using this approximation to extend the crack tip to the center of the region of inelastic deformation and relocate the y-axis to  $y'$ , the elastic solution for the stresses in the region of the crack tip will yield good approximations because the plastic region is confined within an elastic field.

#### 2.1.4 Crack Extension Force

In the Griffith Theory (16) of fracture of brittle materials it is assumed that the material contains small flaws of various dimensions. Centering interest on the largest of these flaws, Griffith reasoned that fracture would occur when the release of elastic strain energy per increment of crack area was equal to the surface energy over the same increment of area. However, introduction of a work rate to account for plastic deformation is difficult and leads to an accompanying lack of accuracy.

The rate of release of elastic strain energy,  $G^*$ , provides a single parameter, entirely analogous to the stress intensity factor,  $K$ , for characterizing the fracture criterion. The following relationship

---

\*  $G$  is the release of energy  $\Delta E$  supplied by a virtual crack extension  $\Delta a$  necessary to furnish the energy requirements of the crack surface  $\Delta a$  as  $\Delta a$  approaches zero; i.e.,  $\lim_{\Delta a \rightarrow 0} \frac{\Delta E}{\Delta a}$ ;  $G$  is the determination of  $G$  at the onset of rapid crack propagation.



exists between the two parameters (17):

$$\begin{aligned} G E &= K^2 && \text{(plane stress)} \\ G E &= K^2 (1 - \mu^2) && \text{(plane strain)} \end{aligned} \quad (3)$$

for isotropic, homogeneous, elastic materials.

## 2.2 Inelastic Deformation in Region of Crack Tip

As the inelastic region increases there is an associated redistribution of stress which increases the error in the elastic stress intensity factor. Although an exact solution for the influence of inelastic phenomena on stress and deformation fields at the crack tip is presently unsolved, an estimate of the inelastic zone size and deformation in the region of the crack tip can be obtained by a rigid-plastic strip model (18) based on hypotheses of Dugdale (19) and Barenblatt (20).

### 2.2.1 Strip-Yield Zone Concept

Stresses near a crack are frequently analyzed by solving the stress problem without the crack and then superimposing a solution that contains forces at the crack plane just sufficient to restore free-surface conditions. Using an approach of this type and restricting the inelastic zone to a line inelastic region extending from the crack tip ( $\theta = 0$ ,  $r > a$ ), Dugdale was able to develop a theory of crack equilibrium. Dugdale's hypothesis (19) was based on experimental observations and measurements of fracture surfaces in thin metal sheets (plane stress) where it was noted that yielding occurred on a narrow line in front of the crack. In Dugdale's model, the force system consisted of a constant tensile stress, the tensile yield strength, across the tensile yield zone. Barenblatt (21) proposed a concept in which there always exists within the crack region a series of crack closure forces; i.e., molecular forces of cohesion. These cohesive forces interact because of the close proximity of the crack surfaces. Assuming that the cohesive forces act only on an edge region of the crack surface that is small compared to total crack area, and that the shape of the edge region of the crack is constant for maximum resistance to crack growth in a material, Barenblatt was able to eliminate the stress singularity at the crack tip.

### 2.2.2 Rice's Rigid-Plastic Strip Model

Response to loadings of a cracked elastic-plastic plane can be

approximated by a rigid-plastic strip model (18) similar to the models of Dugdale and Barenblatt. The model consists of two elastic half planes joined together along a strip of rigid plastic material with a void in the strip material simulating a crack (Fig. 2). The strip is rigid plastic in that when a y-direction normal stress,  $\sigma_{yy}$ , acts on the strip the material does not extend or contract in the y-direction if  $|\sigma_{yy}| < \sigma_y$ ; however, the strip will be capable of unlimited deformation if  $|\sigma_{yy}| = \sigma_y$ . It is assumed that the material offers no resistance to extension or contraction in the x-direction.

Rice modified this model by removing the zone of plastic deformation and superpositioning stresses of yield strength magnitude,  $\sigma_y$ , which the plastic material induces on the elastic half planes, on the region of plastic deformation. Plastic zone size was then determined by the condition that stresses should be bounded at outer edges of the interface. Thus the stress intensity factor due to external loadings and the stress intensity factor due to yield strength loadings should sum to zero.

The rigid-plastic strip model provides a yielding type behavior ahead of the crack which can be used to estimate the plastic zone size and inelastic phenomena in the region of the crack tip. Only an estimate is obtained because the line inelastic region does not take inelastic deformations into account.

### 2.3 Applications of Fracture Mechanics to Concrete

Several applications of linear-elastic fracture mechanics to mortars and concretes have been made (1-6). Concrete, being a poly-phase material, has a more complex fracture process than an ideally brittle material. Fracture of the concrete can occur by fracture of the cement paste, fracture of the aggregate, failure of the bond between cement paste and aggregate, or any combination of these mechanisms.

Kaplan (1) was the first to apply fracture mechanics to concrete when he investigated one mortar and two concretes. An analytical and experimental approach, both neglecting slow crack growth prior to fracture, were used to evaluate the critical strain energy release rate,  $G_c$ . The results obtained by Kaplan indicated that  $G_c$  was influenced by the mix proportions, specimen dimensions, and loading.

Glucklich (3) modified the Griffith-Irwin theory to introduce a non-linear relationship to represent the energy requirements to propagate a crack in a heterogeneous material. Such an alteration is necessary because each phase of the material through which the crack propagates has distinct  $G_c$  values; i.e., in concrete the cement paste, fine aggregate, and coarse aggregate have discrete values of  $G_c$ . Two types of crack growth are present in concrete: an initial stage in which the rate of release of strain energy with slow crack extension is so low that any sudden increase in energy requirement, such as encountering an aggregate, will stabilize the propagating crack; and a final stage where the energy release rate with rapid crack propagation is of such magnitude that any energy demand encountered will be supplied so that an unstable situation results. Glucklich applied this approach to mortars under repeated loading and suggested study of the parameter  $\sigma^2 a$  ( $\sigma$  is the nominal stress and  $a$  is the critical flaw depth). This parameter is proportional to  $G_c$  and is independent of the fatigue life and stress applied to a specimen. Results obtained by Glucklich indicated that the values of  $G_c$  for unnotched beams subjected to repeated loading were about 7.5 per cent lower than those obtained for static loading, while the notched beams subjected to repeated loading yielded  $G_c$  values 10.0 per cent larger than those obtained from static tests.

Lott and Kesler (4) conducted a study to develop a hypothesis for propagation of cracks in plain concrete and to compare the hypothesis to results of an experimental investigation of crack propagation in several mortars and concretes. It was suggested that the critical stress intensity factor for plain concrete was derived from the stress intensity factor of the cement paste and the crack arresting mechanism developed by the heterogeneity of the concrete. Since the critical stress intensity factor for the paste was a material constant, variations in the critical stress intensity factor for the concrete were reflected through the arresting function. The effects of several concrete parameters (water-cement ratio, sand-cement ratio, and gravel-cement ratio) on the fracture toughness of the concrete were evaluated.

For the range of variables investigated, it was found that: the critical stress intensity factor was independent of water-cement ratio for three mortars and for various concretes where the aggregate



percentages remained constant; the critical stress intensity factor was independent of fine aggregate percentage for three mortars with the same water-cement ratio; the critical stress intensity factor varied directly with coarse aggregate content for concretes with the same water-cement ratio and fine aggregate content; and the critical stress intensity factor for concrete was found to be approximately 20.0 per cent greater than that for a mortar with the same water-cement ratio and fine aggregate content.

### 3. EXPERIMENTAL INVESTIGATION

#### 3.1 General

The fracture toughnesses of several pastes, mortars, and concretes were determined by flexural tests of specimens containing flaws of various depths cast at the center of the tensile surface. The parameters investigated were: water-cement ratio, air content, and degree of hydration for the pastes; water-cement ratio, air content, degree of hydration, curing conditions, sand-cement ratio, and sand gradation for the mortars; and water-cement ratio, air content, degree of hydration, curing conditions, sand-cement ratio, gravel-cement ratio, and gradation and type of coarse aggregate for the concretes. Limitations were placed on the range of parameters investigated by the tendency of pastes and mortars to bleed and of the concretes with high percentages of aggregate to be stiff and difficult to compact.

#### 3.2 Materials

##### 3.2.1 Cement

Type I portland cement was used in all mixes. The cement was purchased in paper bags from a local dealer and was stored in the laboratory for use during the investigation.

##### 3.2.2 Aggregate

The sand used in all mixes was Wabash River sand from near Covington, Indiana. It was graded and then recombined into the percentages by weight retained on the sieve sizes as shown in Table I.

Two gravels were used in the series of concrete specimens: a Wabash River gravel from near Covington, Indiana, and a crushed limestone which was obtained from a local dealer. The gravels were graded and recombined into the percentages by weight retained on the sieve sizes as shown in Table II.

##### 3.2.3 Admixtures

The air-entraining agent used was a proprietary compound consisting of an aqueous solution of salts of sulfonated hydrocarbons containing a catalyst.

##### 3.2.4 Paste, Mortar, and Concrete Mixes

Properties of the mixes are given in Table III.

### 3.3 Description of Specimens

#### 3.3.1 Paste and Mortar Series

Nominal dimensions of the flexural specimens were 2 by 2 by 14 in. A flaw was cast at the center of the tensile surface of the specimens. The flaw was formed with a strip of teflon-coated fiberglass cloth with a thickness of 0.003 in. Three nominal flaw depths were used, 1/4 in., 1/2 in., and 1 in. Variation in the nominal dimensions occurred during fabrication. Actual dimensions of the specimens were measured after testing.

Prismatic specimens of the same nominal dimensions as the flexural specimens were used to determine the dynamic modulus of elasticity and the modulus of rupture. Compressive strength was determined with 2-in. cubes, and splitting-tensile strength was determined with 2 by 4-in. cylinders for the paste series and 4 by 8-in. cylinders for the mortar series.

#### 3.3.2 Concrete Series

Nominal dimensions of the flexural specimens were 4 by 4 by 12 in. A flaw was cast at the center of the tensile surface of the specimens. The flaw was formed with a strip of teflon-coated fiberglass cloth with a thickness of 0.003 in. Three nominal flaw depths were used, 1/2 in., 1 in., and 1-1/2 in. Variations in the nominal dimensions of the specimens occurred during fabrication. Actual dimensions of the flexural specimens were measured after testing.

Prismatic specimens of the same nominal dimensions as the flexural specimens were used to determine the dynamic modulus of elasticity and the modulus of rupture. Splitting-tensile strength was determined with 4 by 8-in. cylinders, and compressive strength was determined by a modified cube test (ASTM C116-65T) on one-half of the broken flexural specimen.

### 3.4 Fabrication and Curing

#### 3.4.1 Mixing

The mix volume was approximately 1.4 ft<sup>3</sup> for the pastes and mortars and 1.8 ft<sup>3</sup> for the concretes. A two cubic foot capacity horizontal pan mixer was used. The dry ingredients were blended for one minute before water was added to the mix; mixing was then continued for



three minutes after the water was added. Air-entraining agents, when used, were added to the mix water.

### 3.4.2 Casting

#### 3.4.2.1 Paste and Mortar Series

The 2 by 2 by 14 in. prisms were cast on their side in steel molds. A total of twenty flexural specimens was cast for each series. The molds were filled in one lift and the specimens were compacted on a vibrating table.

The 2-in. cubes were cast in standard brass molds and were compacted on a vibrating table.

The cylinders for the splitting-tensile strength tests were cast in standard steel molds set on steel baseplates. The 2 by 4-in. paste cylinders were compacted by rodding and vibration; and, the 4 by 8-in. mortar cylinders were compacted by rodding only.

The exposed surface of all specimens was trowelled smooth immediately after casting.

#### 3.4.2.2 Concrete Series

The 4 by 4 by 12 in. prisms were cast on their side in plywood forms. A total of eight flexural specimens was cast for each series. The forms were filled in one lift and the specimens were compacted on a vibrating table.

The cylinders for the splitting-tensile strength tests were cast in the same manner as for the mortar series.

The exposed surface of all specimens was trowelled smooth immediately after casting.

### 3.4.3 Curing

About two to four hours after casting, all specimens were covered with wet burlap and plastic sheeting to prevent the loss of moisture. At approximately 24 hours after casting the specimens were removed from their molds and stored in a moisture room for curing at 100 per cent relative humidity. The specimens were removed from the moisture room at various ages and were stored in water until they were tested.

A few series were initially cured in the moisture room and then removed and placed in a controlled environment room (70° F and 50

per cent relative humidity) for further curing. These specimens were tested in laboratory air within one hour of removal from the controlled environment.

### 3.5 Equipment

A hydraulic testing machine was used for the flexural tests. The test setup for the paste and mortar series is shown in Fig. 3, and for the concrete series in Fig. 4. The load was transmitted from the base of the testing machine to a loading plate through a steel ball. The loading plate divided the load into two forces that were transmitted to the quarter-points of the specimen. The test setup was designed to prevent the development of axial and torsional stresses in the specimen.

The loading plate also acted as a dynamometer to measure the load applied to the specimen. Four electric strain gages were mounted on the loading plate to measure longitudinal strains, two on the tensile surface and two on the compressive surface. The tensile gages were connected in opposite arms of a four-arm bridge.

The elongation of the tensile surface was measured with a de-former that was supported by needle-point screws. The screws were mounted on the specimen as shown in Fig. 3 for the paste and mortar series and Fig. 4 for the concrete series. Four electric strain gages, connected in a four-arm bridge were mounted on the deformer. The deformer was pre-compressed before each test by adjustment of the screws. This pre-compression was reduced as the tensile surface elongated during a test.

The response of the load plate and deformer was recorded by an electronic recorder.

### 3.6 Procedure

The deformer was calibrated before each series of tests by placing it in a super-micrometer and compressing it approximately 0.012 in. to a pseudo-zero point. The pre-compression was then reduced in increments of 0.0005 in. and the record was marked at each increment. After calibration, the deformer was placed between the needle-point screws of the first specimen and pre-compressed to a pseudo-zero point. The recorder was then zeroed for no load and the base of the testing machine was raised until the specimen came into contact with the

reactions. Load was then applied at a rate of approximately 250 lb per minute for the paste and mortar flexural specimens and 1500 lb per minute for the concrete flexural specimens until failure occurred. The recorder produced a continuous record of applied load and deformation until failure.

This procedure was repeated until all specimens in the series had been tested. After completion of the flexure tests, the deformer was recalibrated. The sonic tests for dynamic modulus of elasticity and the compression and splitting-tensile tests were conducted on the same day as the flexure tests.



#### 4. EXPERIMENTAL RESULTS

##### 4.1 Strengths and Dynamic Modulus of Elasticity

The average compressive strength, average splitting-tensile strength, average modulus of rupture, and average modulus of elasticity are given in Table IV for each series.

##### 4.2 Test Data for Flexural Specimens

###### 4.2.1 Load-Deformation Curves

A continuous record of load and deformation was made during each test. An x-y recorder plotted the deformation response against load response until failure of the specimen. Typical load-deformation curves for a paste, mortar, and concrete are presented in Fig. 5, Fig. 6, and Fig. 7, respectively.

###### 4.2.2 Loads

Maximum loads,  $P_{\max}$ , of each specimen of each test series are presented in Figures 8 to 92 as a function of the ratio of flaw depth,  $a$ , to specimen depth,  $w$ . The maximum loads correspond to the onset of unstable crack propagation; i.e. fracture.

The loads at the initiation of slow crack propagation ( $P_i$ ) are not presented for each specimen of each test series, but they are presented in Table V for each series in the form of an average stress intensity factor ( $\bar{K}_i$ ).

###### 4.2.3 Stress Intensity Factor

Brown and Srawley (8) used boundary value collocation calibrations to develop an expression for the stress intensity factor,  $K$ , for a single-edge-cracked specimen subjected to pure bending.  $K$  is a function of applied load and geometry of the specimen.

$$K = Y \frac{6Ma^{1/2}}{Bw^2} \quad (4)$$

where

$$Y = 1.99 - 2.47 (a/w) + 12.97 (a/w)^2 - 23.17 (a/w)^3 + 24.80 (a/w)^4$$

and  $a$  is flaw depth,  $w$  is specimen depth,  $M$  is applied bending moment, and  $B$  is specimen width.

The critical stress intensity factor (effective fracture toughness),  $K_{Ic}$ , for each test specimen of each test series is presented in

Figures 8 to 92 as a function of the ratio of flaw depth,  $a$ , to specimen depth,  $w$ . The average effective fracture toughness,  $\bar{K}_C^I$ , and coefficient of variation of effective fracture toughness of each series are presented in Table V.

The effective stress intensity factor at the initiation of slow stable crack propagation,  $K_I^I$ , where the load-deformation curve first deviates from linearity, was determined for the load corresponding to the point where the load-deformation curve becomes non-linear. The average effective stress intensity factor at initiation of slow crack growth,  $\bar{K}_I^I$ , and coefficient of variation of effective stress intensity factor for each series are presented in Table V.

## 5. ANALYSIS AND DISCUSSION OF EXPERIMENTAL RESULTS

### 5.1 Behavior of Fracture Toughness Specimens

The behavior of the fracture toughness specimens is illustrated by the load-deformation curves. Typical load-deformation curves are presented in Fig. 5, Fig. 6, and Fig. 7 for a paste, mortar, and concrete, respectively. These curves illustrate the stages of behavior of the concrete near the tip of the flaw (4): the linear stage\* where the cement paste matrix has no crack extension; the slow cracking stage in which stable crack propagation occurs to result in a rapid decrease in the slope of the load-deformation curve; and, the fracture stage where unstable crack propagation occurs and results in the deformation increasing without an increase in applied load.

### 5.2 Stress Intensity Factor

In the analysis it was assumed that the concrete was homogeneous and the crack depth at failure was the cast flaw depth. Since concrete is heterogeneous and the stress intensity factor is a function of the instantaneous value of the crack depth, the analysis yields an effective stress intensity factor,  $K_I'$ , which differed from the actual value.

#### 5.2.1 Fracture Toughness

The effective fracture toughness,  $K_{Ic}'$ , for concrete is based on an analysis which assumes that the concrete is homogeneous and the flaw depth at failure is equal to the cast flaw depth.  $K_{Ic}'$  is determined by substituting the bending moment at failure into Eq. 4. The value obtained represents an average value across the cross-section of the flexure specimen.

The average effective fracture toughness and coefficient of variation for each series are given in Table V. Figures 8 to 92 present the effective fracture toughness of each specimen of each series as a function of the ratio of flaw depth,  $a$ , to specimen depth,  $w$ . The horizontal line in each figure represents the mean value of effective fracture toughness.

---

\*The initial slope of the load-deformation curve is a function of elastic constants and varies inversely with flaw depth.

The mean  $\bar{K}_C'$  for pastes varies from 0.278 ksi  $\sqrt{\text{in}}$  for Series 8 to 0.407 ksi  $\sqrt{\text{in}}$  for Series 2. The coefficients of variation range from 11.9 per cent for Series 6 to 22.3 per cent for Series 2.

The mean  $\bar{K}_C'$  for mortars varies from 0.192 ksi  $\sqrt{\text{in}}$  for Series 37 to 0.514 ksi  $\sqrt{\text{in}}$  for Series 26. The coefficients of variation range from 6.9 per cent for Series 18 to 35.5 per cent for Series 37.

The mean  $\bar{K}_C'$  for concretes varies from 0.342 ksi  $\sqrt{\text{in}}$  for Series 74 to 0.702 ksi  $\sqrt{\text{in}}$  for Series 61. The coefficients of variation range from 3.5 per cent for Series 73 to 17.6 per cent for Series 84.

### 5.2.2 Initiation of Stable Crack Propagation

The effective stress intensity factor at the initiation of stable crack propagation,  $K_I'$ , where the load-deformation curve first deviates from linearity, was determined for the load corresponding to onset of the non-linear relationship between load and deformation,  $P_I$ , and specimen dimensions. The average value,  $\bar{K}_I'$ , for each series is presented in Table V.

The mean  $\bar{K}_I'$  for pastes varies from 0.125 ksi  $\sqrt{\text{in}}$  for Series 8 to 0.183 ksi  $\sqrt{\text{in}}$  for Series 2. The coefficients of variation range from 8.9 per cent for Series 7 to 29.0 per cent for Series 6.

The mean  $\bar{K}_I'$  for mortars varies from 0.115 ksi  $\sqrt{\text{in}}$  for Series 37 to 0.293 ksi  $\sqrt{\text{in}}$  for Series 33. The coefficients of variation range from 5.7 per cent for Series 14 to 27.2 per cent for Series 37.

The mean  $\bar{K}_I'$  for concretes varies from 0.187 ksi  $\sqrt{\text{in}}$  for Series 74 to 0.458 ksi  $\sqrt{\text{in}}$  for Series 81. The coefficients of variation range from 3.5 per cent for Series 67 to 27.7 per cent for Series 60.

## 5.3 Effect of Concrete Parameters on $\bar{K}_C'$

The average effective fracture toughness of the mortars was 18.0 per cent larger than the average effective fracture toughness of the pastes, as shown in Fig. 93; and, the average effective fracture toughness of the concretes was 40.0 per cent larger than the average effective fracture toughness of the mortars, as shown in Fig. 94. In general, the coefficient of variation of the effective fracture toughness was highest for the pastes and lowest for the concretes.

### 5.3.1 Water-Cement Ratio

In the paste series there was a decrease in  $\bar{K}_C'$  of 43.3 per



cent when the water-cement ratio was increased from 0.27 to 0.36 as shown in Fig. 95; while in the mortar series there was an 18.3 per cent decrease in  $\bar{K}'_C$  when the water-cement ratio was increased from 0.45 to 0.60 as shown in Fig. 96. However, in the concrete series  $\bar{K}'_C$  was independent of the water-cement ratio over the range of water-cement ratios investigated as shown in Fig. 97.

There was a decrease in the fracture toughness of the paste and mortar series with increasing water-cement ratio because the fracture toughness was dependent on the strength of the cement paste matrix which was a function of the gel-space ratio (22). With increasing water contents, the gel-space ratio decreases and this results in a reduction of strength and  $\bar{K}'_C$ . The fine aggregate of the mortar reduces the affect of water-cement ratio.

Fracture toughness of concrete was dependent on both the fracture toughness of the paste and the presence of coarse aggregate. The range of water-cement ratios did not affect the fracture toughness of the concrete because the effects of the aggregates as a crack arresting function were more significant than the effects of the water-cement ratio on the paste matrix.

### 5.3.2 Air Content

In the paste series, there was a 23.4 per cent decrease in  $\bar{K}'_C$  when the air content was increased from 2.0 per cent to 8.0 per cent as shown in Fig. 98. In the mortar series,  $\bar{K}'_C$  decreased by 19.2 per cent when the air content was increased from 3.0 per cent to 9.0 per cent as shown in Fig. 99.  $\bar{K}'_C$  decreased by 8.2 per cent when the air content in the concrete was increased from 2.0 per cent to 12.0 per cent as shown in Fig. 100.

Increasing the air content of the matrix results in a decrease in effective fracture toughness because of a reduced matrix strength. This decrease is not as significant for concretes as pastes or mortars because of the aggregate arresting phenomenon.

### 5.3.3 Curing Time and Curing Conditions

In the paste series,  $\bar{K}'_C$  for 28 days moist cure was 6.5 per cent greater than  $\bar{K}'_C$  for 6 days moist cure as shown in Fig. 101. For the mortar series there was a 47.5 per cent increase in  $\bar{K}'_C$  when the length of moist cure was increased from 3 days to 90 days as shown in

Fig. 102.  $\bar{K}'_C$  increased 54.2 per cent when the length of moist cure was increased from 3 days to 28 days for concrete using a river gravel coarse aggregate; however, the increase in  $\bar{K}'_C$  was only 7.7 per cent when the length of moist cure was increased from 28 days to 90 days as shown in Fig. 103. When a crushed limestone coarse aggregate was used,  $\bar{K}'_C$  increased 23.0 per cent with an increase in moist cure from 3 days to 28 days; however, there was no change in  $\bar{K}'_C$  when the length of moist cure was increased from 28 days to 90 days as shown in Fig. 103.

There was a 4.5 per cent decrease in  $\bar{K}'_C$  of the mortar series when the length of moist cure was increased with an accompanying decrease in length of air cure (total curing period of 29 days) as shown in Fig. 104. In the concrete series there was no definite relationship between  $\bar{K}'_C$  and an increase in length of moist cure with an accompanying decrease in length of air cure (total curing period of 90 days) as shown in Fig. 105.

The increase in  $\bar{K}'_C$  with age was the result of continuing hydration of the cement particles to produce a higher strength matrix. Also the matrix-aggregate bond strength increased with age. After 90 days cure, the change in fracture toughness with age was not significant because the change in matrix strength with time was low.

The amount of moist cure relative to air cure for a total curing period of 29 days did not have a significant effect on  $K'_C$ .

#### 5.3.4 Fine Aggregate Content and Gradation

In the mortar series there was a 16.2 per cent increase in  $\bar{K}'_C$  when the fine aggregate was increased from 55.0 per cent to 70.0 per cent as shown in Fig. 106; however, for the concrete series there was a 2.3 per cent decrease in  $\bar{K}'_C$  when the fine aggregate content was increased from 35.0 to 50.0 per cent as shown in Fig. 107.

In the mortar series there was a 5.0 per cent decrease in  $\bar{K}'_C$  with an increasing fineness modulus of sand for the range of fineness modulus investigated as shown in Fig. 108.

There was an increase in  $\bar{K}'_C$  for the mortar with an increasing amount of fine aggregate because the concentration of crack arresting particles in the matrix was increased.  $\bar{K}'_C$  was not affected by the fineness modulus of fine aggregate because there was not a significant variation in fine aggregate particle size.

The concrete  $\bar{K}_C^I$  was not significantly affected by the fine aggregate content because of the overriding effect of the coarse aggregate.

### 5.3.5 Gravel Content, Gradation, and Type

$\bar{K}_C^I$  for the concretes increased 13.3 per cent when the fineness modulus was increased from 6.3 to 7.1 as shown in Fig. 109. When the percentage of coarse aggregate was increased from 0.0 per cent to 50.0 per cent there was a 37.0 per cent increase in  $\bar{K}_C^I$  as shown in Fig. 110.

$\bar{K}_C^I$  of the concrete series cast with a crushed limestone was 28.9 per cent, 17.7 per cent, and 1.7 per cent higher than  $\bar{K}_C^I$  for concrete cast with a river gravel at ages of 3 days, 6 days, and 28 days, respectively. However, at an age of 90 days  $\bar{K}_C^I$  for the concrete cast with a river gravel was 5.0 per cent higher than the concrete cast with a crushed limestone as shown in Fig. 103.

$\bar{K}_C^I$  increased with an increase in maximum size particles because the larger size aggregates act as better crack arresters. However, a maximum can be reached where too great a maximum particle size in conjunction with a poor gradation will produce a lower  $\bar{K}_C^I$  because of the effects of segregation as shown in Fig. 109 for a fineness modulus of 7.45.

An increased gravel content increased  $\bar{K}_C^I$  because the larger gravel content enlarged the concentration of crack arresters in the matrix.

$\bar{K}_C^I$  for the crushed limestone coarse aggregate was greater than  $\bar{K}_C^I$  for the river gravel coarse aggregate until an age of 28 days because the crushed limestone apparently developed a greater bond strength. However, after an age of 28 days the bond strengths for the two types of coarse aggregate appeared to be equivalent.

## 6. RIGID-PLASTIC CRACKED STRIP MODEL

### 6.1 Development of Model

The rigid-plastic cracked strip model (Fig. 111) is a modification of Rice's rigid-plastic strip model (Fig. 2). The model consists of two elastic half planes joined together along a strip of rigid-elastic material which contains a void simulating a crack and a zone of length  $\omega$  which corresponds to the region of inelastic deformation; i.e., yielding or microcracking.

The length of the inelastic zone,  $\omega$ , is a function of the elastic stress intensity factor,  $K_e$ , for the given load and geometry, threshold stress,  $\sigma_{th}$ , for microcracking or yielding, and the stress distribution along the length of inelastic deformation. The region of inelastic deformation is determined by the condition that stresses should be bounded to eliminate the stress singularity at the crack tip. For the infinite sheet with a semi-infinite crack of Fig. 112 (6)

$$K_e = - \sqrt{\frac{2}{\pi}} \int_0^{\omega} x^{-1/2} \sigma_{th}(x) dx. \quad (5)$$

The Rice's model is a special case of Eq. 5 in which the stress is uniform and equal to  $\sigma_{th}$  along the entire inelastic region. The length  $\omega$  becomes

$$\omega = \frac{\pi}{8} \left[ \frac{K_e}{\sigma_{th}} \right]^2. \quad (6)$$

In general, the length of the inelastic region,  $\omega$ , will be of the form

$$\omega = \alpha \left[ \frac{K_e}{\sigma_{th}} \right]^2 \quad (7)$$

where  $\alpha$  is a constant determined by the stress distribution along the length of the inelastic zone. Equation 7 is presented graphically in Fig. 113. The ratio of the length of inelastic zone to stress distribution constant is obtained directly if the elastic stress intensity factor and threshold stress are known.

### 6.2 Analysis of Model

Equation 7 provides an estimate of the size of the region of



inelastic deformation as a function of the elastic stress intensity factor, threshold stress, and stress distribution constant. Since the critical elastic stress intensity factor and threshold stress are material properties, the inelastic zone size will be dependent on the distribution of stress near the inelastic-elastic interface of the model. Various assumed stress distributions and their corresponding stress distribution constants are presented in Table VII.

For a non-strain hardening material, distributions four and six of Table VII form an upper and lower bound, respectively, on the size of the inelastic region. Ductile materials or materials with a distinct yield plateau would tend to approach distribution six while brittle materials might approach distribution four. However, most materials are neither ideally ductile nor ideally brittle so an intermediate distribution, depending on the material, would be expected to give the best results.

### 6.3 Model for Fracture of Portland Cement Paste

Hardened portland cement paste consists of colloidal size gel particles, unhydrated cement, calcium hydroxide crystals, water, gel pores, and capillary cavities. Properties of the paste are dependent on the cement gel.

#### 6.3.1 Strength of Paste

Strength of the paste is derived from the inherent strength of the gel and the physical and chemical bonds between the gel particles. The size of the gel particles, expressed as the diameter of an equivalent sphere, is approximately 87 Å. Spacing of these particles is estimated to be about 20 Å.

#### 6.3.2 Model for Fracture

Assuming that the stress-displacement curve (Fig. 114) between gel particles can be approximated by a sine curve of wave length  $\lambda$  and that for small displacements Hooke's law is valid, an estimate of the theoretical cohesive strength,  $\sigma_c$ , is

$$\sigma_c = \sqrt{\frac{E \cdot \gamma_s}{s_0}} \quad (8)$$

where  $E$  is Young's modulus,  $\gamma_s$  is the work done in creating a new surface area by breaking of bonds, surface energy, and  $s_0$  is the

equilibrium spacing between gel particles in the absence of applied stress. Taking typical values for a paste of  $E = 3.4 \times 10^6$  psi,  $s_o = 8.0 \times 10^{-8}$  in., and  $\gamma_s = 0.0046$  in.-lb/in.<sup>2</sup> (1), the theoretical cohesive strength of paste is approximately  $4.4 \times 10^5$  psi. However, measured tensile strengths are two and three orders of magnitude smaller than this because of crack growth from existing flaws in the material and the random orientation of gel particles.

The fracture toughness of hardened cement paste is approximately 0.340 ksi  $\sqrt{\text{in.}}$  (6). Converting this to rate of release of energy with respect to increasing crack surface (G) by Eq. 3 results in the energy requirements for crack propagation in cement paste being approximately an order of magnitude greater than the surface energy of the new crack surface. Therefore, an inelastic deformation such as microcracking must occur in the region of the crack tip.

The rigid-plastic cracked strip model for fracture of cement paste (Fig. 115) is a modification of the model for a purely brittle material (Table VII, Distribution 4). With increasing microcracking of paste the model maintains a smooth transition between the linear-elastic stresses and the stress distribution along the cracked region of the model ( $d\sigma_{th}/dx = 0$  at  $x = 0$  and  $x = \omega$ ).

The size of the microcracking zone can be predicted by the rigid-plastic cracked strip model as a function of the threshold stress, elastic stress intensity factor, and stress distribution constant of Table VII, Distribution 1.

$$\omega = .831 \left[ \frac{K_e}{\sigma_{th}} \right]^2 \quad (9)$$

Using Fig. 113, the model indicates that the length of the microcracking region is on the order of 0.025 in. if  $\sigma_{th}$  is around 2000 psi. Thus, the microcracking region is approximately five orders of magnitude larger than the gel particles.

With the addition of aggregate to the paste, the material will no longer be homogeneous. The aggregate will affect the elastic stress field in the region of the crack tip. Since the aggregate particles are 5-8 orders of magnitude larger than the gel particles and are materials

of high modulus (stiffness) relative to the gel, the aggregate acts as an arresting function to increase the fracture toughness and micro-cracking region (4).

## 7. SUMMARY AND CONCLUSIONS

### 7.1 Object and Scope

The object of this study is to develop a better understanding of the fracture mechanism of concrete, and to determine the concrete parameters effect on concrete fracture toughness.

A rigid-plastic cracked strip model was developed to provide an estimate of the length of the microcracking region in a cement paste.

The experimental program included eight paste, thirty-two mortar, and forty-five concrete mix designs. Variables in the investigation were the water-cement ratio, sand-cement ratio, gravel-cement ratio, degree of hydration (age of specimens at testing), curing conditions, air content, sand gradation, and gradation and type of coarse aggregate.

Nominal dimensions of the paste and mortar specimens (except for three concrete series) were 2 by 2 by 14 in., and nominal dimensions of the concrete specimens (except for one mortar series) were 4 by 4 by 12 in. All specimens were subjected to four-point bending. Nominal flaw depths ranged from 1/4 in. to 1 in. for the paste and mortar series, and 1/2 in to 1-1/2 in. for the concrete series. A continuous record of load and deformation was made until failure.

### 7.2 Experimental Results

The effective fracture toughness for concrete was based on the assumption that the concrete was homogeneous and the flaw depth at failure was equal to the cast flaw depth. The mean effective fracture toughness for the pastes ranged from 0.278 ksi  $\sqrt{\text{in.}}$  to 0.407 ksi  $\sqrt{\text{in.}}$ . The mean effective fracture toughness for the mortars ranged from 0.192 ksi  $\sqrt{\text{in.}}$  to 0.514 ksi  $\sqrt{\text{in.}}$  and the mean effective fracture toughness for the concretes ranged from 0.342 ksi  $\sqrt{\text{in.}}$  to 0.702 ksi  $\sqrt{\text{in.}}$ .

In the paste and mortar series there was a decrease in effective fracture toughness with increasing water-cement ratio, while in the concrete series there was no apparent effect of varying the water-cement ratio on effective fracture toughness for the range of water-cement ratios investigated.

Increasing the air content decreased the effective fracture toughness for the paste, mortar, and concrete series.



In the paste, mortar, and concrete series there was an increase in effective fracture toughness with age. This increase was significant up to an age of 29 days, but the difference between the effective fracture toughness for 29 days cure and 92 days cure was insignificant.

No definite trend was apparent in the variation of effective fracture toughness with curing conditions for the mortar and concrete series.

In the mortar series there was an increase in effective fracture toughness with increasing sand-cement ratio, however there was a slight decrease in effective fracture toughness with increasing sand-cement ratio for the concretes.

The fineness modulus of sand did not have an apparent effect on the effective fracture toughness of the mortar series over the range of fineness modulus investigated.

The effective fracture toughness of the concrete series increased with an increase in the maximum size of coarse aggregate and also with an increased gravel cement ratio. However, there was a decrease in the effective fracture toughness when a large amount of maximum size aggregate was used in the mix. This was probably attributable to segregation.

The effective fracture toughness of the concrete series cast with a river gravel coarse aggregate was lower than the effective fracture toughness of the concrete series cast with a crushed limestone coarse aggregate for ages of 3 days and 6 days; however, at ages of 29 days and 92 days the difference in their effective fracture toughness was insignificant.

### 7.3 Model for Fracture of Cement Paste

A rigid-plastic cracked strip model was developed to approximate inelastic phenomenon in the region of the crack tip. An estimate of the length of the inelastic zone in the region of the crack tip can be obtained if the elastic stress intensity factor, for the given load and geometry, and threshold stress for microcracking are known.

### 7.4 Significance

The effective fracture toughness of concrete was not significantly effected by the fine aggregate content (30.0 per cent to 50.0 per cent, by weight), air content (4.0 per cent to 10.0 per cent), and water-cement

ratio (5.7 gal/sack to 7.3 gal/sack). Since the range of these parameters investigated is inclusive of most mix designs, they can be neglected in designing for a mix of high or low fracture toughness (material resistance to propagation of a flaw). Therefore, the variables affecting the fracture toughness of concrete can be limited to the coarse aggregate content and gradation of coarse aggregate.

The fracture toughness of concrete was found to be directly proportional to both coarse aggregate content and gradation. Thus, by increasing or decreasing the percentage of coarse aggregate, or increasing or decreasing the maximum aggregate size, or a combination of both, the fracture toughness can be adjusted. However, if the fracture toughness is to be increased by using a larger maximum size coarse aggregate, the gradation of coarse aggregate must be uniform to minimize segregation and its detrimental effects. Limitations will be placed on maximum aggregate size by the size and shape of the concrete members and by the amount and distribution of reinforcing steel.

In the design of all mixes the objectives of: (1) required qualities of hardened concrete; (2) workability of fresh concrete; and, (3) economy should be maintained even though it may mean a sacrifice in desired fracture toughness.

## REFERENCES

1. Kaplan, M. F., "Crack Propagation and the Fracture of Concrete," Proc., ACI, Vol. 58, 1961, pp. 591-611.
2. Glucklich, J., "Fracture of Plain Concrete," Proc. ASCE, Vol. 89, No. EM 6, 1963, pp. 127-138.
3. Glucklich, J., "Static and Fatigue Fractures of Portland Cement Mortars in Flexure," Proc. First International Conference on Fracture, Vol. 2, Sendai, Japan, 1965, pp. 1343-1382.
4. Lott, J. L., and Kesler, C. E., "Crack Propagation in Plain Concrete," Symposium on Structure of Portland Cement Paste and Concrete, H.R.B. Special Report 90, Washington, D. C., 1966, pp. 204-218.
5. Raecke, D. A., and Lott, J. L., "First Progress Report, The Control of Cracking of Concrete," Theoretical and Applied Mechanics Report No. 667, University of Illinois, 1966, pp. 1-38.
6. Raecke, D. A., Naus, D. J., and Lott, J. L., "Second Progress Report, The Control of Cracking of Concrete," Theoretical and Applied Mechanics Report No. 676, University of Illinois, 1967, pp. 1-34.
7. "Fracture Toughness Testing and Its Applications," ASTM STP No. 381, Am. Soc. for Testing Materials, April 1965.
8. Brown, W. F., and Srawley, J. E., "Plane Strain Crack Toughness Testing of High Strength Metallic Materials," ASTM STP No. 410, Am. Soc. for Testing Materials, 1966, pp. 13-14.
9. Irwin, G. R., "Fracture," Handbuch der Physik, Vol. 6, Springer (Berlin), 1958, pp. 551-590.
10. Irwin, G. R., "Structural Mechanics," Pergamon Press (London), 1960, p. 557.
11. Irwin, G. R., "Proceedings of the 1960 Sagamore Research Conference on Ordnance Materials," p. IV, 63, 1961: Washington, D. C. (U. S. Office of Technical Services).
12. McClintock, F. A., and Hult, J. A. H., "Proceedings of the 9th International Conference on Applied Mathematics," (Brussels, 1956), Vol. 8, p. 51.
13. Westergaard, H. M., "Bearing Pressure and Cracks," ASME, Vol. 61, 1939, pp. A-49-A-53.
14. Irwin, G. R., "Analysis of Stresses and Strains Near the End of a Crack Traversing a Plate," J. App. Mech., Vol. 24, 1957, pp. 361-364.

15. Golestaneh, A. A., Brit. Weld. Research Assoc. Rep. (C33/1/57), 1957.
16. Griffith, A. A., "The Phenomena of Rupture and Flow in Solids," Philosophical Transactions, Roy. Soc. of London, Vol. 221, Series A, 1920, pp. 163-198.
17. Irwin, G. R., "Fracturing and Fracture Mechanics," Theoretical and Applied Mechanics Report No. 202, University of Illinois, 1961, p. 6.
18. Rice, J. R., "Plastic Yielding at a Crack Tip," Proc. First International Conference on Fracture, Vol. 1, Sendai, Japan, 1965, pp. 283-308.
19. Dugdale, D. S., "Yielding of Steel Sheets Containing Slits," J. Mech. Phys. Solids, Vol. 8, 1960.
20. Barenblatt, G. I., "On Equilibrium Cracks Formed in Brittle Fracture," Appl. Math. Mech., Vol. 23, 3, 1959.
21. Barenblatt, G. I., "Mathematical Theory of Equilibrium Cracks in Brittle Fracture," Advances in Applied Mechanics, Vol. 7, Academic Press, New York, 1962, pp. 55-129.
22. Powers, T. C., and Brownyard, T. L., "Studies of the Physical Properties of Hardened Portland Cement Paste," Proc. ACI, Vol. 41, pp. 101-132, 249-504, 549-602, 669-712, 845-880, and 992-993, 1946-47.



TABLE I

## GRADATION OF FINE AGGREGATE

Designation	% Retained on Sieve						Fineness Modulus
	4	8	16	30	50	100	
I	0.0	5.0	10.0	45.0	77.0	100.0	2.37
II	0.0	11.0	33.0	63.0	83.0	100.0	2.90
III	0.0	15.7	47.1	47.1	75.7	100.0	2.86
IV	0.0	20.0	45.0	75.0	90.0	100.0	3.30

TABLE II

## GRADATION OF COARSE AGGREGATE

Designation	% Retained on Sieve Size Indicated				Fineness Modulus
	3/4 in.	1/2 in.	3/8 in.	#4	
I	5.0	30.0	50.0	100.0	6.55
II	5.0	50.0	70.0	100.0	6.75
III	10.0	50.0	50.0	100.0	6.60
IV	25.0	65.0	85.0	100.0	7.10
V	5.0	15.0	35.0	100.0	6.40
VI	50.0	85.0	95.0	100.0	7.45
VII	20.7	49.5	72.0	100.0	6.93
VIII	0.0	0.0	38.4	100.0	6.38
IX	0.0	35.0	60.0	100.0	6.60

TABLE III

## PROPERTIES OF MIXES

Series	Relative Weights, SSD Basis			Type Gravel	Sand Gradation	Gravel Gradation	Curing (days)	Air Content %
	Cement	Water	Sand					
1 <sup>a</sup>	1.0	0.27	0	0	...	...	29 Moist	3.3
2	1.0	0.30	0	0	...	...	29 Moist	2.1
3	1.0	0.30	0	0	...	...	29 Moist	3.3
4	1.0	0.30	0	0	...	...	29 Moist	4.0
5	1.0	0.30	0	0	...	...	29 Moist	7.0
6	1.0	0.30	0	0	...	...	29 Moist	7.8
7	1.0	0.30	0	0	...	...	6 Moist	...
8	1.0	0.36	0	0	...	...	29 Moist	0.4
9	1.0	0.40	2.0	0	11	...	29 Moist	2.0
10	1.0	0.40	2.5	0	11	...	29 Moist	3.9
11	1.0	0.50	2.0	0	11	...	29 Moist	0.9
12	1.0	0.50	2.5	0	11	...	29 Moist	0.7
13	1.0	0.50	3.0	0	11	...	29 Moist	3.4
14	1.0	0.50	3.0	0	11	...	29 Moist	3.6

<sup>a</sup>Series 1-42 were 2 x 2 x 14 in. prisms.

TABLE III (Continued)

## PROPERTIES OF MIXES

Series	Relative Weights, SSD Basis		Type Gravel	Sand Gradation	Gravel Gradation	Curing (days)	Air Content %
	Cement	Water					
15	1.0	0.50	3.0	0	...	29 Moist	...
16	1.0	0.50	3.0	0	...	29 Moist	6.2
17	1.0	0.50	3.0	0	...	29 Moist	8.9
18	1.0	0.50	3.0	0	...	2 Moist	3.7
19	1.0	0.50	4.0	0	...	29 Moist	4.4
20	1.0	0.60	3.0	0	...	29 Moist	0.8
21	1.0	0.60	4.0	0	...	29 Moist	4.3
22	1.0	0.50	3.0	0	...	29 Moist	6.8
23	1.0	0.50	3.0	0	...	29 Moist	2.9
24	1.0	0.50	3.0	0	...	29 Moist	4.2
25	1.0	0.50	3.0	0	...	29 Moist	...
26	1.0	0.50	3.0	0	...	92 Moist	5.1
27	1.0	0.50	3.0	0	...	244 Moist	3.2
28	1.0	0.50	3.0	0	...	7 Moist 22 Air	3.1

TABLE III (Continued)

## PROPERTIES OF MIXES

Series	Relative Weights, SSD Basis			Type Gravel	Sand Gradation	Gravel Gradation	Curing (days)	Air Content %
	Cement	Water	Sand					
29	1.0	0.50	3.0	0	...	...	29 Moist	...
30	1.0	0.50	3.0	0	...	...	29 Moist	...
31	1.0	0.50	3.0	0	...	...	6 Moist	4.4
32	1.0	0.50	3.0	0	...	...	29 Moist	...
33	1.0	0.50	3.5	0	...	...	29 Moist	5.8
34	1.0	0.50	3.0	0	...	...	14 Moist 15 Air	3.1
35	1.0	0.45	3.0	0	...	...	29 Moist	5.2
36	1.0	0.50	3.0	0	...	...	7 Moist 22 Air	2.9
37	1.0	0.50	3.0	0	...	...	3 Moist	3.6
38	1.0	0.50	3.0	0	...	...	14 Moist 15 Air	4.8
39	1.0	0.55	3.0	0	...	...	29 Moist	2.2
40	1.0	0.55	3.0	1.0	Cr. Lst.	VIII	29 Moist	2.9
41	1.0	0.55	3.0	2.0	Cr. Lst.	VIII	29 Moist	2.0
42	1.0	0.55	3.0	3.0	Cr. Lst.	VIII	29 Moist	2.2

TABLE III (Continued)

## PROPERTIES OF MIXES

Series	Relative Weights, SSD Basis		Type Gravel	Sand Gradation	Gravel Gradation	Curing (days)	Air Content %
	Cement	Water					
43 <sup>b</sup>	1.0	0.60	3.0	0	...	29 Moist	1.4
44	1.0	0.60	3.0	1.5	Cr. Lst.	29 Moist	0.9
45	1.0	0.60	3.0	3.0	Cr. Lst.	29 Moist	1.5
46	1.0	0.60	3.0	4.0	Cr. Lst.	29 Moist	1.5
47	1.0	0.60	3.0	3.0	Cr. Lst.	90 Moist	1.5
48	1.0	0.50	3.0	3.0	Cr. Lst.	29 Moist	0.4
49	1.0	0.60	2.5	3.0	Cr. Lst.	29 Moist	1.1
50	1.0	0.60	4.0	3.0	Cr. Lst.	29 Moist	3.4
51	1.0	0.60	3.0	3.0	Cr. Lst.	29 Moist	6.2
52	1.0	0.60	3.0	3.0	Cr. Lst.	29 Moist	7.8
53	1.0	0.60	3.0	3.0	Cr. Lst.	29 Moist	11.0
54	1.0	0.60	3.0	3.0	Cr. Lst.	29 Moist	2.4
55	1.0	0.60	3.0	3.0	Cr. Lst.	29 Moist	2.4
56	1.0	0.60	3.0	3.0	Cr. Lst.	29 Moist	1.9

<sup>b</sup>Series 43-85 were 4 x 4 x 12 in. prisms.



TABLE III (Continued)

## PROPERTIES OF MIXES

Series	Type Gravel			Sand Gradation	Gravel Gradation	Curing (days)	Air Content %		
	Cement	Water	Sand						
57	1.0	0.60	3.0	3.0	River Gr.	II	VII	29 Moist	2.1
58	1.0	0.60	3.0	3.0	Cr. Lst.	II	VII	3 Moist	2.3
59	1.0	0.60	3.0	3.0	Cr. Lst.	II	IX	29 Moist	2.1
60	1.0	0.55	3.0	3.0	Cr. Lst.	II	IX	29 Moist	2.3
61	1.0	0.60	3.0	3.0	Cr. Lst.	II	IX	7 Moist 85 Air	2.6
62	1.0	0.60	3.0	3.0	Cr. Lst.	II	IX	14 Moist 78 Air	2.2
63	1.0	0.60	3.0	3.0	Cr. Lst.	II	II	29 Moist	2.0
64	1.0	0.60	3.0	3.0	Cr. Lst.	II	V	29 Moist	2.4
65	1.0	0.60	3.0	3.0	Cr. Lst.	II	VI	29 Moist	1.8
66	1.0	0.65	3.0	3.0	Cr. Lst.	II	IX	29 Moist	1.8
67	1.0	0.60	3.0	3.0	Cr. Lst.	II	IX	29 Moist	11.8
68	1.0	0.60	3.0	3.0	River Gr.	II	VII	6 Moist	4.2
69	1.0	0.60	3.0	3.0	Cr. Lst.	II	IX	91 Air	2.2

TABLE III (Continued)

## PROPERTIES OF MIXES

Series	Relative Weights, SSD Basis			Type Gravel	Sand Gradation	Gravel Gradation	Curing (days)	Air Content %	
	Cement	Water	Gravel						
70	1.0	0.60	3.0	3.0	Cr. Lst.	II	IX	29 Moist	12.2
71	1.0	0.60	3.0	3.0	River Gr.	II	VII	92 Moist	3.3
72	1.0	0.60	3.0	3.0	Cr. Lst.	II	VII	6 Moist	1.9
73	1.0	0.60	3.0	3.0	Cr. Lst.	II	VII	91 Moist	2.4
74	1.0	0.60	3.0	3.0	River Gr.	II	VII	3 Moist	3.6
75	1.0	0.60	3.0	3.0	Cr. Lst.	II	VII	29 Moist	2.4
76	1.0	0.65	3.0	3.0	River Gr.	II	VII	91 Moist	1.9
77	1.0	0.60	3.0	3.0	Cr. Lst.	II	IX	29 Moist	9.3
78	1.0	0.60	3.0	3.0	River Gr.	II	VII	92 Moist	3.3
79	1.0	0.60	4.5	3.0	Cr. Lst.	II	IX	29 Moist	3.8
80	1.0	0.60	3.5	3.0	Cr. Lst.	II	IX	29 Moist	3.3
81	1.0	0.60	3.0	4.5	Cr. Lst.	II	IX	29 Moist	2.2
82	1.0	0.60	3.0	2.5	Cr. Lst.	II	IX	29 Moist	...
83	1.0	0.60	3.0	3.5	Cr. Lst.	II	IX	29 Moist	2.5

TABLE III (Concluded)

## PROPERTIES OF MIXES

Series	Relative Weights, SSD Basis			Type Gravel	Sand Gradation	Gravel Gradation	Curing (days)	Air Content %	
	Cement	Water	Sand						
84	1.0	0.60	3.0	3.0	River Gr.	II	VII	29 Moist	3.9
85	1.0	0.60	3.0	3.0	River Gr.	II	VII	3 Moist	3.8

TABLE IV  
STRENGTHS AND DYNAMIC MODULUS

Series	Compressive Strength psi	Splitting Tensile Strength psi	Modulus of Rupture psi	Dynamic Modulus $\times 10^{-6}$ psi
1 <sup>a</sup>	15770	...	813	3.71
2	15740	637	649	3.46
3	15300	582	588	3.06
4	13370	442	821	3.65
5	13740	428	657	2.04
6	12860	353	785	3.05
7	12870	443	756	3.88
8	14060	400	487	3.09
9	11430	572	958	4.92
10	10330	635	751	4.82
11	8010	561	716	4.17
12	8040	623	767	4.49
13	8240	525	637	...
14	7700	593	721	4.42
15	8620	545	781	5.18
16	6370	488	656	4.79
17	6730	524	633	4.56
18	4360	395	373	3.25
19	7400	498	758	...
20	7480	524	801	4.52

<sup>a</sup>Series 1-42 were 2 x 2 x 14 in. prisms.

Continued

TABLE IV (Continued)

## STRENGTHS AND DYNAMIC MODULUS

Series	Compressive Strength psi	Splitting Tensile Strength psi	Modulus of Rupture psi	Dynamic Modulus $\times 10^{-6}$ psi
21	6660	462	551	4.48
22	6550	435	844	4.74
23	7790	517	779	4.30
24	7290	486	636	4.17
25	8170	517	819	4.44
26	9350	589	1137	6.49
27	9210	641	965	4.64
28	8800	590	895	...
29	6410	477	712	5.87
30	5700	421	714	4.54
31	5050	444	738	5.91
32	6460	499	851	5.48
33	4360	461	819	5.77
34	9190	502	824	...
35	8930	505	734	5.50
36	8400	484	807	5.75
37	3740	337	455	3.34
38	8500	452	735	4.60
39	7570	537	723	5.82
40	7520	500	773	4.55

Continued



TABLE IV (Continued)  
STRENGTHS AND DYNAMIC MODULUS

Series	Compressive Strength psi	Splitting Tensile Strength psi	Modulus of Rupture psi	Dynamic Modulus $\times 10^{-6}$ psi
41	7780	537	833	4.81
42	7840	575	862	5.14
43 <sup>b</sup>	4050	447	685	...
44	4210	467	696	...
45	4800	520	682	...
46	4860	505	734	...
47	6000	549	804	6.11
48	6000	559	761	...
49	5220	485	638	...
50	4440	428	681	...
51	3540	408	654	...
52	4080	360	607	...
53	3570	350	619	...
54	4930	491	749	...
55	5530	479	722	...
56	4770	435	661	...
57	5210	458	695	5.80
58	...	361	473	...
59	5090	444	700	...
60	6480	...	713	...

<sup>b</sup>Series 43-85 were 4 x 4 x 12 in. prisms.

Continued

TABLE IV (Continued)  
STRENGTHS AND DYNAMIC MODULUS

Series	Compressive Strength psi	Splitting Tensile Strength psi	Modulus of Rupture psi	Dynamic Modulus $\times 10^{-6}$ psi
61	6290	532	860	5.73
62	6630	610	860	5.72
63	5290	519	677	...
64	4720	529	760	...
65	5030	513	687	...
66	4850	486	696	...
67	3100	398	617	4.74
68	3350	328	501	...
69	5670	495	775	5.20
70	3420	396	583	4.93
71	4980	532	651	6.27
72	3750	377	510	...
73	6080	585	774	6.37
74	2150	262	379	4.44
75	5350	537	796	6.21
76	4750	466	654	5.89
77	3990	407	668	5.05
78	4830	555	721	6.21
79	3830	406	623	5.62
80	5090	498	703	6.03

Continued

TABLE IV (Concluded)

## STRENGTHS AND DYNAMIC MODULUS

Series	Compressive Strength psi	Splitting Tensile Strength psi	Modulus of Rupture psi	Dynamic Modulus $\times 10^{-6}$ psi
81	4850	478	829	6.30
82	5000	482	734	5.98
83	4910	515	837	6.24
84	4840	431	703	5.86
85	2570	287	353	4.64

TABLE V  
AVERAGE STRESS INTENSITY FACTORS

Series	$\bar{K}_c'$ ksi $\sqrt{\text{in.}}$	Coefficient of Variation per cent	$\bar{K}_I'$ ksi $\sqrt{\text{in.}}$	Coefficient of Variation per cent
1 <sup>a</sup>	0.387	22.2	0.174	21.8
2	0.407	22.3	0.183	22.3
3	0.336	19.6	0.151	19.5
4	0.369	20.9	0.182	16.3
5	0.299	18.9	0.139	15.0
6	0.318	11.9	0.173	29.0
7	0.351	13.0	0.172	8.9
8	0.278	16.4	0.125	16.3
9	0.498	9.8	0.226	10.6
10	0.424	10.8	0.191	10.7
11	0.378	8.9	0.170	8.8
12	0.397	7.7	0.179	7.7
13	0.376	9.7	0.222	10.2
14	0.391	8.5	0.223	5.7
15	0.406	13.2	0.261	19.9
16	0.339	9.8	0.210	6.0
17	0.317	8.9	0.188	10.3
18	0.258	6.9	0.157	5.9
19	0.428	9.6	0.263	10.6
20	0.373	8.7	0.215	10.5

<sup>a</sup>Series 1-42 were 2 x 2 14 in. prisms.

Continued

TABLE V (Continued)

## AVERAGE STRESS INTENSITY FACTORS

Series	$\bar{K}_C'$ ksi $\sqrt{\text{in.}}$	Coefficient of Variation per cent	$\bar{K}_I'$ ksi $\sqrt{\text{in.}}$	Coefficient of Variation per cent
21	0.284	22.5	0.181	6.0
22	0.392	14.5	0.231	11.0
23	0.379	14.7	0.214	12.3
24	0.397	10.3	0.232	9.0
25	0.420	20.4	0.250	19.0
26	0.514	15.7	0.270	10.8
27	0.449	10.7	0.248	9.7
28	0.437	19.2	0.237	15.0
29	0.387	16.8	0.219	11.4
30	0.439	10.2	0.247	6.4
31	0.356	18.4	0.190	12.3
32	0.458	15.2	0.268	14.2
33	0.458	21.7	0.293	14.3
34	0.434	10.0	0.251	11.1
35	0.466	13.3	0.268	11.6
36	0.444	7.9	0.232	17.9
37	0.192	35.5	0.115	27.2
38	0.402	16.0	0.229	13.6
39	0.423	18.7	...	...
40	0.401	21.5	0.271	12.5

Continued



TABLE V (Continued)

## AVERAGE STRESS INTENSITY FACTORS

Series	$\bar{K}_c'$ ksi $\sqrt{\text{in.}}$	Coefficient of Variation per cent	$\bar{K}_I'$ ksi $\sqrt{\text{in.}}$	Coefficient of Variation per cent
41	0.505	16.7	0.319	13.6
42	0.516	11.3	0.343	12.5
43 <sup>b</sup>	0.476	9.7	0.252	20.5
44	0.536	10.4	0.312	7.5
45	0.545	7.0	0.281	12.5
46	0.583	10.0	0.261	8.4
47	0.666	7.0	0.416	12.5
48	0.607	10.5	0.343	11.0
49	0.572	13.5	0.277	14.6
50	0.582	6.1	0.339	7.5
51	0.554	10.3	0.322	19.5
52	0.528	10.9	0.306	26.0
53	0.503	6.1	0.331	8.0
54	0.632	10.2	0.411	9.2
55	0.569	5.5	0.322	25.3
56	0.672	17.2	0.447	24.2
57	0.585	7.6	0.309	13.8
58	0.519	8.3	0.323	5.3
59	0.556	4.8	0.365	9.6
60	0.618	12.9	0.257	27.7

<sup>b</sup>Series 43-85 were 4 x 4 x 12 in. prisms.

Continued

TABLE V (Continued)

## AVERAGE STRESS INTENSITY FACTORS

Series	$\bar{K}_c^I$ ksi $\sqrt{\text{in.}}$	Coefficient of Variation per cent	$\bar{K}_I^I$ ksi $\sqrt{\text{in.}}$	Coefficient of Variation per cent
61	0.702	12.2	0.399	14.2
62	0.460	9.3	0.355	25.5
63	0.603	12.5	0.258	21.3
64	0.594	5.9	0.328	18.3
65	0.559	5.8	0.301	8.3
66	0.626	12.2	0.388	17.7
67	0.527	12.9	0.325	3.5
68	0.471	9.7	0.253	22.4
69	0.647	9.8	0.412	14.1
70	0.489	8.5	0.307	7.9
71	0.618	17.2	0.436	24.7
72	0.492	6.7	0.343	11.0
73	0.593	3.5	0.392	6.2
74	0.342	11.6	0.187	13.1
75	0.597	6.2	0.397	12.4
76	0.532	15.2	...	...
77	0.553	12.6	0.367	8.9
78	0.634	7.0	0.412	7.2
79	0.533	10.8	0.340	4.2
80	0.615	6.1	0.431	13.2

Continued

TABLE V (Concluded)

## AVERAGE STRESS INTENSITY FACTORS

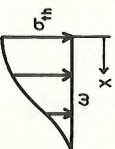
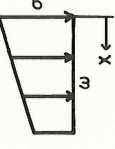
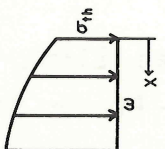
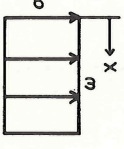
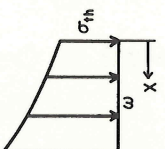
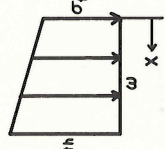
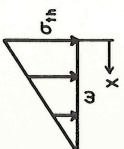
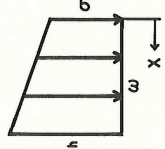
Series	$\bar{K}_c'$ ksi $\sqrt{\text{in.}}$	Coefficient of Variation per cent	$\bar{K}_I'$ ksi $\sqrt{\text{in.}}$	Coefficient of Variation per cent
81	0.682	14.0	0.458	9.6
82	0.548	9.5	0.363	15.2
83	0.643	14.0	0.424	21.9
84	0.582	17.6	0.356	17.1
85	0.375	12.1	0.243	13.2

TABLE VI

SERIES PERTAINING TO EACH CONCRETE PARAMETER INVESTIGATED

Type	Parameter	Series
Paste	water-cement ratio	1, 2, 3, 4, 8
Paste	age	2, 3, 4, 7
Paste	air content	2, 3, 4, 5, 6
Mortar	water-cement ratio	13, 14, 15, 20, 25, 35, 39
Mortar	age	13, 14, 15, 18, 25, 26, 27, 31, 37
Mortar	sand gradation	22, 23, 24, 25
Mortar	air content	13, 14, 16, 17
Mortar	sand-cement ratio	11, 12, 13, 14, 15, 19, 25, 33
Mortar	curing conditions	25, 28, 34, 36, 38
Concrete	water-cement ratio	45, 48, 59, 60, 66
Concrete	age (Cr. Lst.)	58, 72, 73, 75
Concrete	age (River Gr)	57, 68, 71, 74, 78, 84, 85
Concrete	curing conditions	47, 61, 62, 69
Concrete	sand-cement ratio	45, 49, 50, 59, 79, 80
Concrete	air content	45, 51, 52, 53, 59, 67, 70, 77
Concrete	gravel-cement ratio (2x2x14 in.)	39, 40, 41, 42
Concrete	gravel cement ratio (4x4x12 in.)	43, 44, 45, 46, 59, 81, 82, 83
Concrete	gravel gradation	45, 54, 55, 56, 63, 64, 65, 75

TABLE VII  
DISTRIBUTION CONSTANTS

Assumed Shape	Stress Distribution	Distribution Constant $\alpha$	Assumed Shape	Stress Distribution	Distribution Constant $\alpha$
1. 	$\sigma(x) = \frac{\sigma_{th}}{2} \left[ 1 + \cos \frac{\pi x}{w} \right]$	0.831	5. 	$\sigma(x) = \sigma_{th} \left[ 1 - \frac{x}{2w} \right]$	0.565
2. 	$\sigma(x) = \sigma_{th} \left[ 1 + \sin \frac{\pi x}{2w} \right]$	0.190	6. 	$\sigma(x) = \sigma_{th}$	0.393
3. 	$\sigma(x) = \sigma_{th} \left[ 1 + \tan \frac{\pi x}{4w} \right]$	0.237	7. 	$\sigma(x) = \sigma_{th} \left[ 1 + \frac{x}{2w} \right]$	0.290
4. 	$\sigma(x) = \sigma_{th} \left[ 1 - \frac{x}{w} \right]$	0.884	8. 	$\sigma(x) = \sigma_{th} \left[ 1 + \frac{x}{w} \right]$	0.221



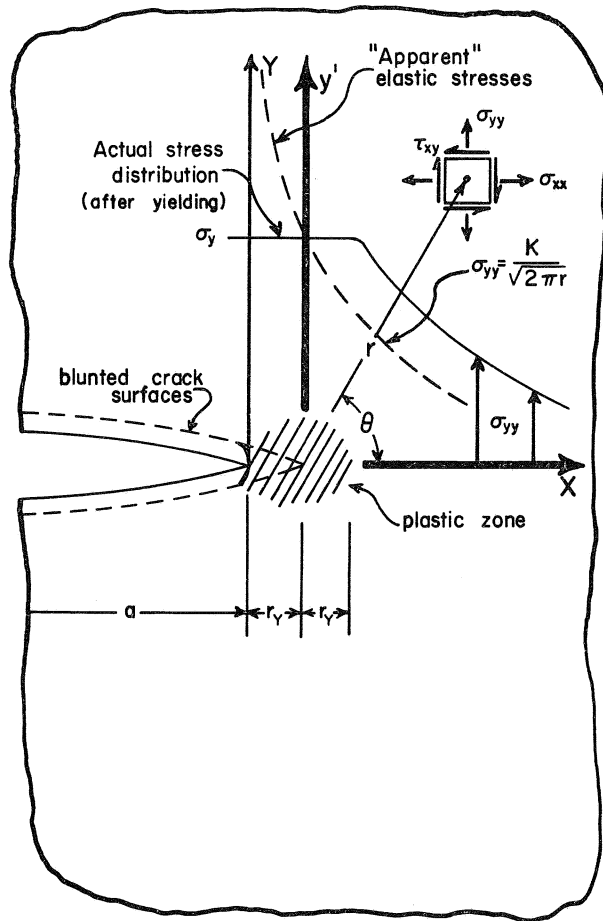


Fig. 1 Distribution of Stress After Inelastic Deformation

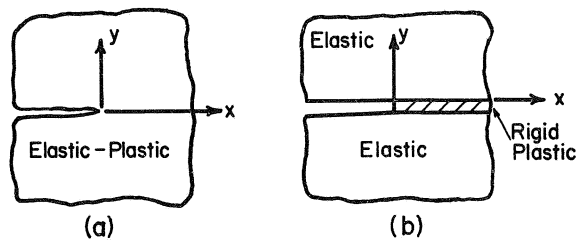


Fig.2 (a) Cracked Elastic-Plastic Body  
(b) Rigid-Plastic Strip Model

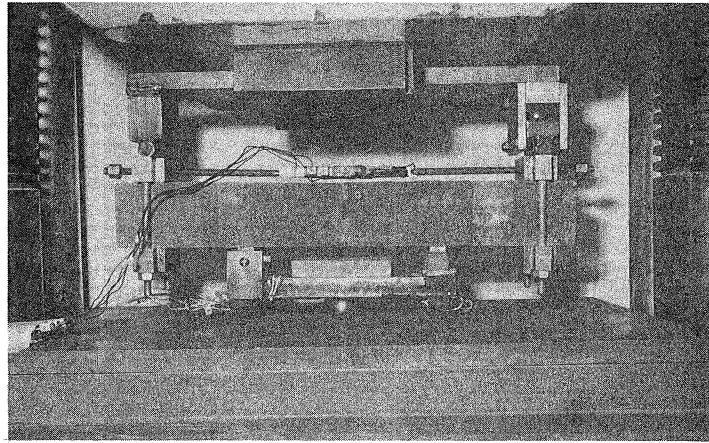


Fig. 3 Test Setup: Paste and Mortar

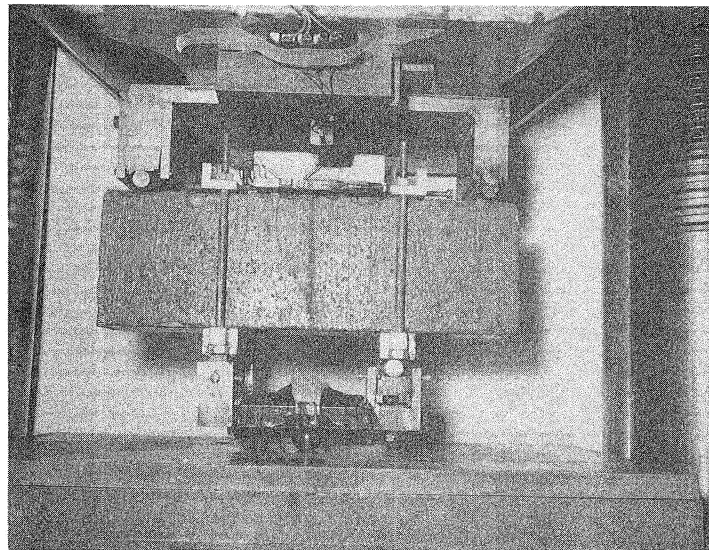


Fig. 4 Test Setup: Concrete

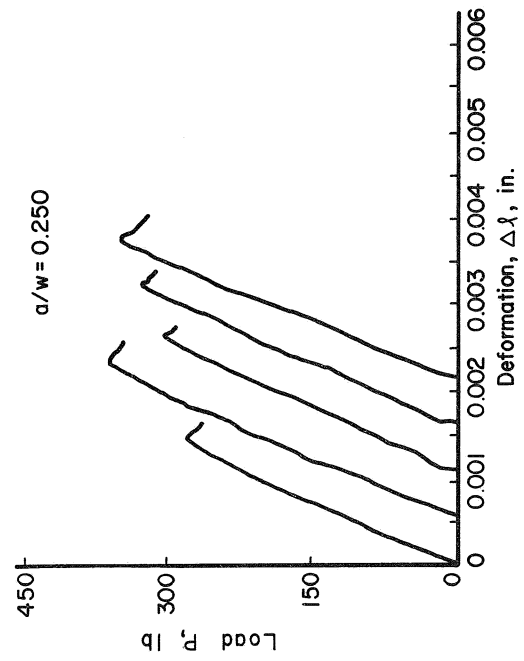
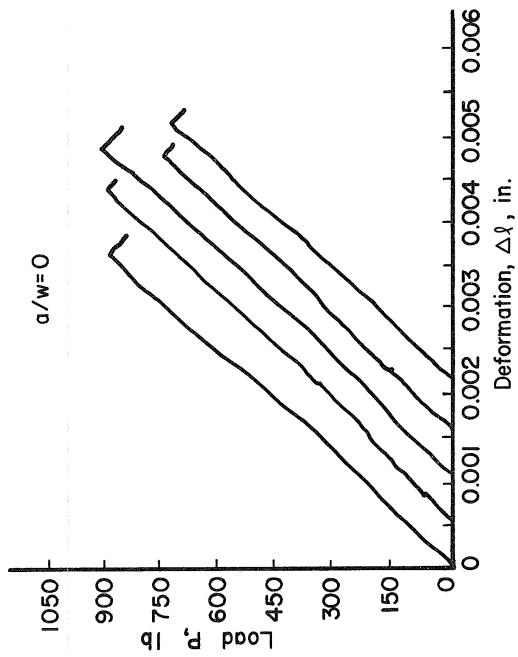
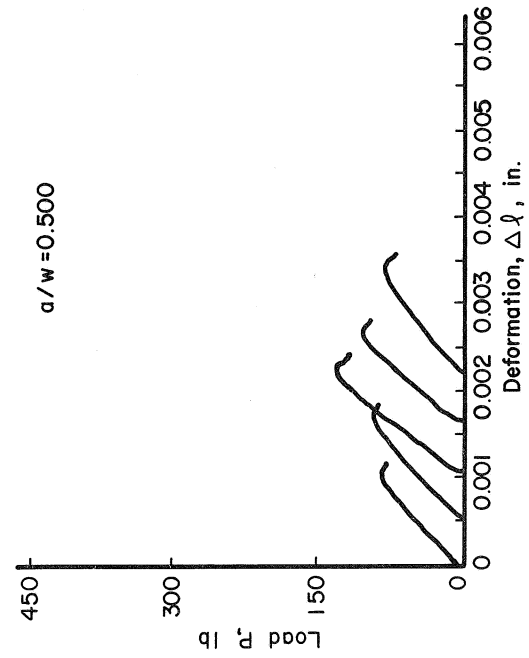
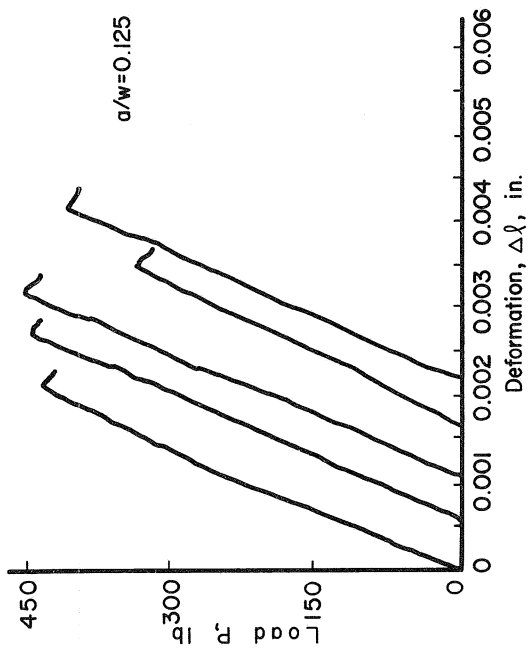


Fig. 5 Typical Load-Deformation Curves: Paste

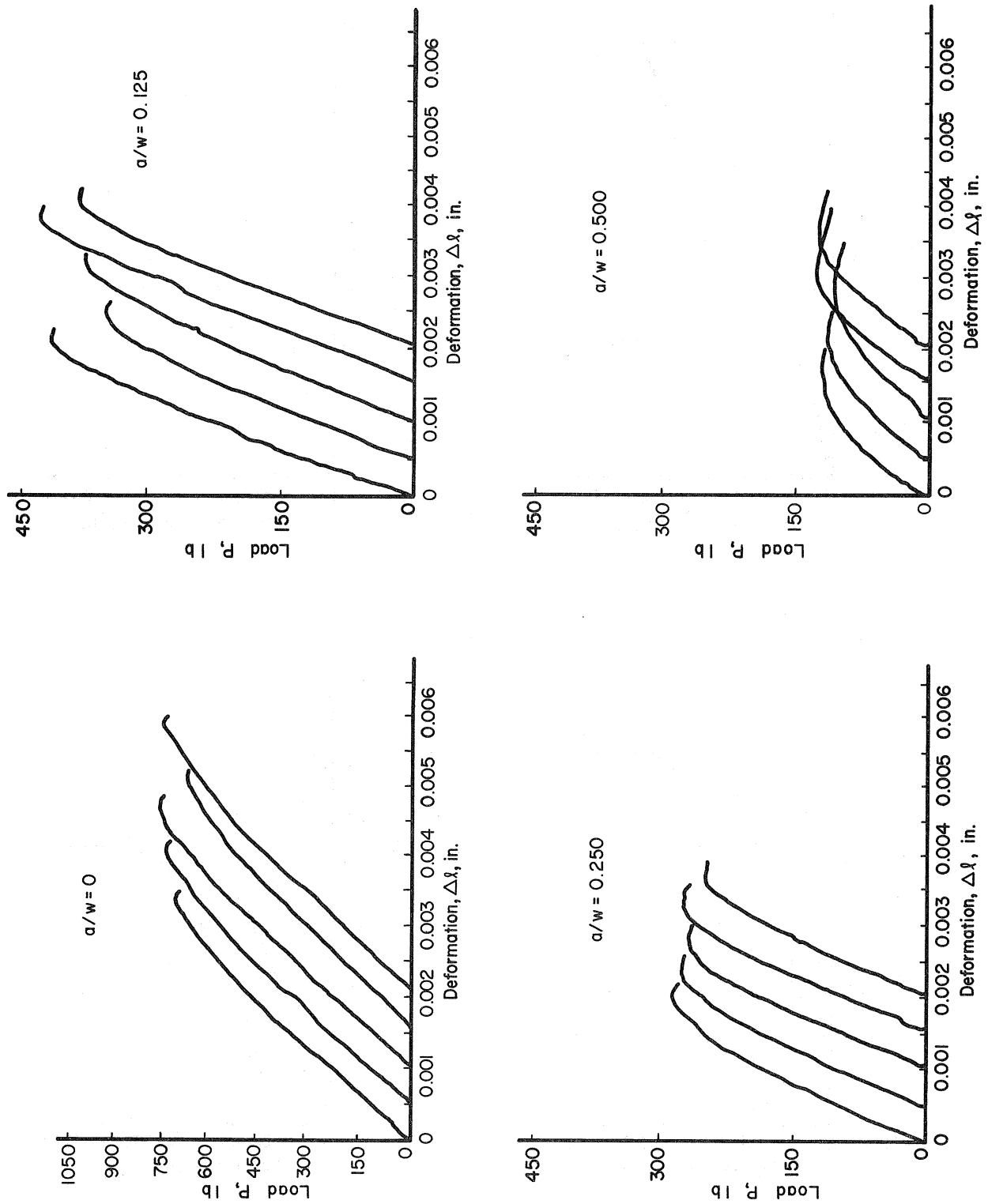


Fig. 6 Typical Load-Deformation Curves: Mortar

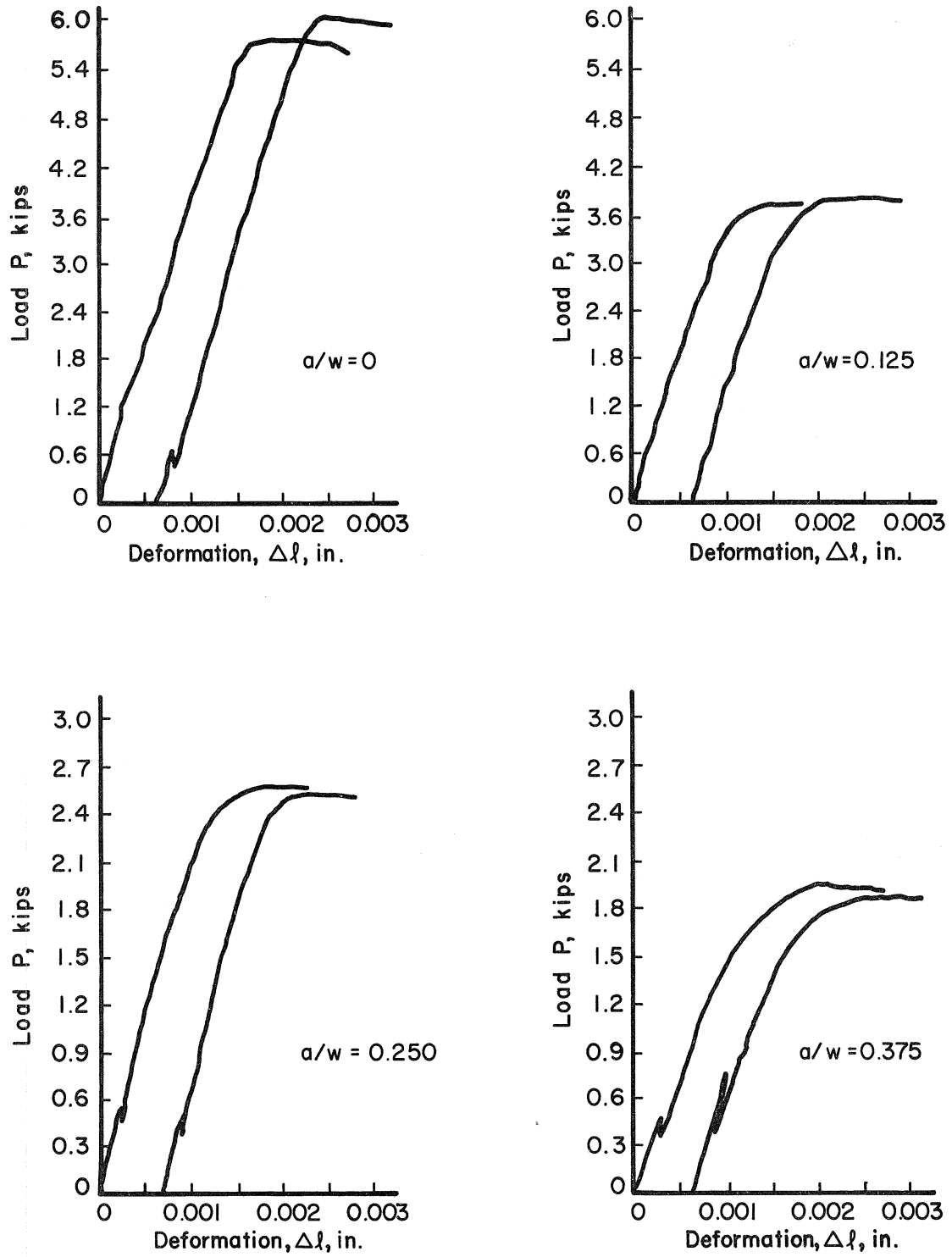


Fig.7 Typical Load-Deformation Curves: Concrete



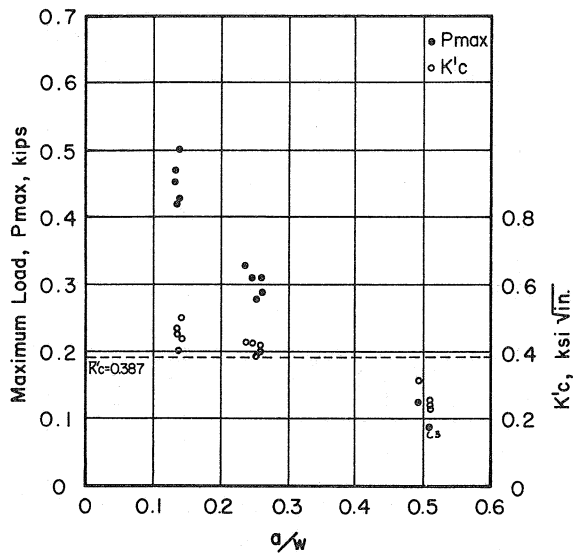


Fig. 8 Maximum Load and Effective Fracture Toughness vs  $a/w$ : Series 1

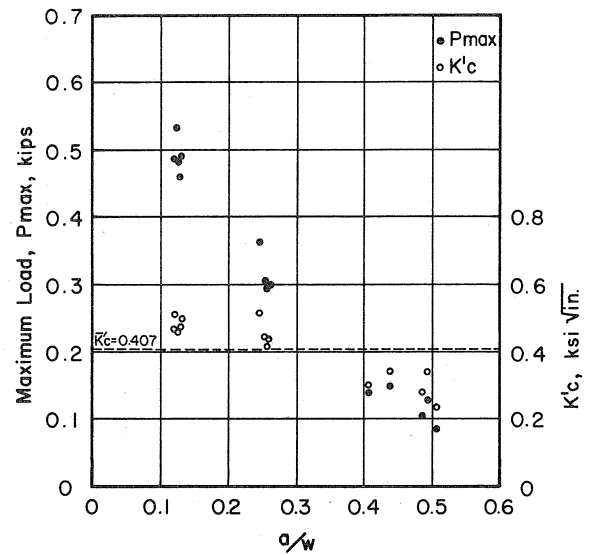


Fig. 9 Maximum Load and Effective Fracture Toughness vs  $a/w$ : Series 2

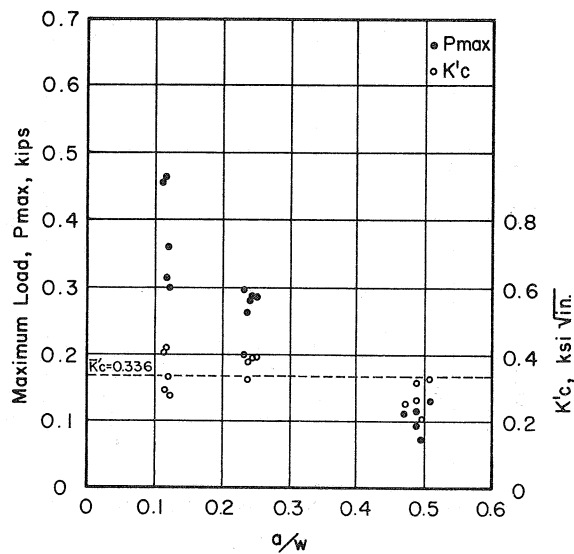


Fig. 10 Maximum Load and Effective Fracture Toughness vs  $a/w$ : Series 3

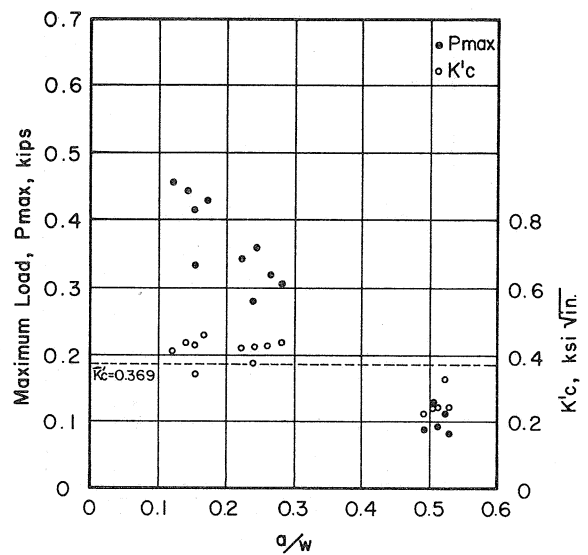


Fig. 11 Maximum Load and Effective Fracture Toughness vs  $a/w$ : Series 4

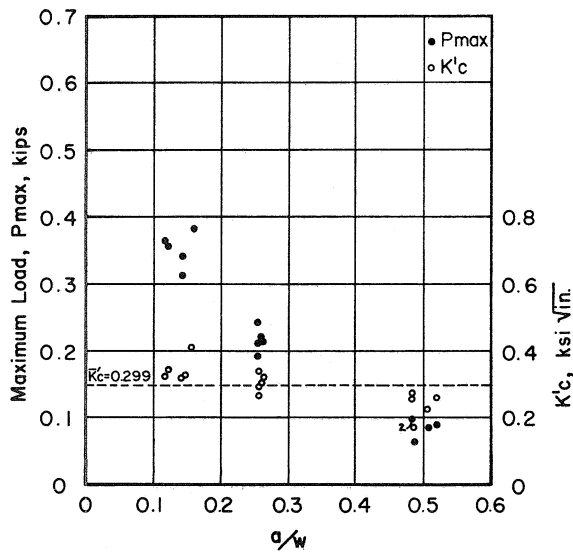


Fig. 12 Maximum Load and Effective Fracture Toughness vs  $a/w$ : Series 5

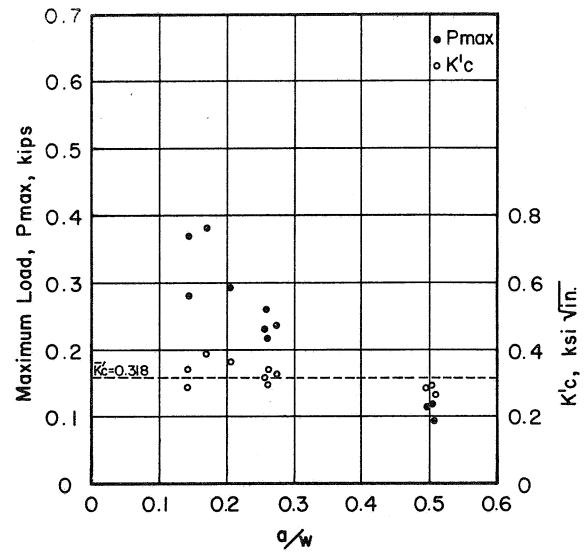


Fig. 13 Maximum Load and Effective Fracture Toughness vs  $a/w$ : Series 6

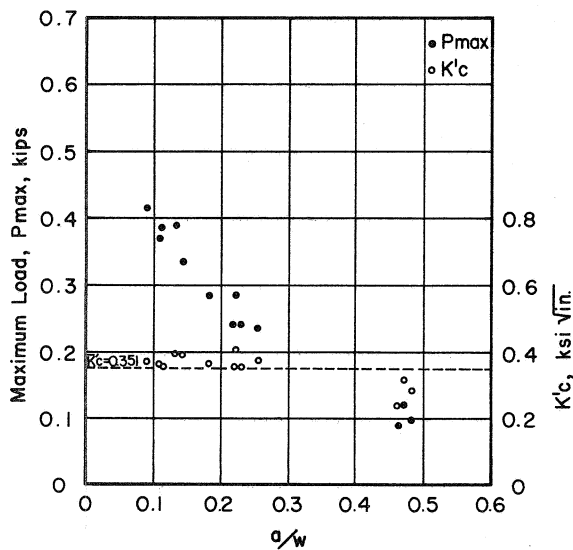


Fig. 14 Maximum Load and Effective Fracture Toughness vs  $a/w$ : Series 7

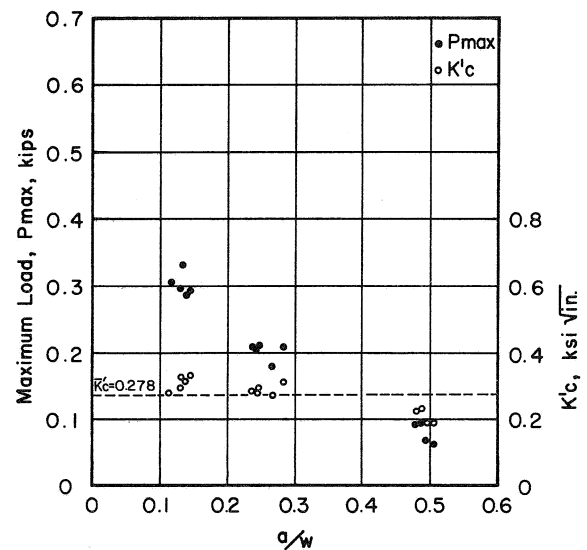


Fig. 15 Maximum Load and Effective Fracture Toughness vs  $a/w$ : Series 8

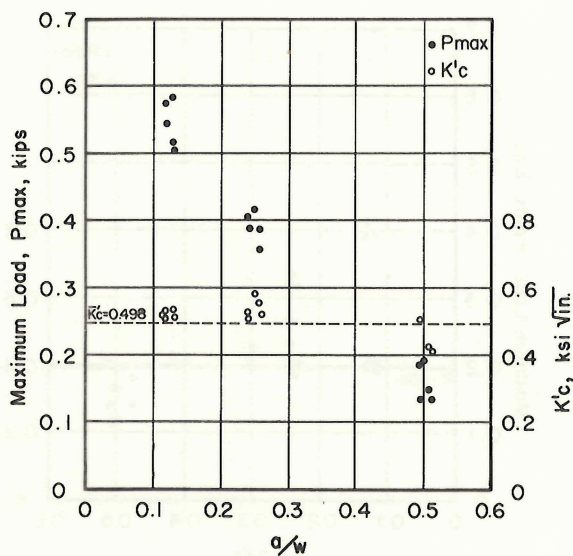


Fig. 16 Maximum Load and Effective Fracture Toughness vs  $a/w$ : Series 9

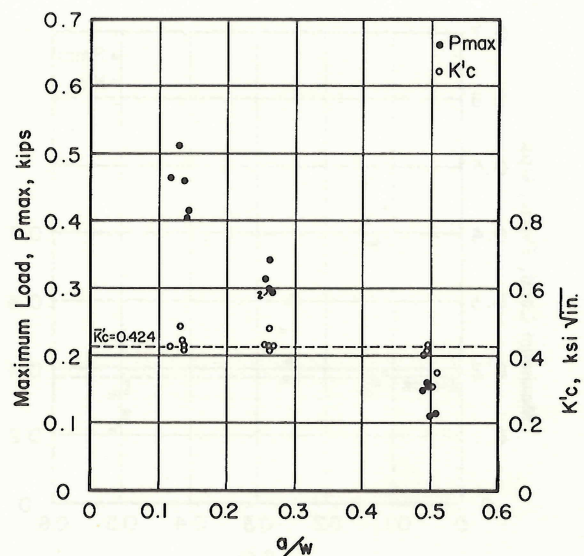


Fig. 17 Maximum Load and Effective Fracture Toughness vs  $a/w$ : Series 10

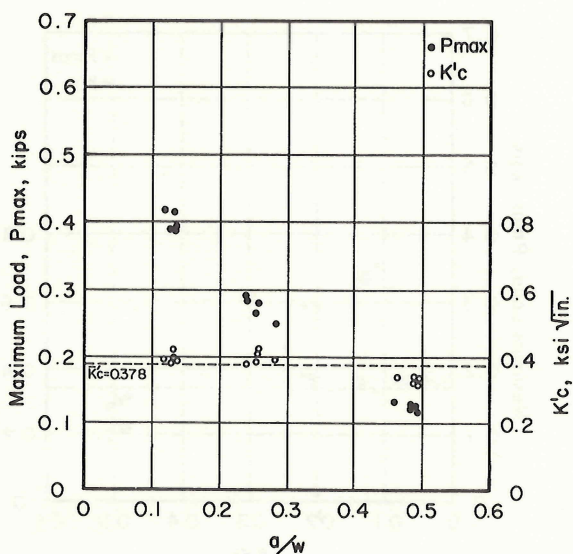


Fig. 18 Maximum Load and Effective Fracture Toughness vs  $a/w$ : Series 11

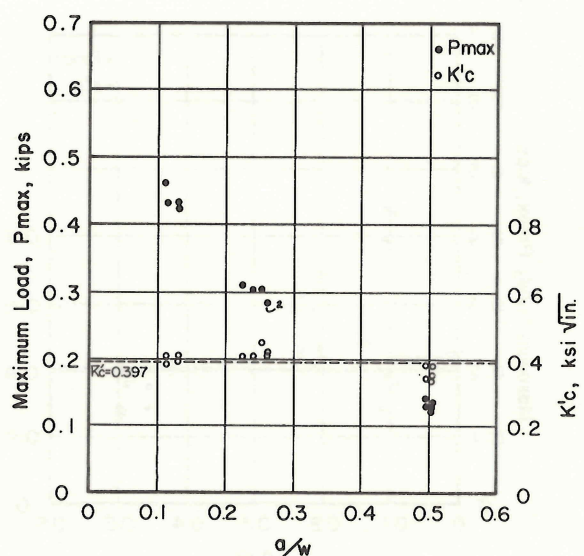


Fig. 19 Maximum Load and Effective Fracture Toughness vs  $a/w$ : Series 12

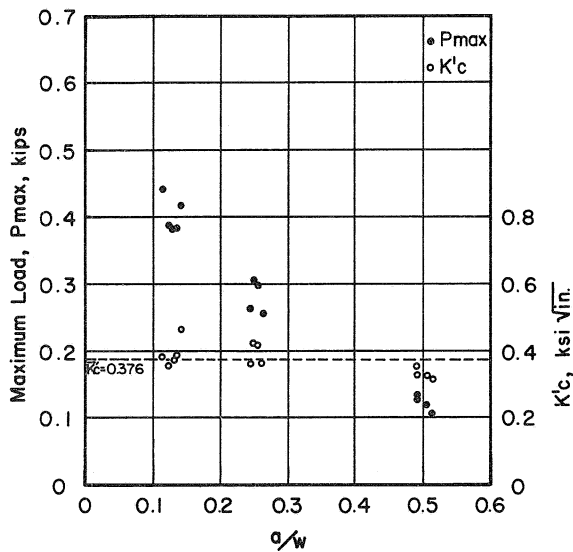


Fig. 20 Maximum Load and Effective Fracture Toughness vs  $a/w$ : Series I3

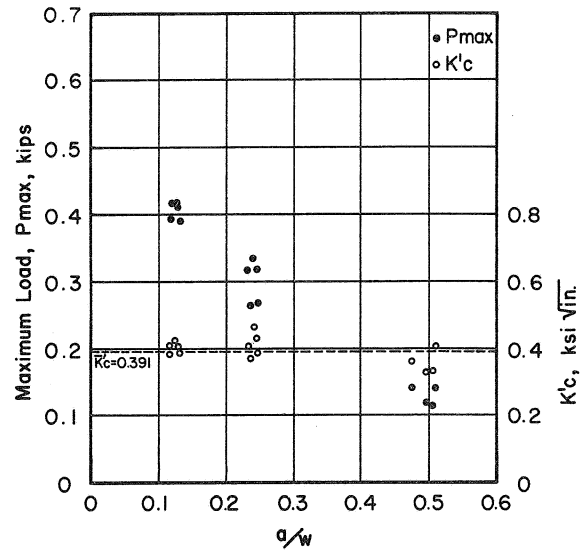


Fig. 21 Maximum Load and Effective Fracture Toughness vs  $a/w$ : Series I4

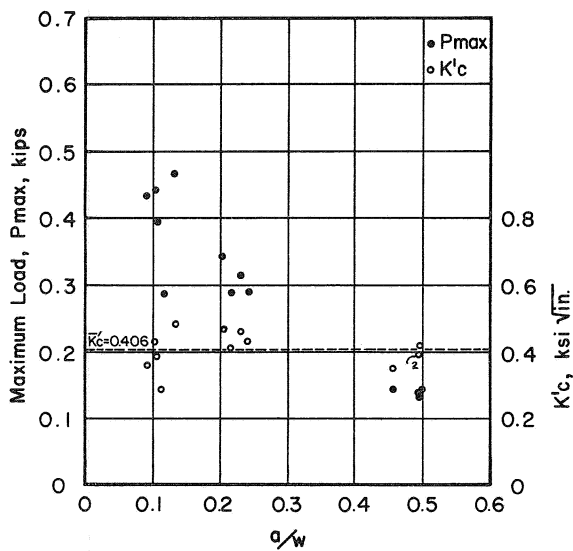


Fig. 22 Maximum Load and Effective Fracture Toughness vs  $a/w$ : Series I5

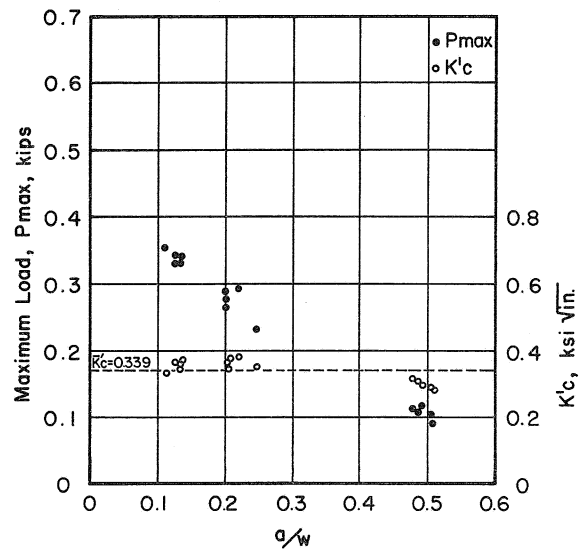


Fig. 23 Maximum Load and Effective Fracture Toughness vs  $a/w$ : Series I6

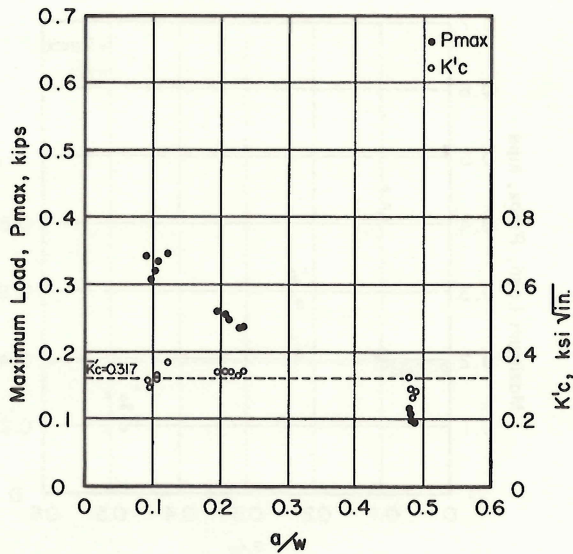


Fig. 24 Maximum Load and Effective Fracture Toughness vs  $a/w$ : Series 17

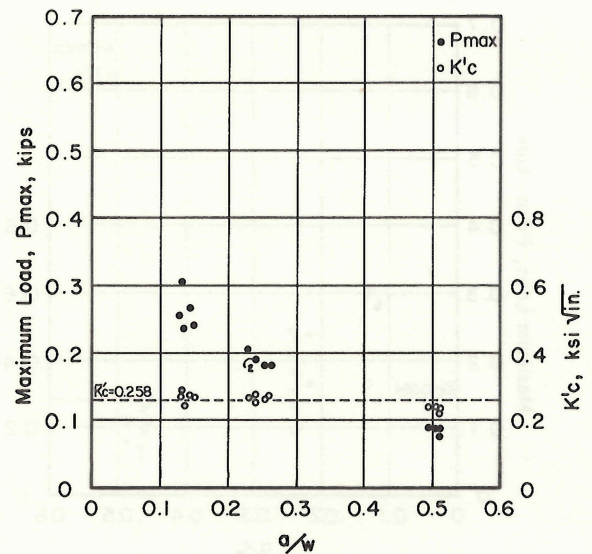


Fig. 25 Maximum Load and Effective Fracture Toughness vs  $a/w$ : Series 18

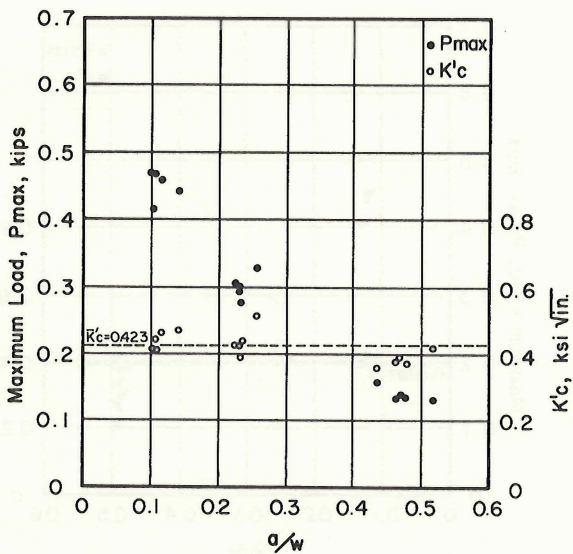


Fig. 26 Maximum Load and Effective Fracture Toughness vs  $a/w$ : Series 19

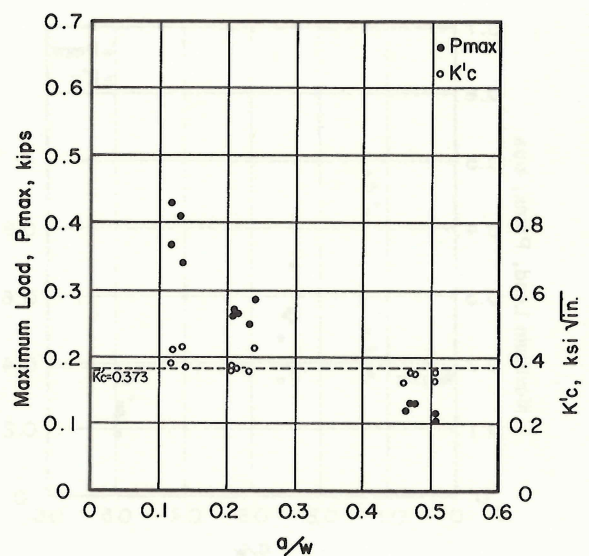


Fig. 27 Maximum Load and Effective Fracture Toughness vs  $a/w$ : Series 20



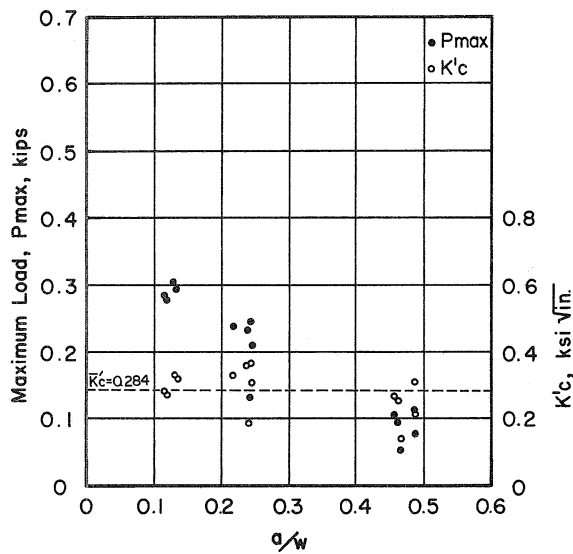


Fig. 28 Maximum Load and Effective Fracture Toughness vs  $a/w$ : Series 21

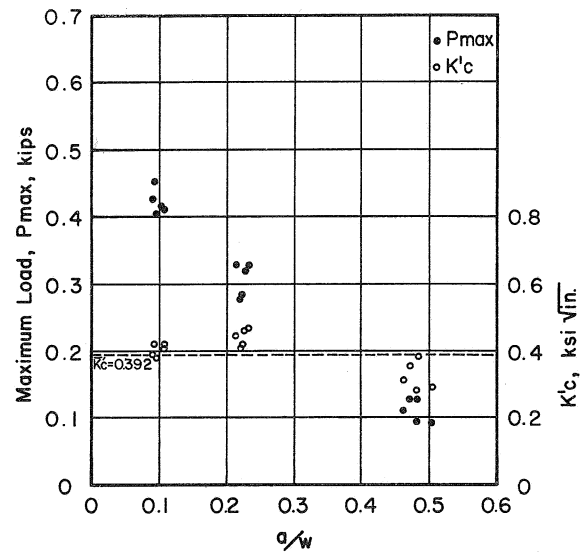


Fig. 29 Maximum Load and Effective Fracture Toughness vs  $a/w$ : Series 22

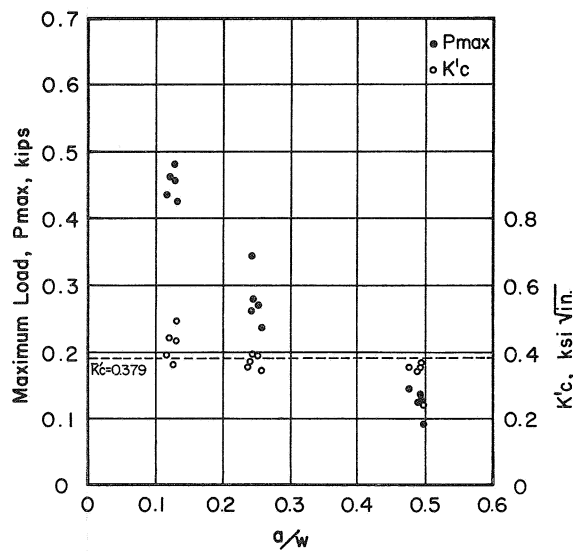


Fig. 30 Maximum Load and Effective Fracture Toughness vs  $a/w$ : Series 23

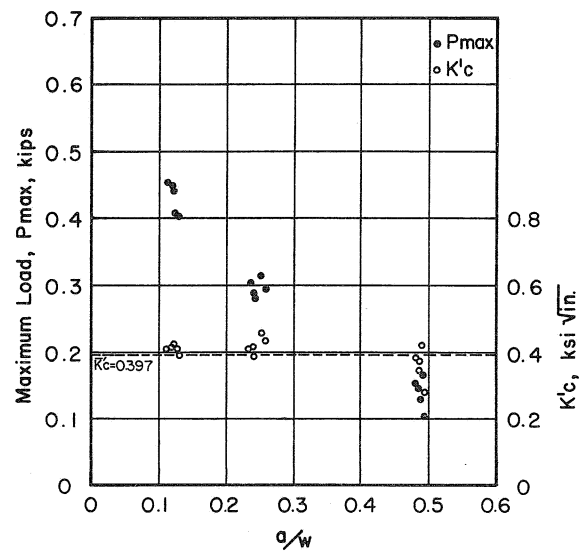


Fig. 31 Maximum Load and Effective Fracture Toughness vs  $a/w$ : Series 24

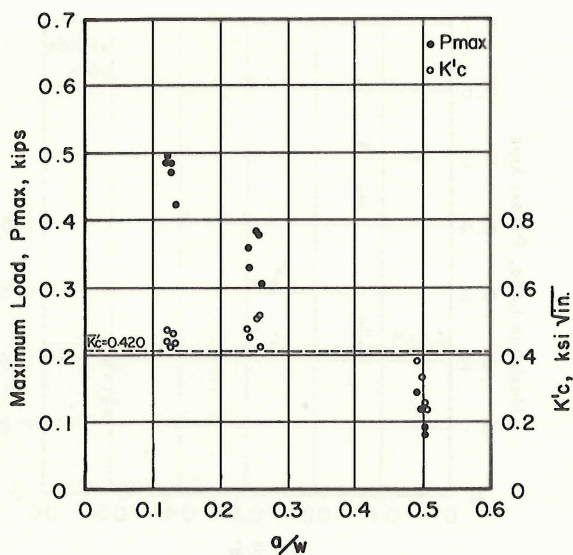


Fig. 32 Maximum Load and Effective Fracture Toughness vs  $a/w$ : Series 25

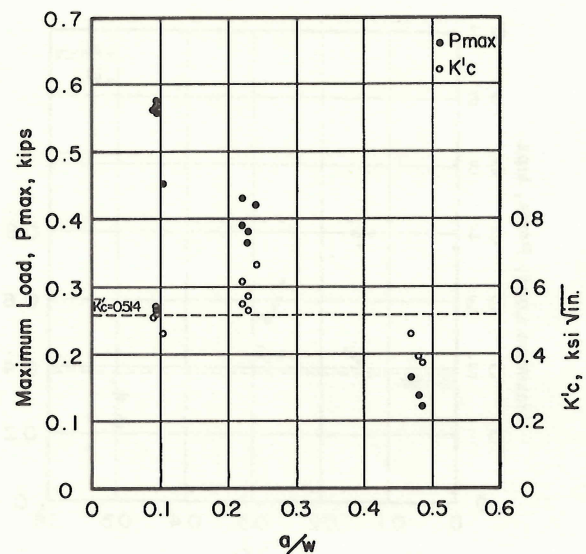


Fig. 33 Maximum Load and Effective Fracture Toughness vs  $a/w$ : Series 26

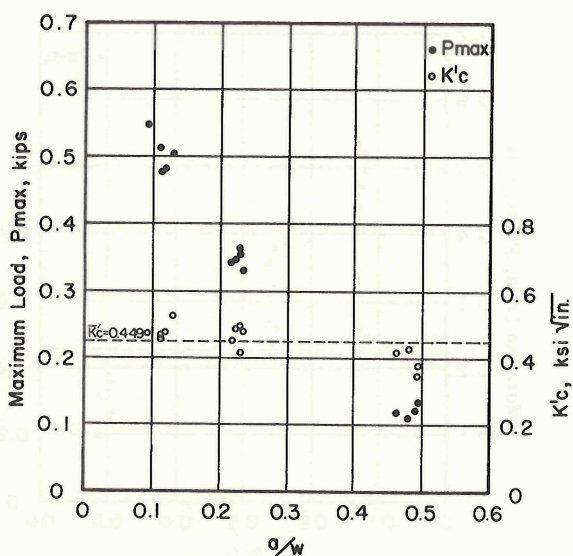


Fig. 34 Maximum Load and Effective Fracture Toughness vs  $a/w$ : Series 27

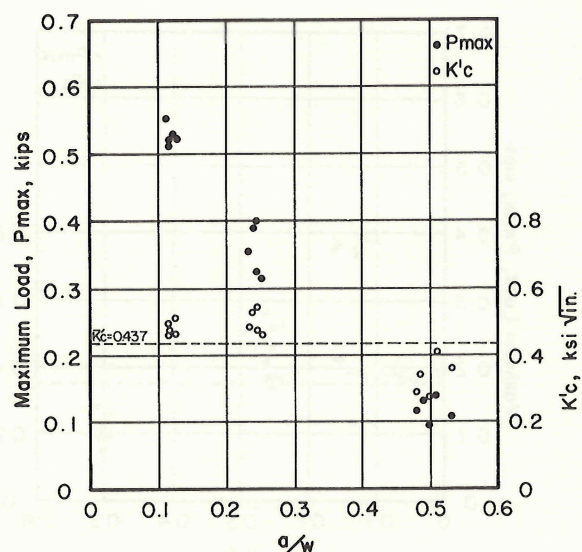


Fig. 35 Maximum Load and Effective Fracture Toughness vs  $a/w$ : Series 28

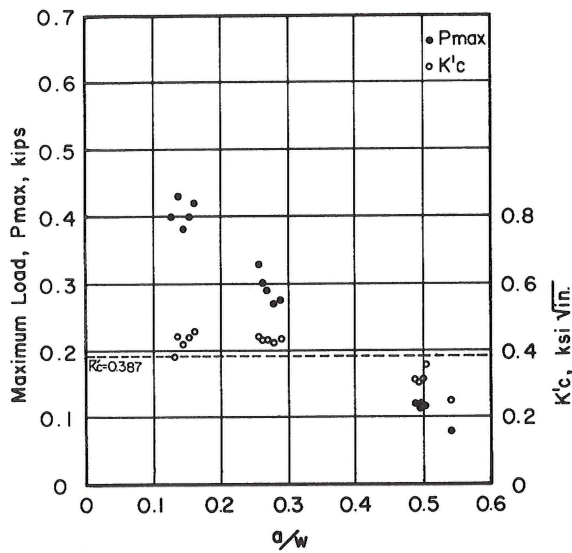


Fig. 36 Maximum Load and Effective Fracture Toughness vs  $a/w$ : Series 29

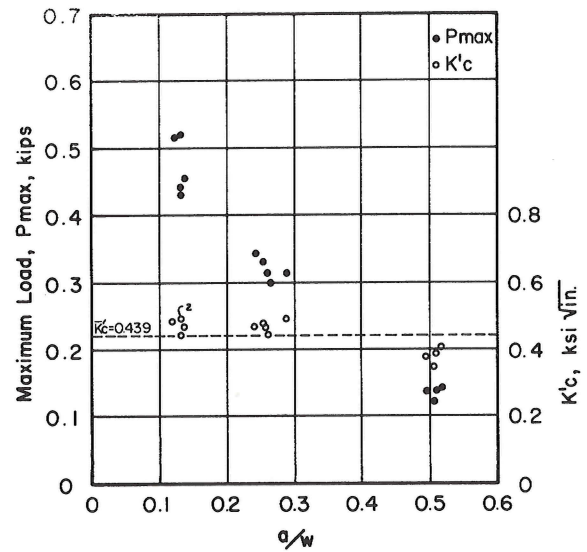


Fig. 37 Maximum Load and Effective Fracture Toughness vs  $a/w$ : Series 30

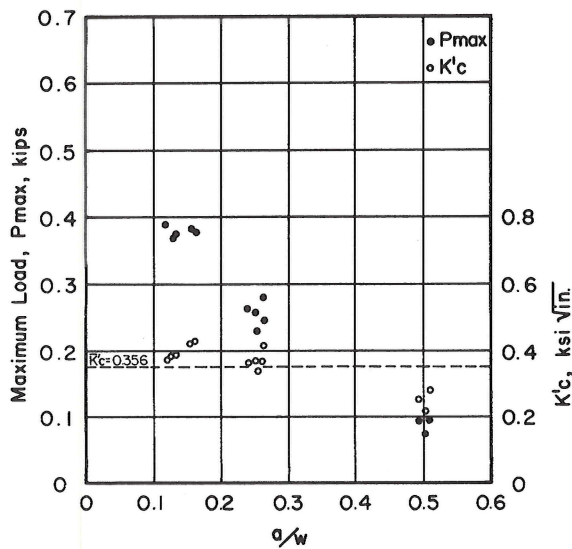


Fig. 38 Maximum Load and Effective Fracture Toughness vs  $a/w$ : Series 31

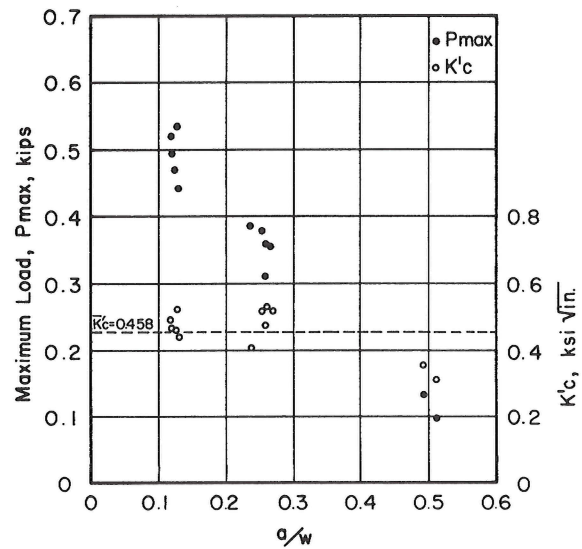
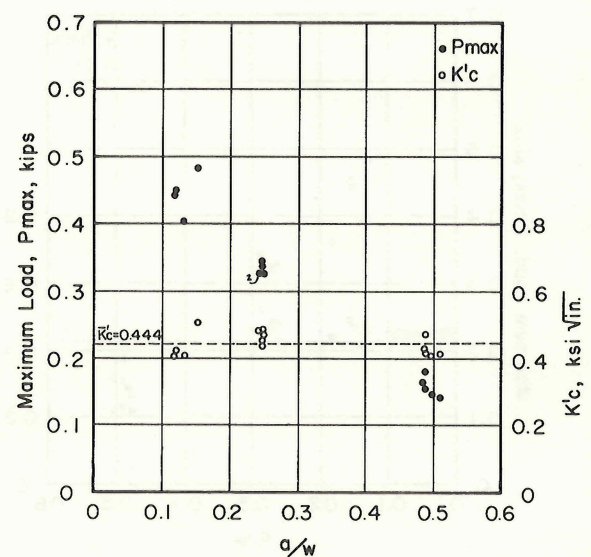
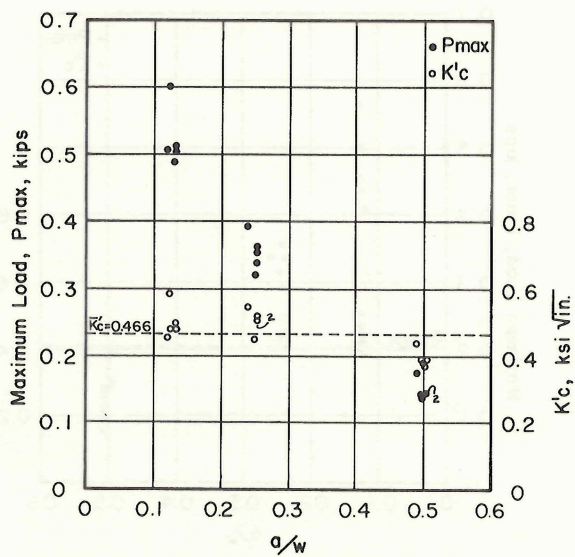
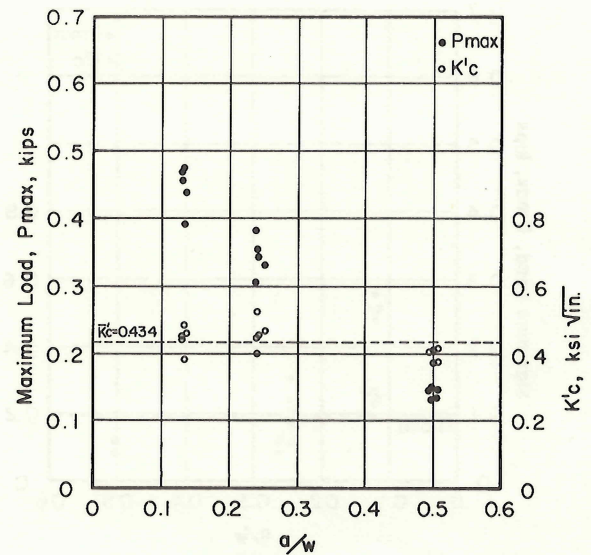
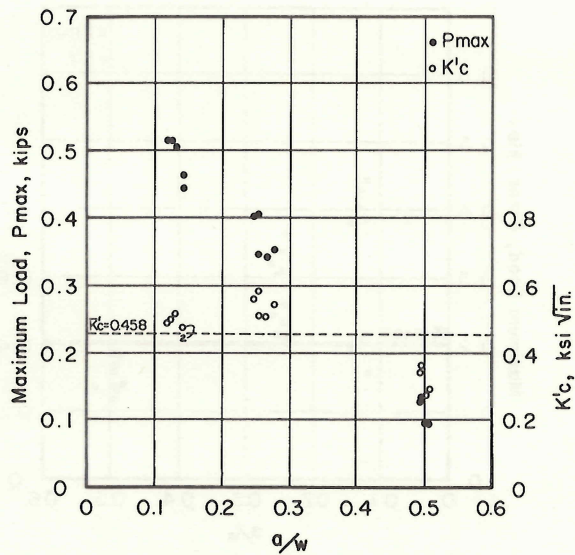


Fig. 39 Maximum Load and Effective Fracture Toughness vs  $a/w$ : Series 32



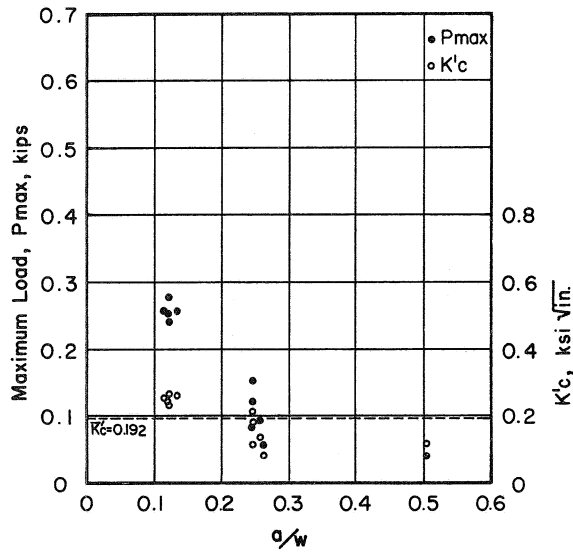


Fig. 44 Maximum Load and Effective Fracture Toughness vs  $a/w$ : Series 37

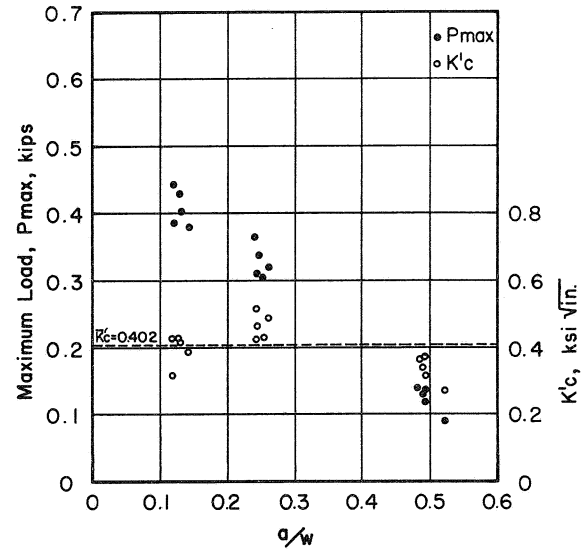


Fig. 45 Maximum Load and Effective Fracture Toughness vs  $a/w$ : Series 38

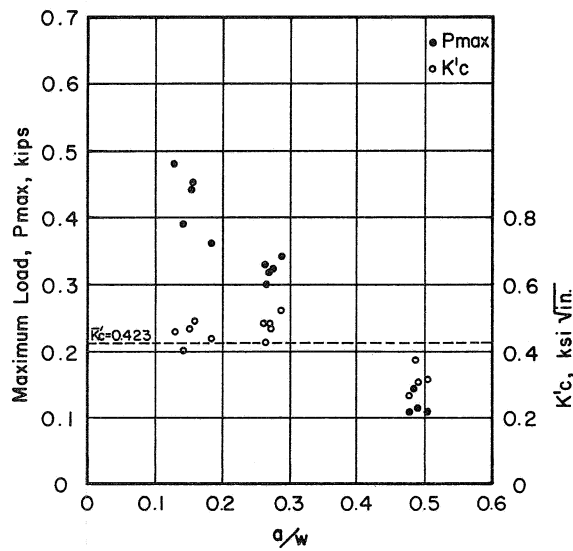


Fig. 46 Maximum Load and Effective Fracture Toughness vs  $a/w$ : Series 39

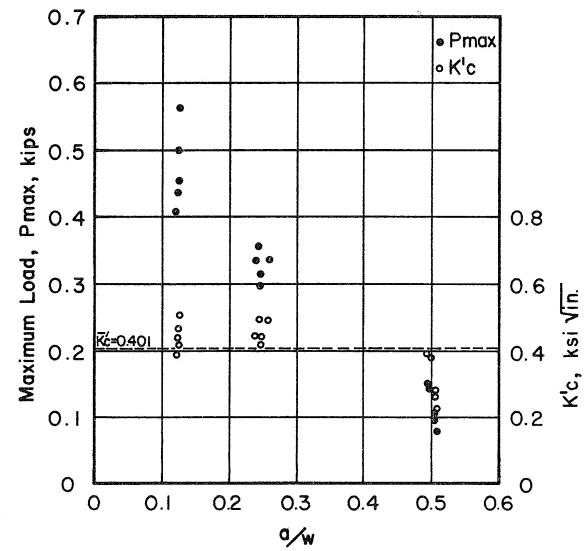


Fig. 47 Maximum Load and Effective Fracture Toughness vs  $a/w$ : Series 40



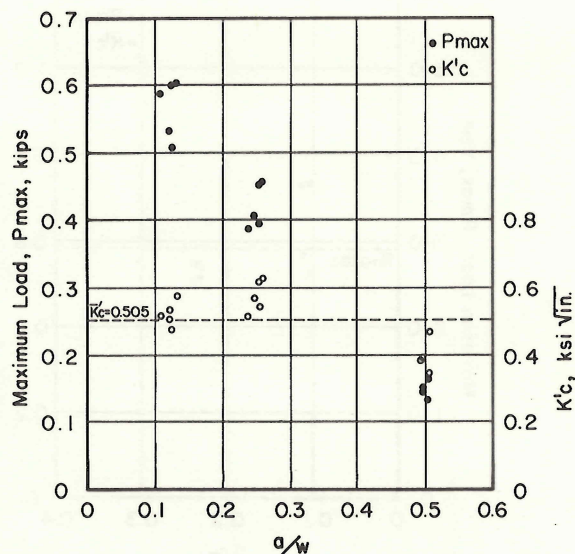


Fig. 48 Maximum Load and Effective Fracture Toughness vs  $a/w$ : Series 41

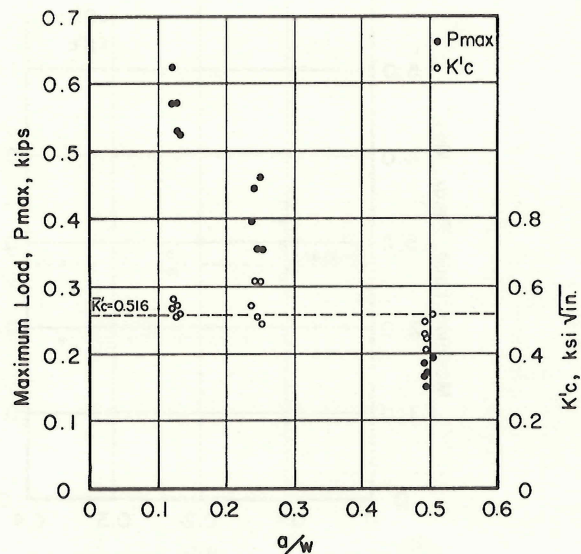


Fig. 49 Maximum Load and Effective Fracture Toughness vs  $a/w$ : Series 42

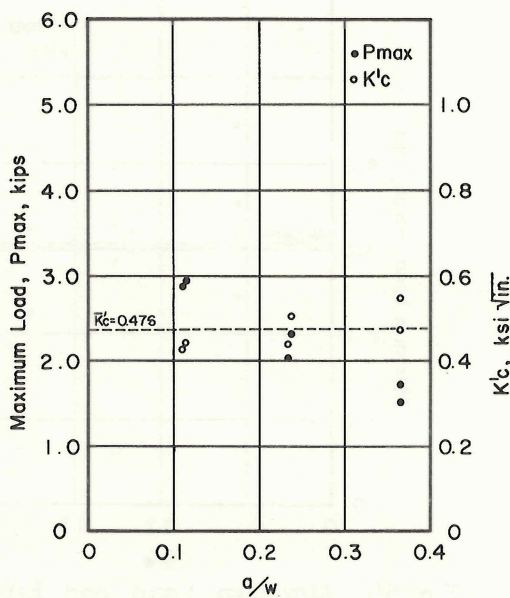


Fig. 50 Maximum Load and Effective Fracture Toughness vs  $a/w$ : Series 43

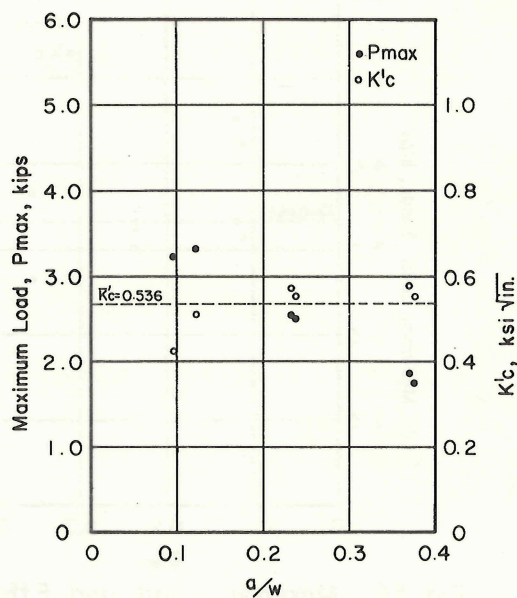


Fig. 51 Maximum Load and Effective Fracture Toughness vs  $a/w$ : Series 44

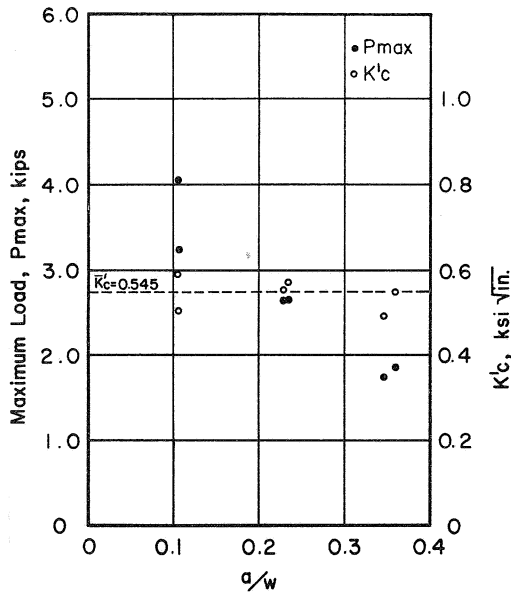


Fig. 52 Maximum Load and Effective Fracture Toughness vs  $a/w$ : Series 45

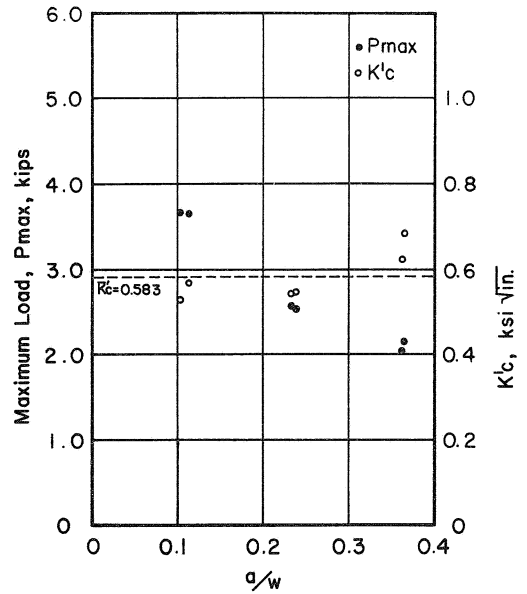


Fig. 53 Maximum Load and Effective Fracture Toughness vs  $a/w$ : Series 46

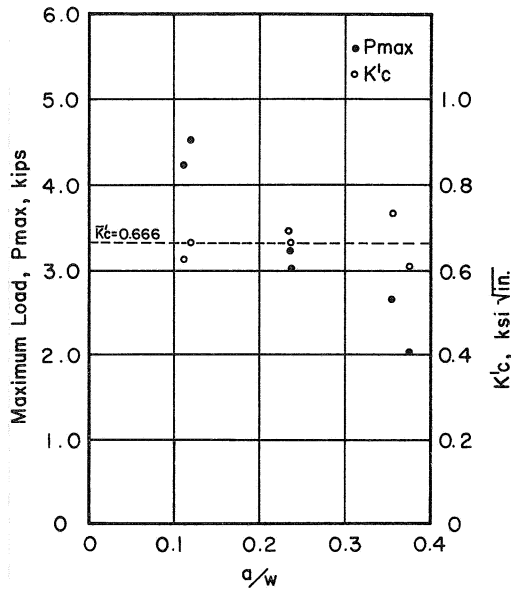


Fig. 54 Maximum Load and Effective Fracture Toughness vs  $a/w$ : Series 47

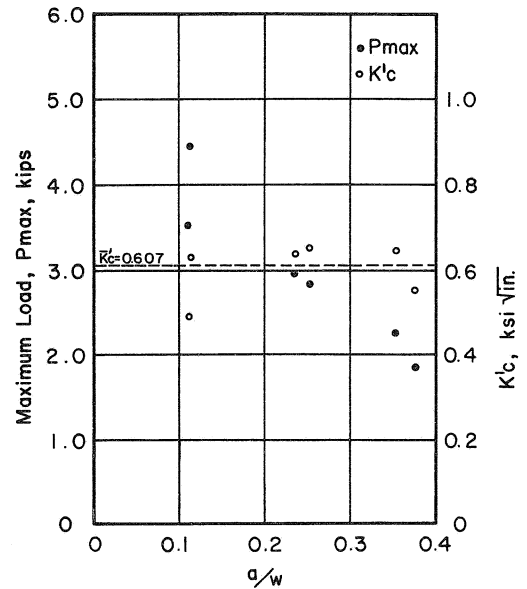


Fig. 55 Maximum Load and Effective Fracture Toughness vs  $a/w$ : Series 48

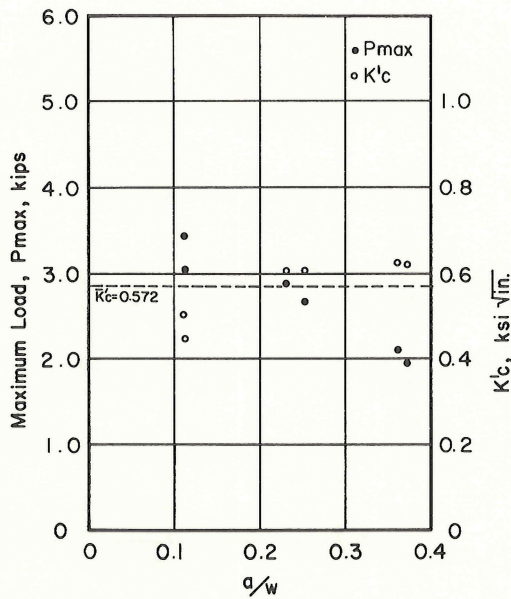


Fig. 56 Maximum Load and Effective Fracture Toughness vs  $q/w$ : Series 49

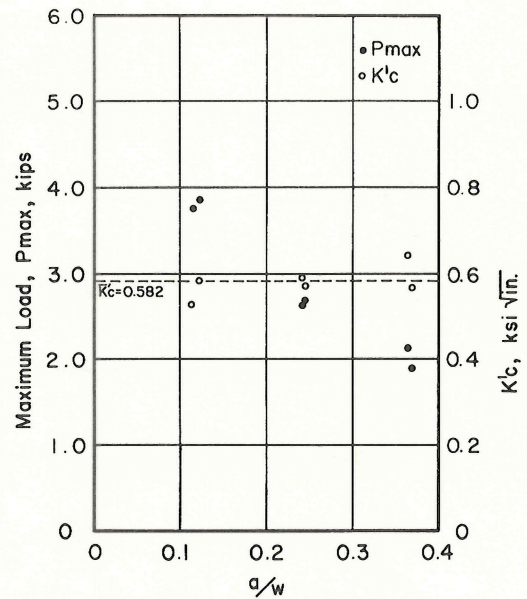


Fig. 57 Maximum Load and Effective Fracture Toughness vs  $q/w$ : Series 50

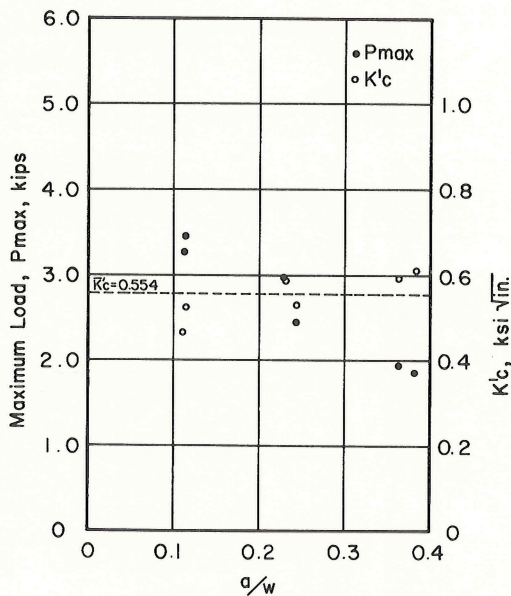


Fig. 58 Maximum Load and Effective Fracture Toughness vs  $q/w$ : Series 51

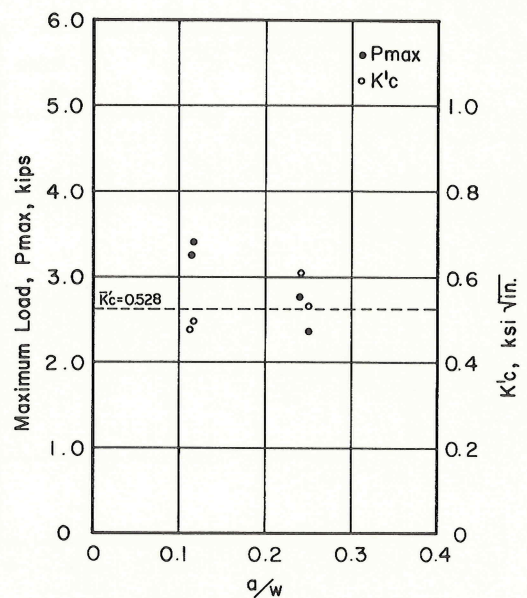


Fig. 59 Maximum Load and Effective Fracture Toughness vs  $q/w$ : Series 52

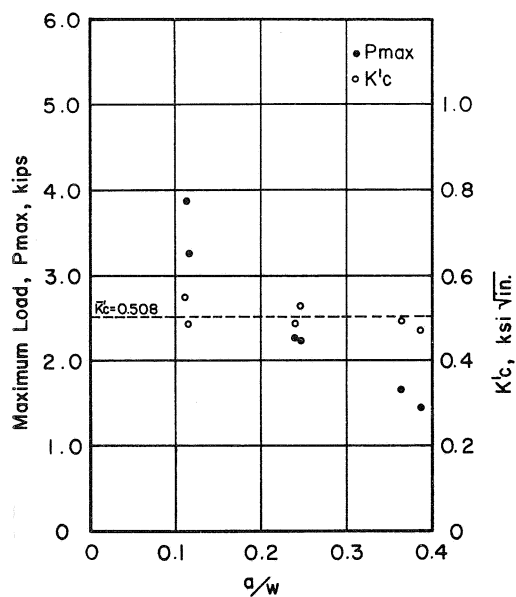


Fig. 60 Maximum Load and Effective Fracture Toughness vs  $a/w$ : Series 53

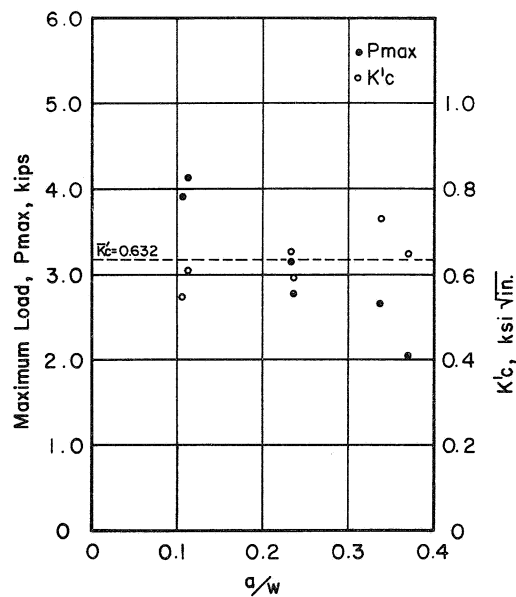


Fig. 61 Maximum Load and Effective Fracture Toughness vs  $a/w$ : Series 54

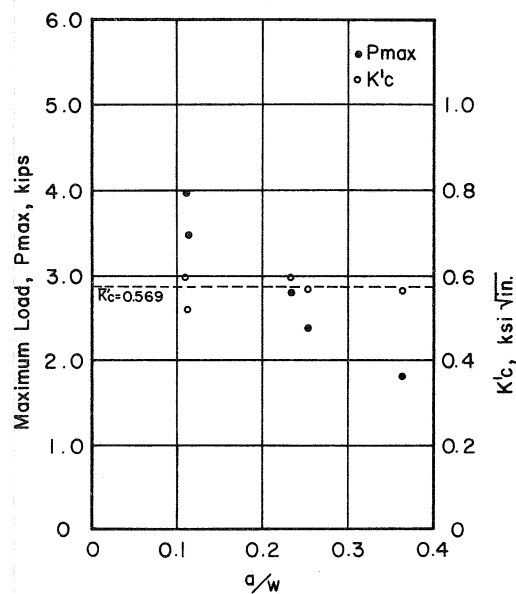


Fig. 62 Maximum Load and Effective Fracture Toughness vs  $a/w$ : Series 55

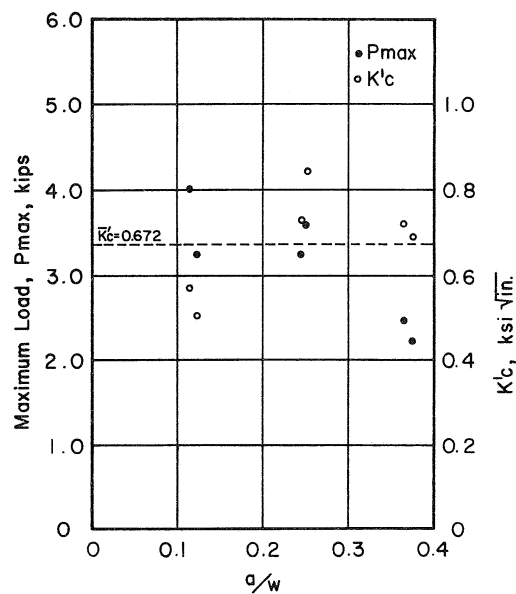


Fig. 63 Maximum Load and Effective Fracture Toughness vs  $a/w$ : Series 56

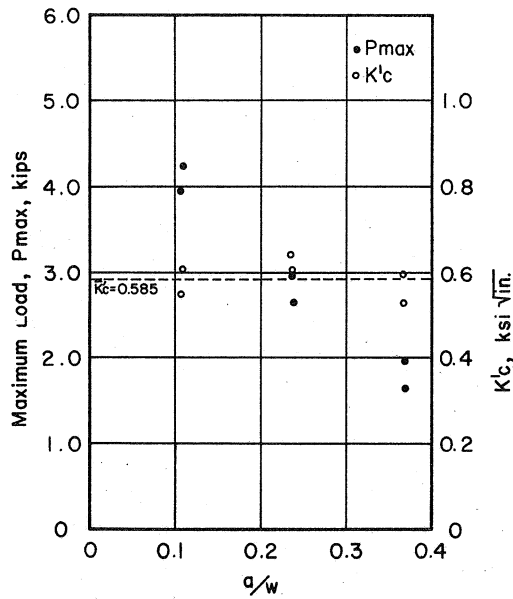


Fig. 64 Maximum Load and Effective Fracture Toughness vs  $a/w$ : Series 57

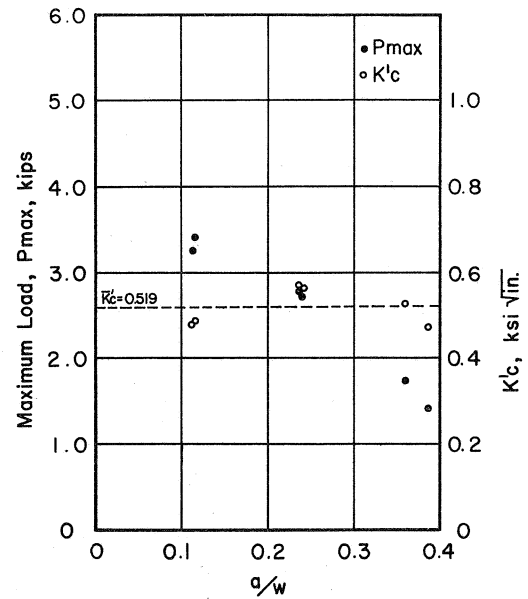


Fig. 65 Maximum Load and Effective Fracture Toughness vs  $a/w$ : Series 58

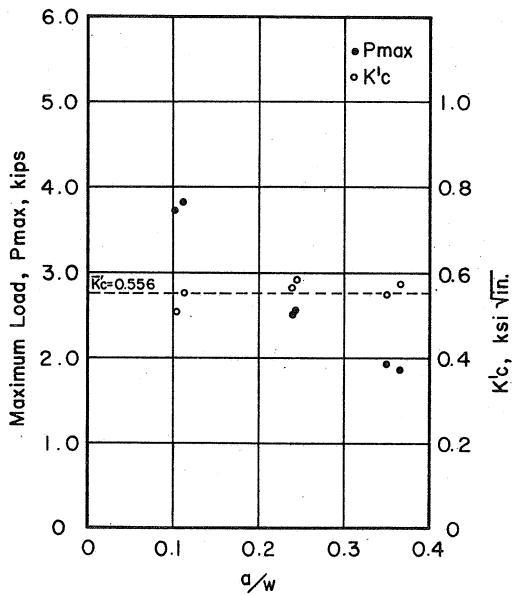


Fig. 66 Maximum Load and Effective Fracture Toughness vs  $a/w$ : Series 59

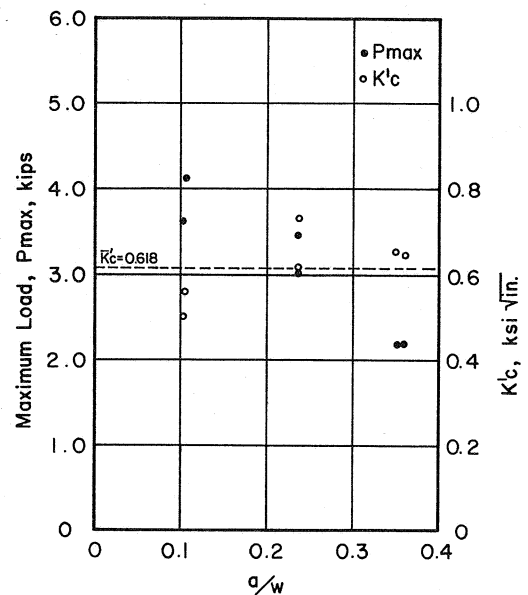


Fig. 67 Maximum Load and Effective Fracture Toughness vs  $a/w$ : Series 60



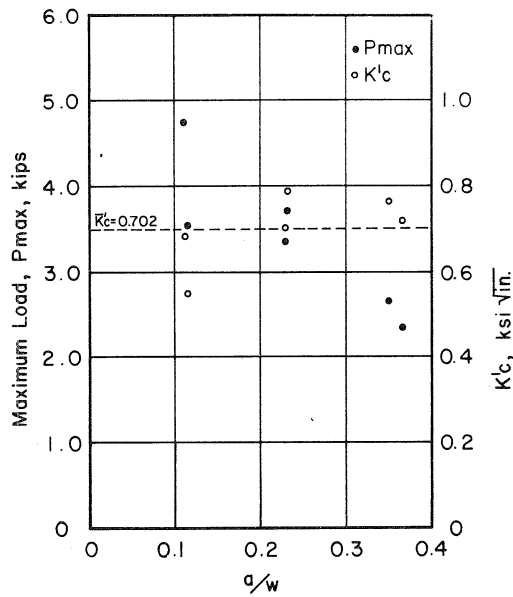


Fig. 68 Maximum Load and Effective Fracture Toughness vs  $a/w$ : Series 61

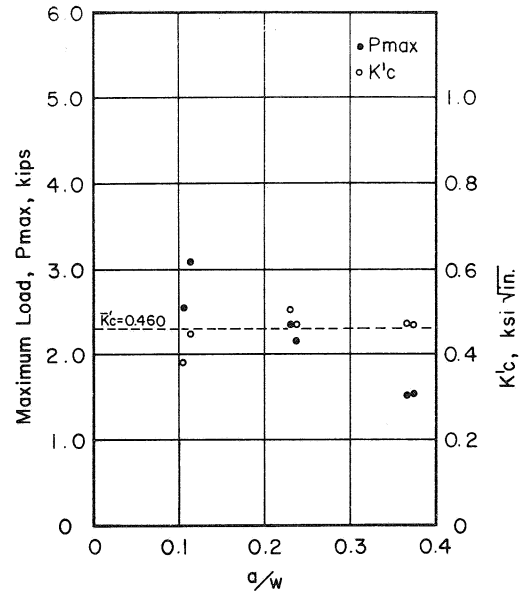


Fig. 69 Maximum Load and Effective Fracture Toughness vs  $a/w$ : Series 62

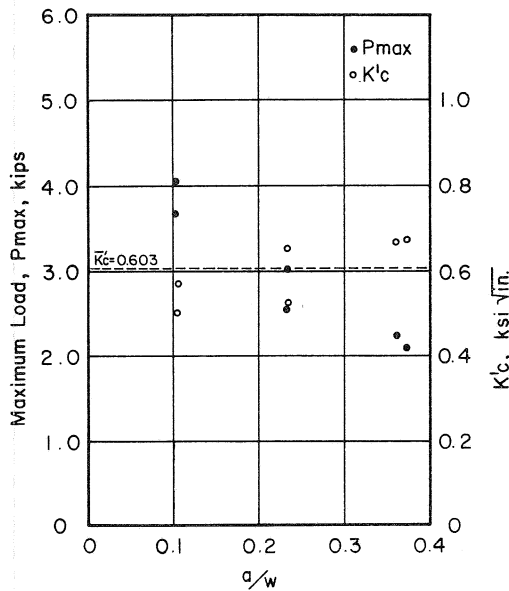


Fig. 70 Maximum Load and Effective Fracture Toughness vs  $a/w$ : Series 63

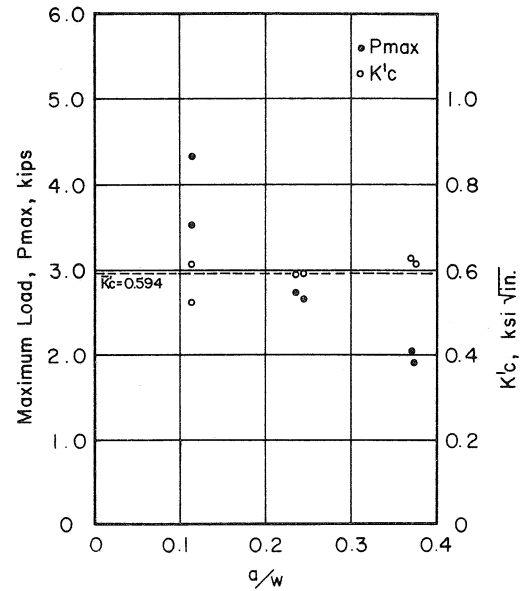


Fig. 71 Maximum Load and Effective Fracture Toughness vs  $a/w$ : Series 64

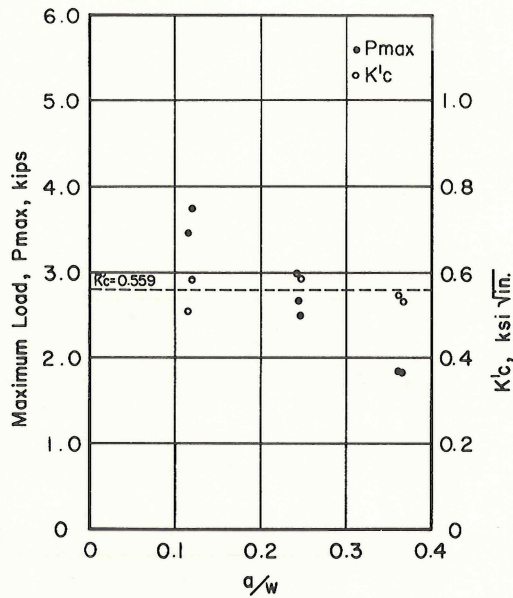


Fig. 72 Maximum Load and Effective Fracture Toughness vs  $a/w$ : Series 65

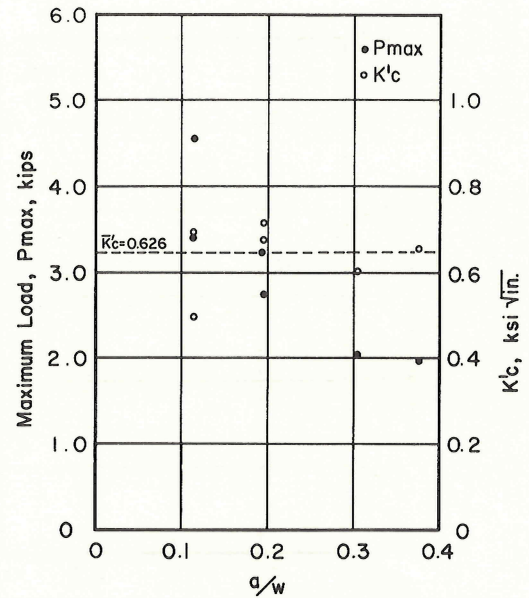


Fig. 73 Maximum Load and Effective Fracture Toughness vs  $a/w$ : Series 66

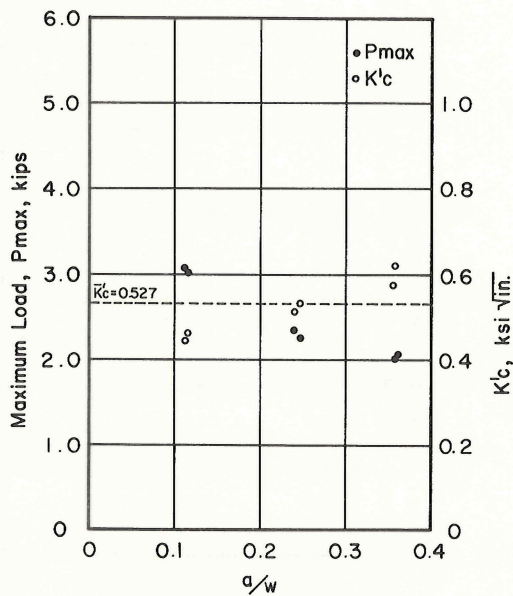


Fig. 74 Maximum Load and Effective Fracture Toughness vs  $a/w$ : Series 67

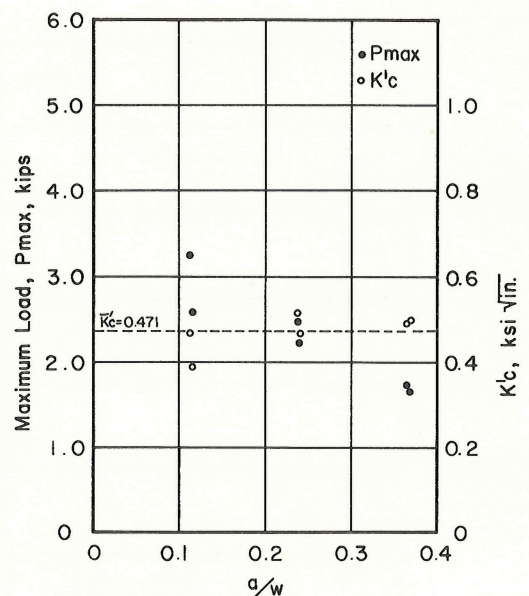


Fig. 75 Maximum Load and Effective Fracture Toughness vs  $a/w$ : Series 68

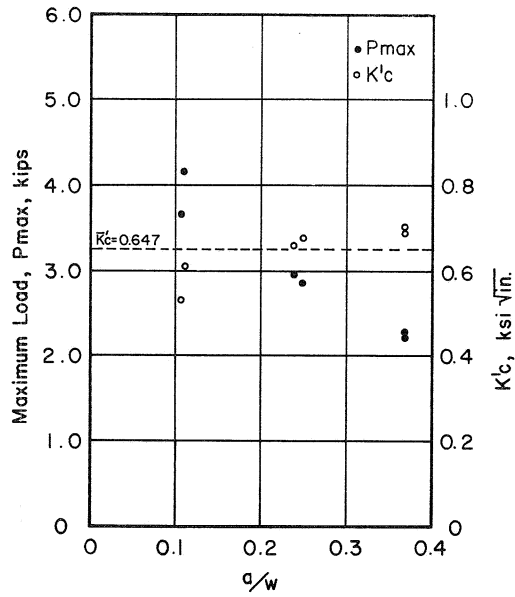


Fig. 76 Maximum Load and Effective Fracture Toughness vs  $a/w$ : Series 69

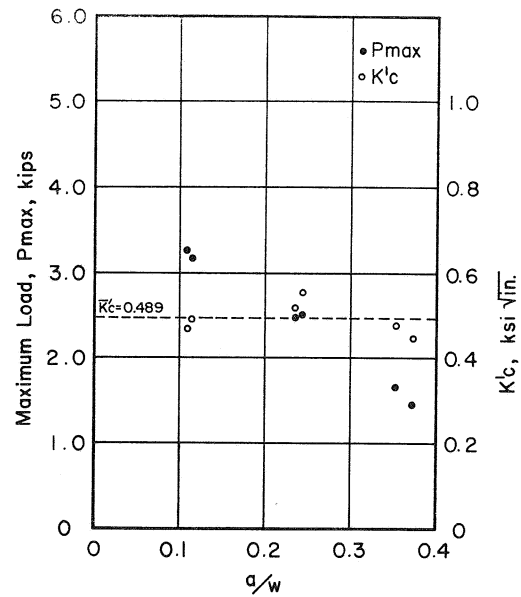


Fig. 77 Maximum Load and Effective Fracture Toughness vs  $a/w$ : Series 70

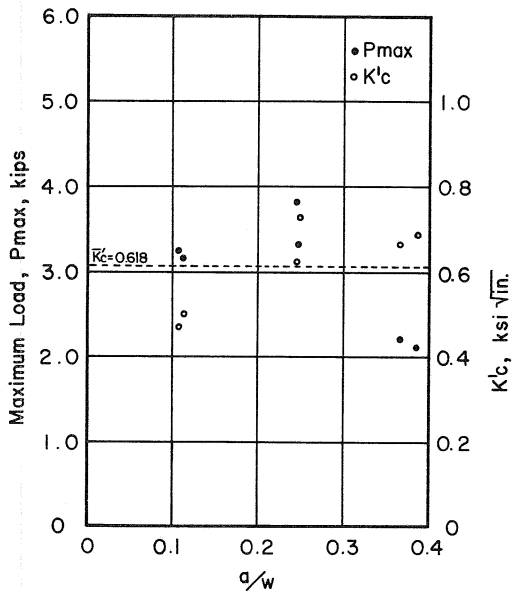


Fig. 78 Maximum Load and Effective Fracture Toughness vs  $a/w$ : Series 71

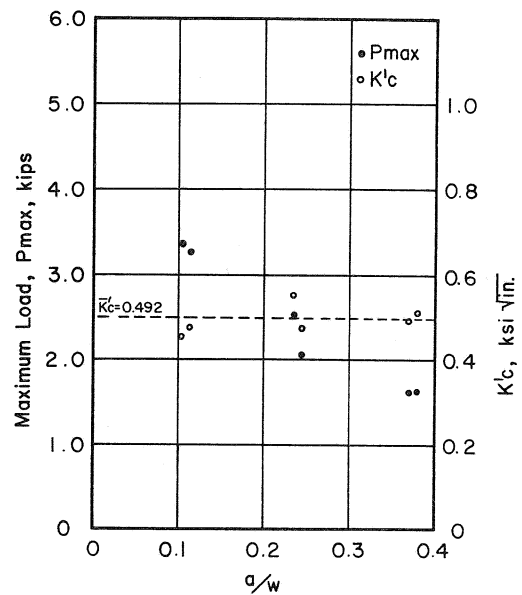


Fig. 79 Maximum Load and Effective Fracture Toughness vs  $a/w$ : Series 72

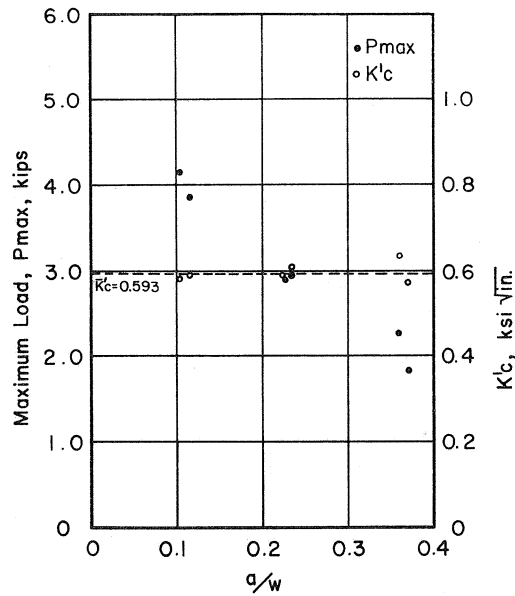


Fig. 80 Maximum Load and Effective Fracture Toughness vs  $a/w$ : Series 73

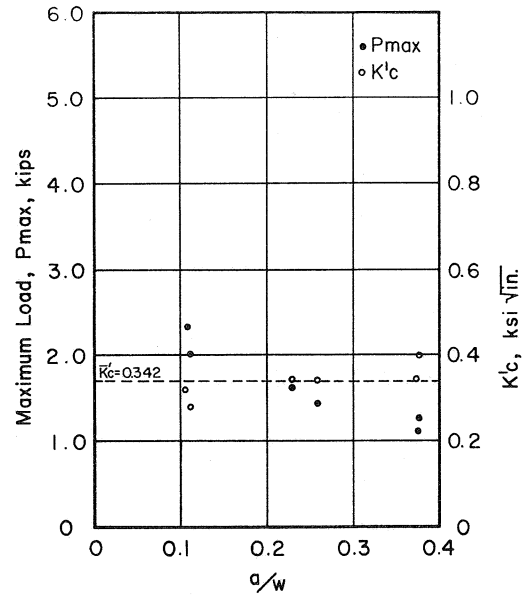


Fig. 81 Maximum Load and Effective Fracture Toughness vs  $q/w$ : Series 74

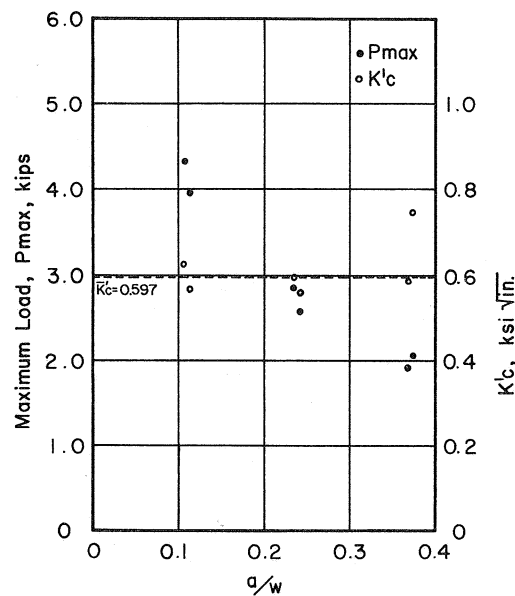


Fig. 82 Maximum Load and Effective Fracture Toughness vs  $a/w$ : Series 75

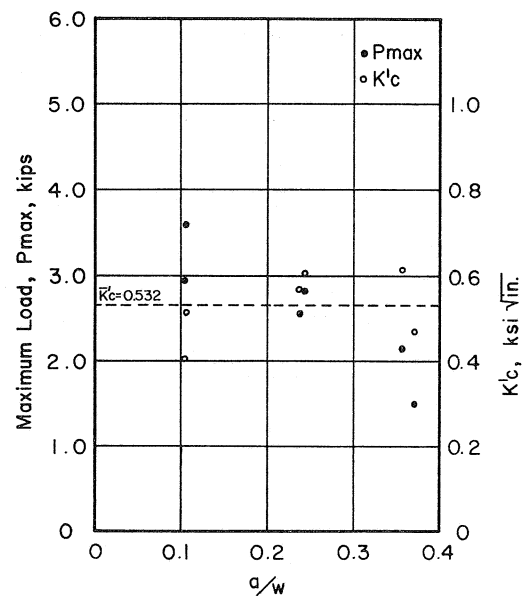


Fig. 83 Maximum Load and Effective Fracture Toughness vs  $a/w$ : Series 76

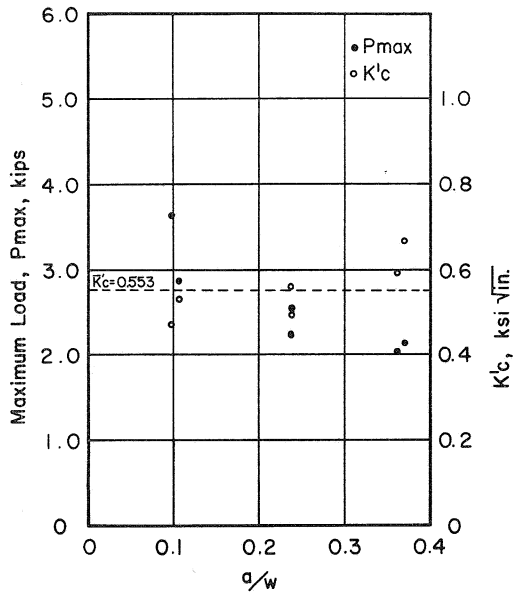


Fig. 84 Maximum Load and Effective Fracture Toughness vs  $a/w$ : Series 77

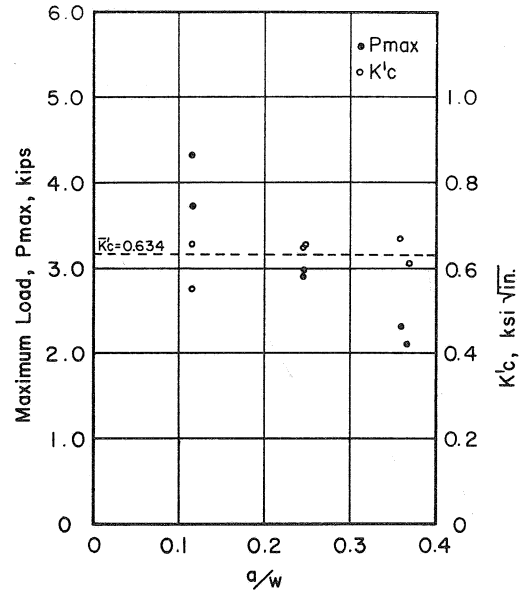


Fig. 85 Maximum Load and Effective Fracture Toughness vs  $a/w$ : Series 78

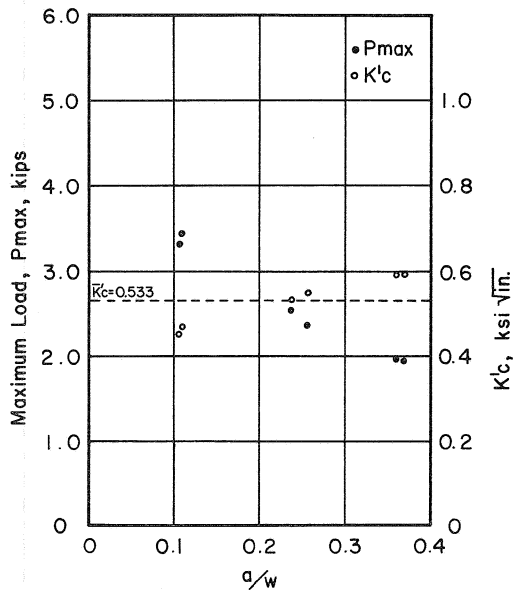


Fig. 86 Maximum Load and Effective Fracture Toughness vs  $a/w$ : Series 79

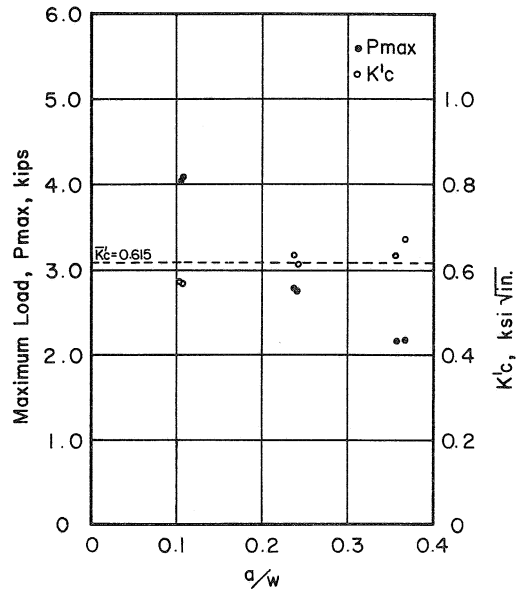


Fig. 87 Maximum Load and Effective Fracture Toughness vs  $a/w$ : Series 80

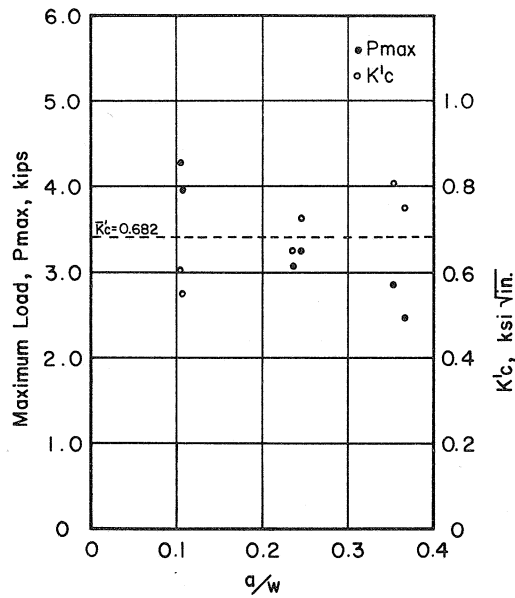


Fig. 88 Maximum Load and Effective Fracture Toughness vs  $a/w$ : Series 81

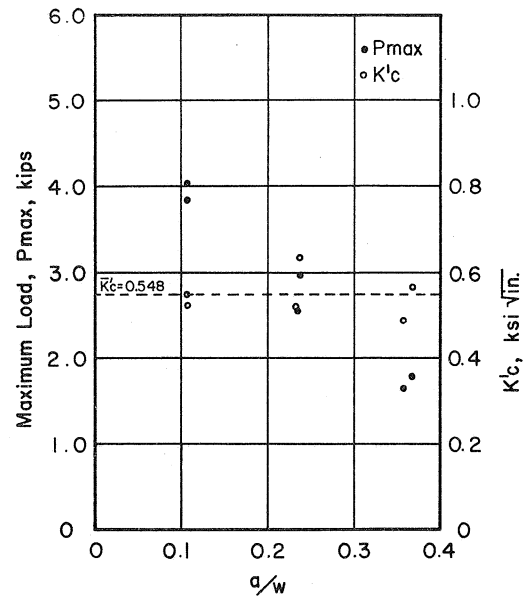


Fig. 89 Maximum Load and Effective Fracture Toughness vs  $a/w$ : Series 82

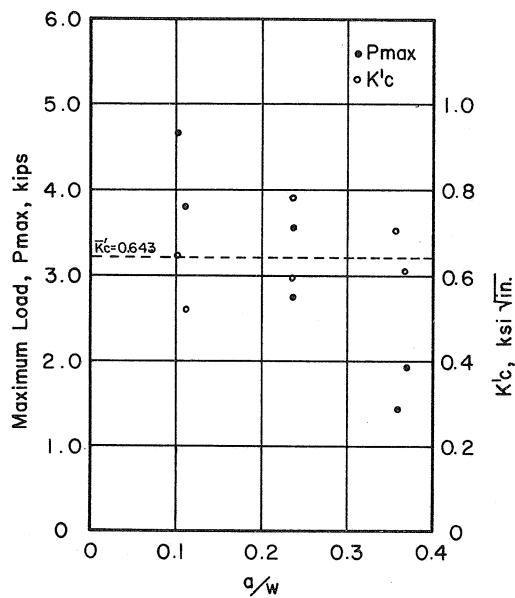


Fig. 90 Maximum Load and Effective Fracture Toughness vs  $a/w$ : Series 83

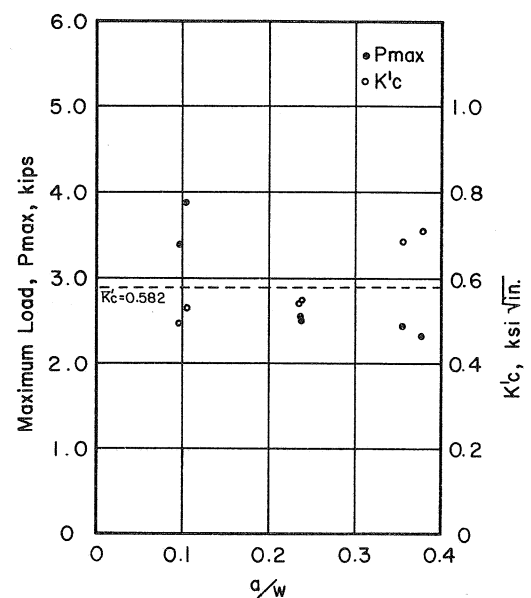


Fig. 91 Maximum Load and Effective Fracture Toughness vs  $a/w$ : Series 84



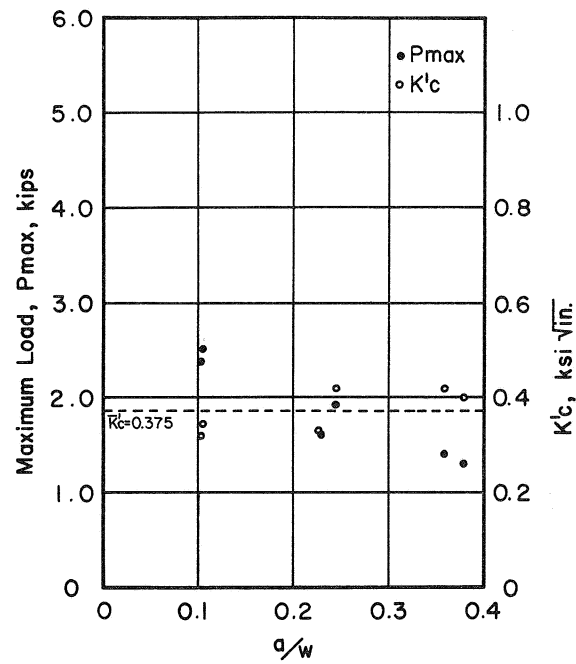


Fig. 92 Maximum Load and Effective Fracture Toughness vs  $q/w$ : Series 85

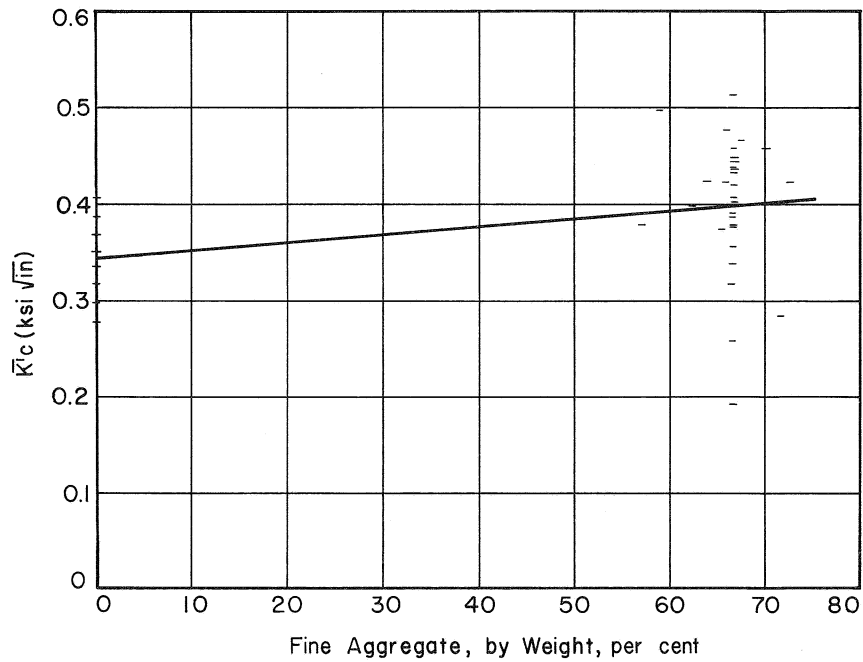


Fig. 93 Effect of Fine Aggregate on  $K'c$ : Pastes and Mortars, All Series

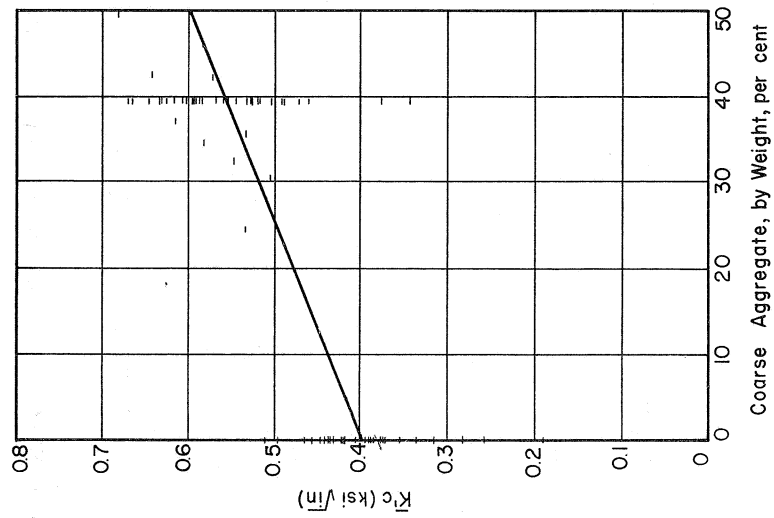


Fig. 94 Effect of Coarse Aggregate on  $K'_c$ : Mortars and Concretes, All Series

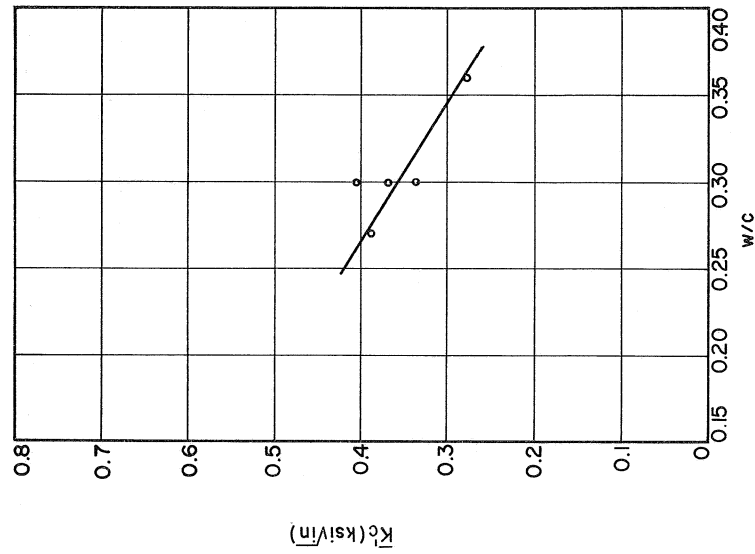


Fig. 95 Effect of w/c Ratio on  $K'_c$ : Pastes

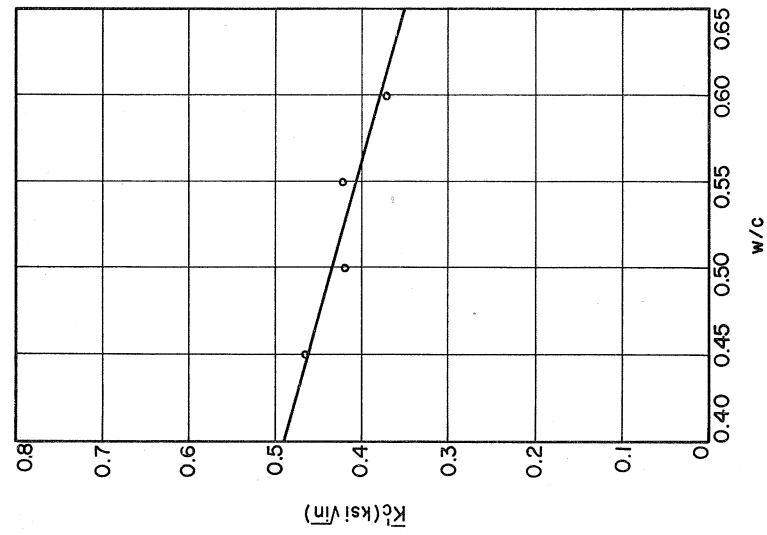
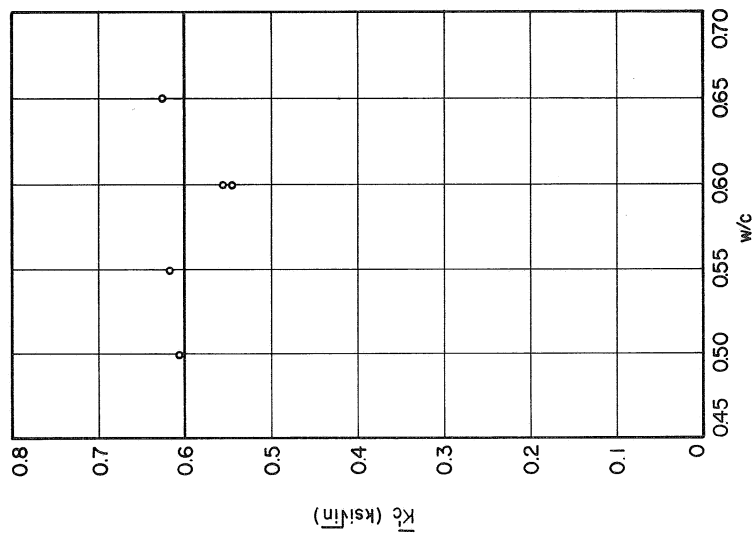
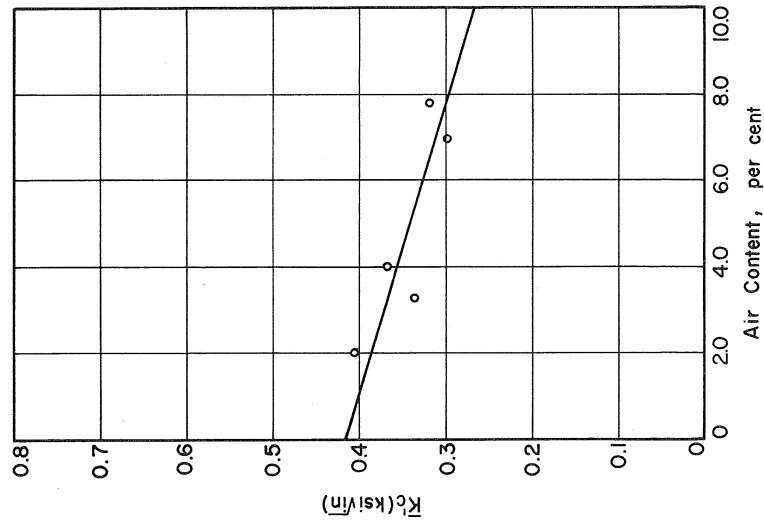
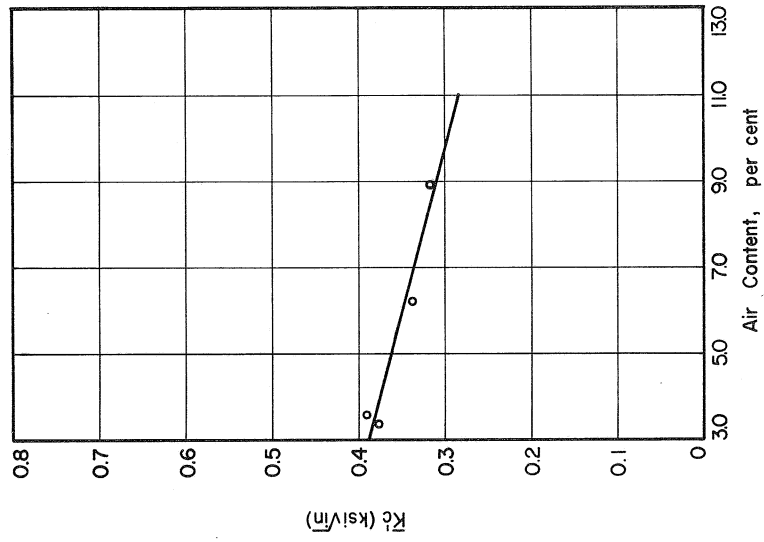


Fig. 96 Effect of w/c Ratio on  $K'_c$ : Mortars

Fig. 97 Effect of w/c Ratio on  $\bar{K}_c$ : ConcretesFig. 98 Effect of Air Content on  $\bar{K}_c$ : PastesFig. 99 Effect of Air Content on  $\bar{K}_c$ : Mortars

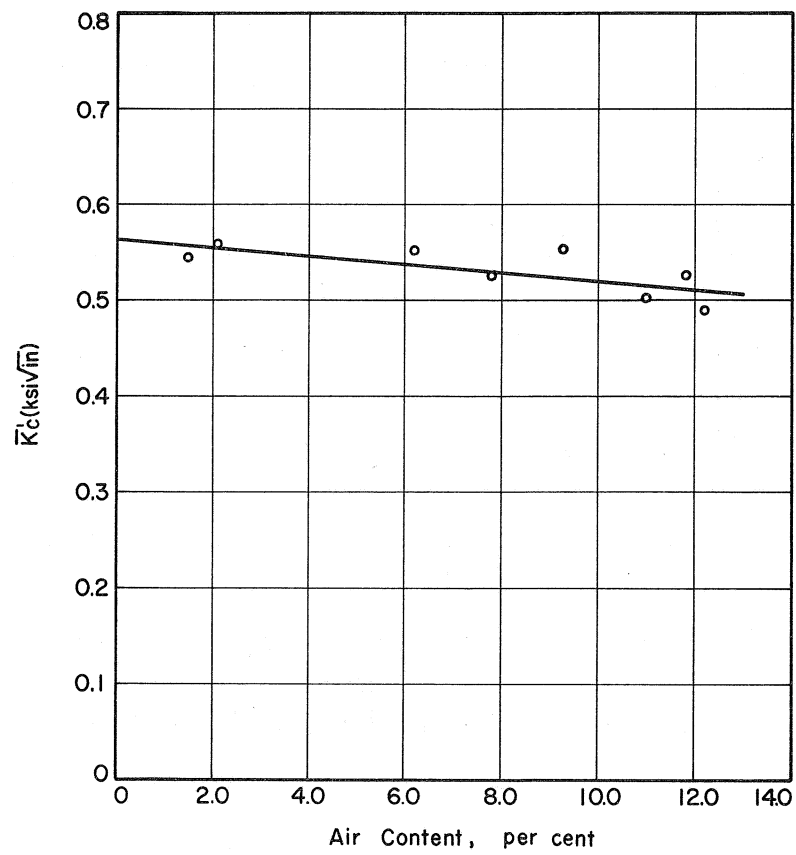


Fig. 100 Effect of Air Content on  $\bar{K}_c'$ : Concretes

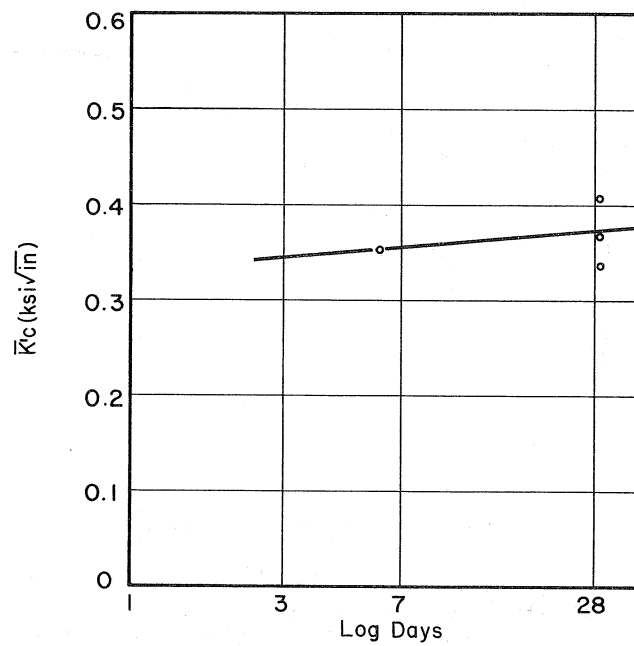


Fig. 101 Effect of Curing Time on  $\bar{K}_c'$ : Pastes

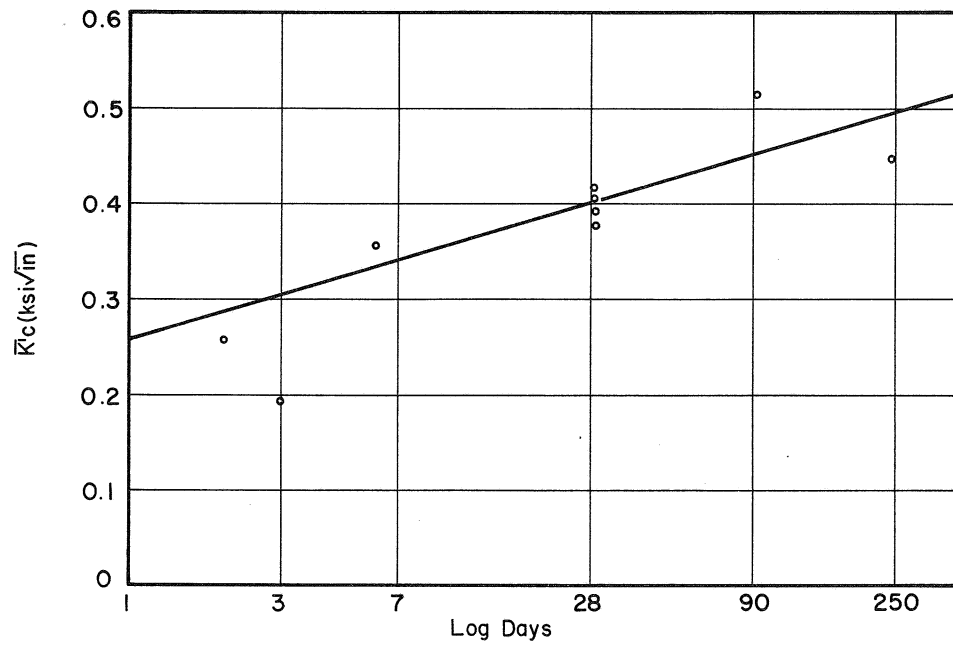


Fig. 102 Effect of Curing Time on  $\bar{K}'_c$ : Mortars

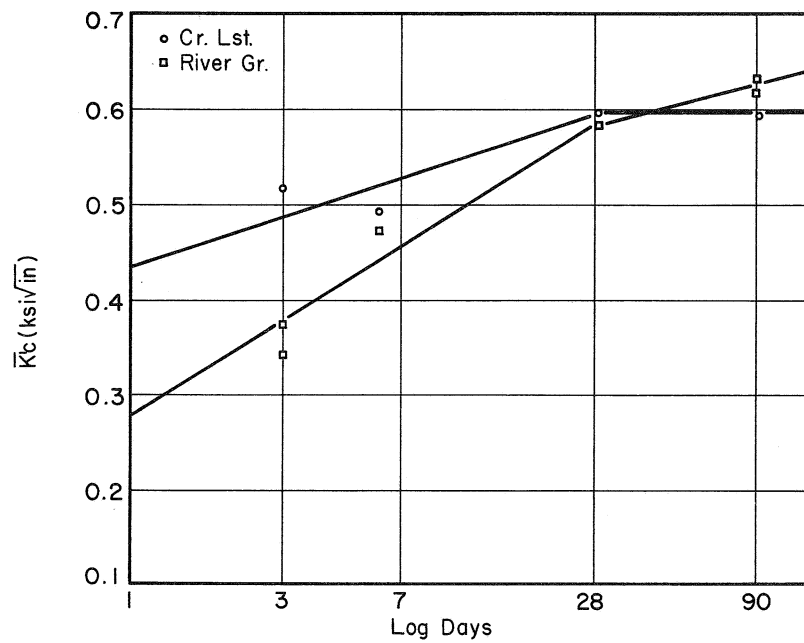


Fig. 103 Effect of Curing Time and Type of Coarse Aggregate on  $\bar{K}'_c$ : Concretes

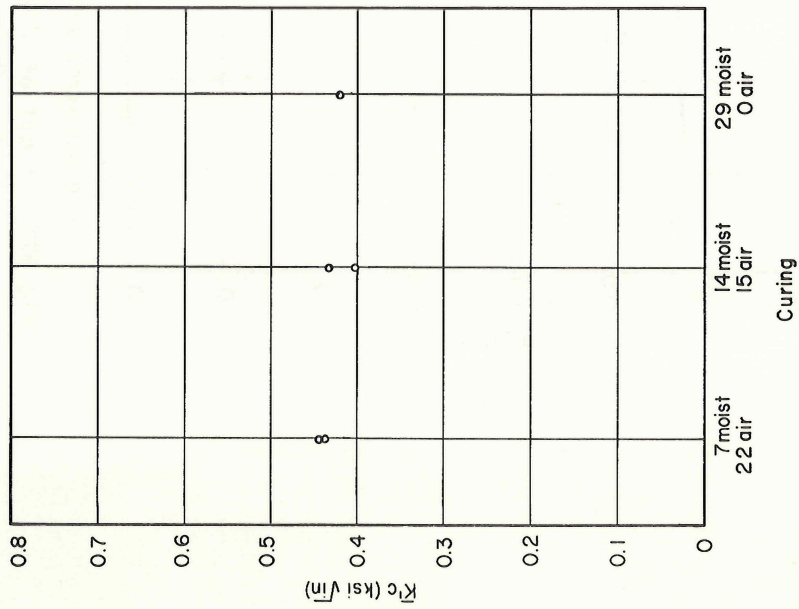


Fig. 104 Effect of Curing Conditions on  $K'_c$ : Mortars

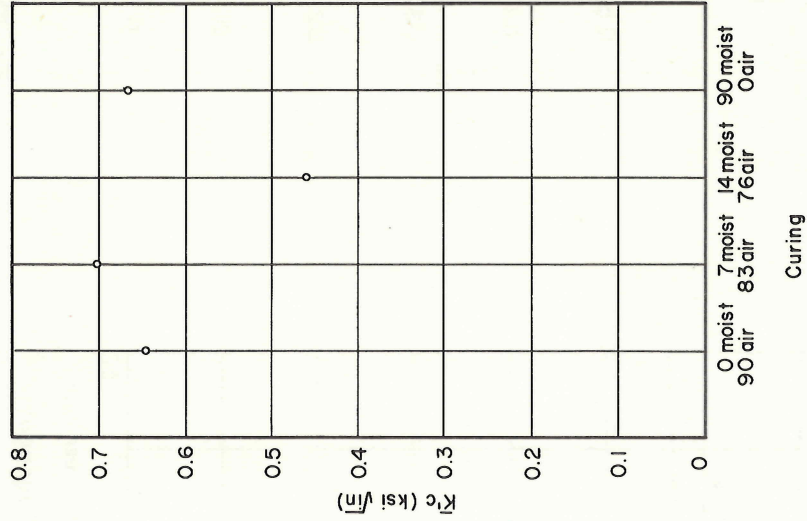


Fig. 105 Effect of Curing Conditions on  $K'_c$ : Concretes

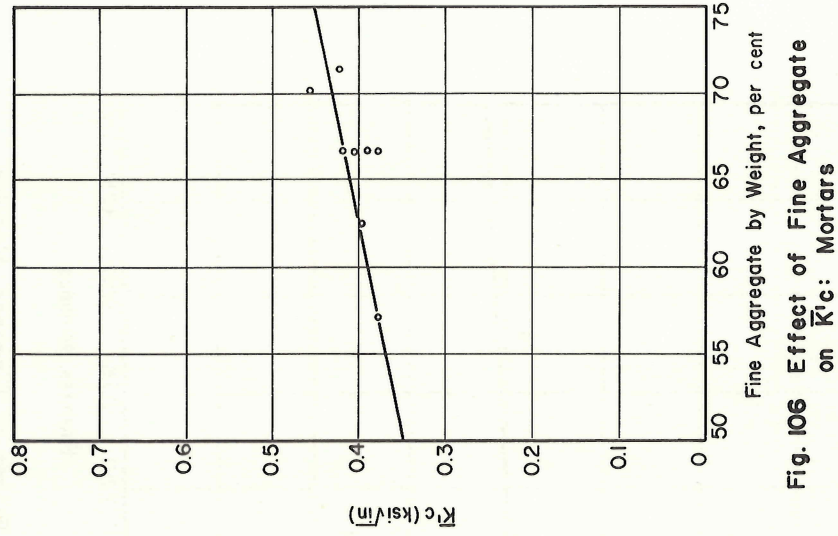


Fig. 106 Effect of Fine Aggregate on  $K'_c$ : Mortars



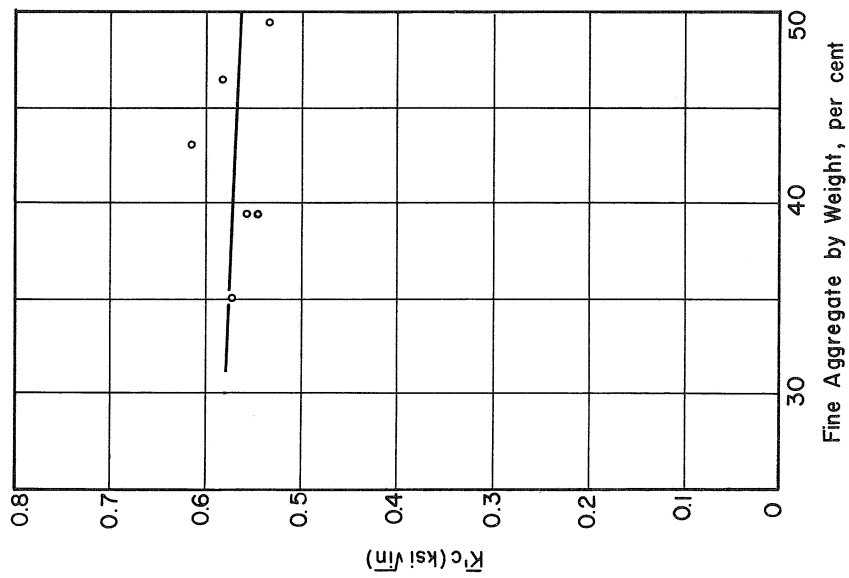


Fig. 107 Effect of Fine Aggregate on  $K'c$ : Concretes

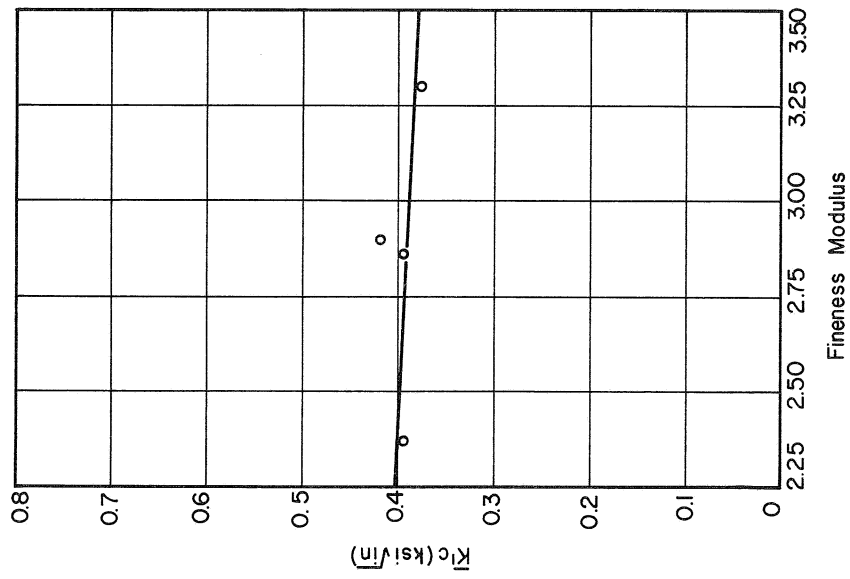
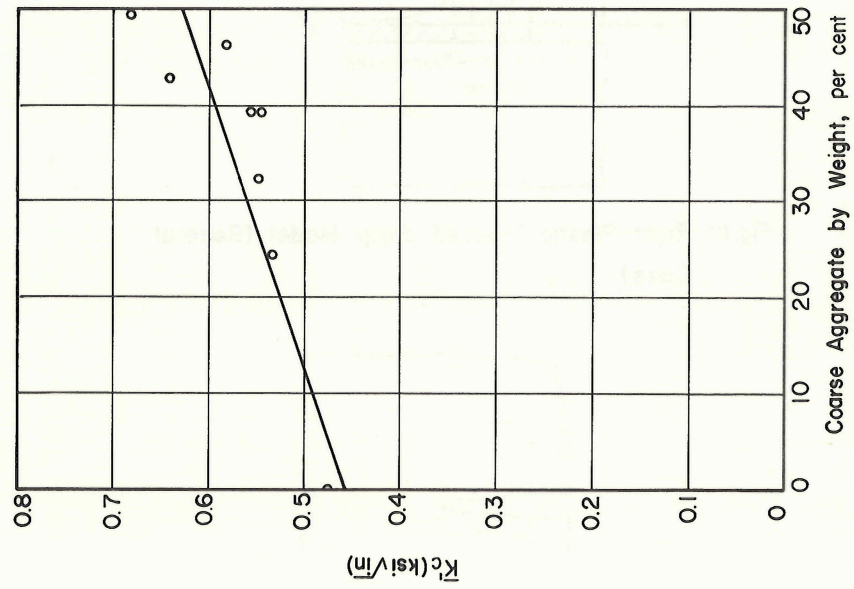
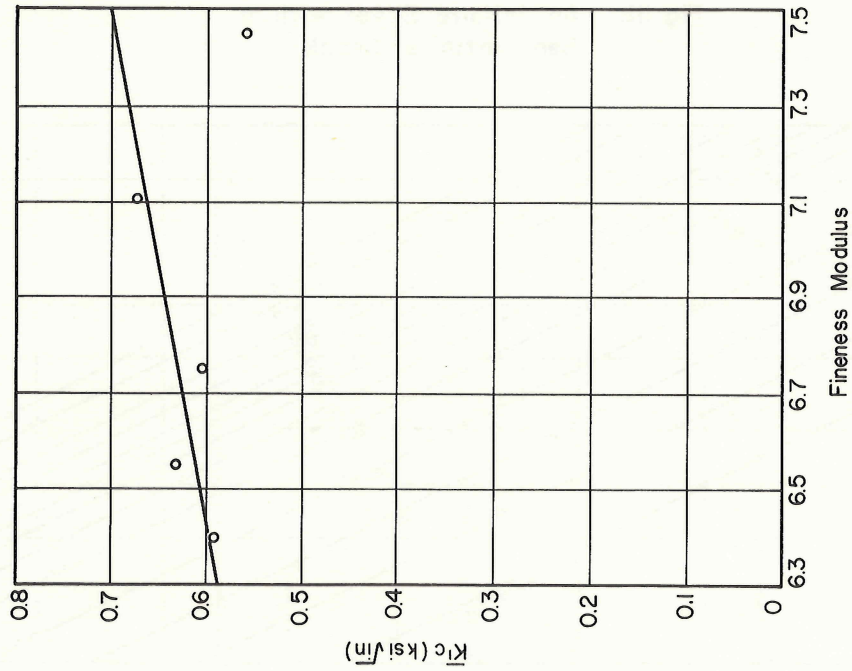


Fig. 108 Effect of Fineness Modulus of Sand on  $K'c$ : Mortars

Fig. 110 Effect of Coarse Aggregate on  $\bar{K}'_c$  ConcretesFig. 109 Effect of Fineness Modulus of Coarse Aggregate on  $\bar{K}'_c$  Concretes

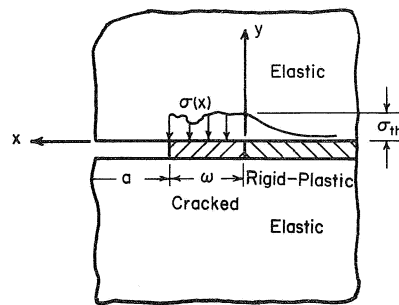


Fig. III Rigid-Plastic Cracked Strip Model (General Case)

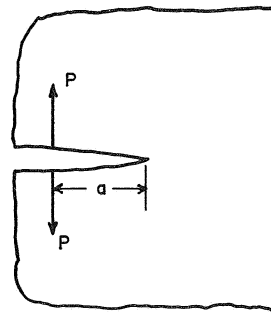


Fig. II2 An Infinite Sheet with a Semi-infinite Crack

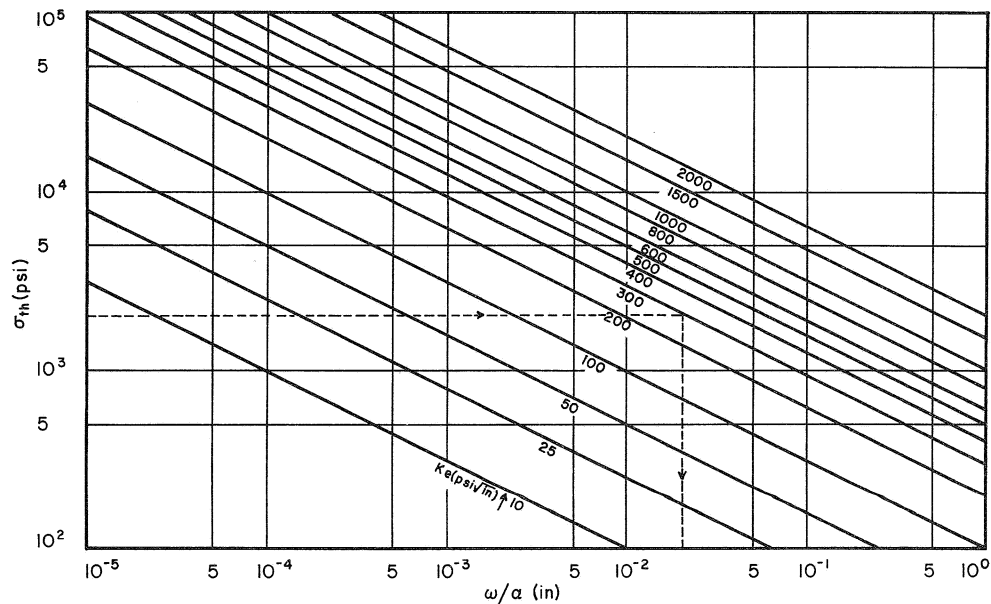


Fig. II3 Ratio of Plastic Zone Length to Stress Distribution Constant as a Function of Threshold Stress and Elastic Stress Intensity Factor

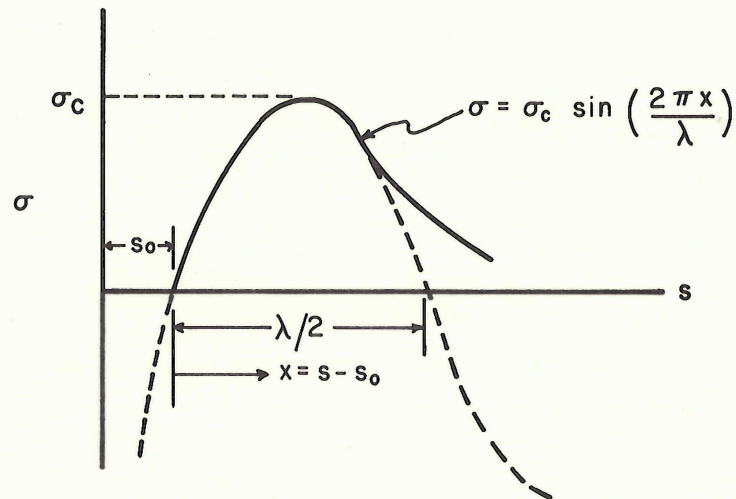


Fig. 114 Tensile Stress Required to Separate Gel Particles to a Distance  $s > s_0$

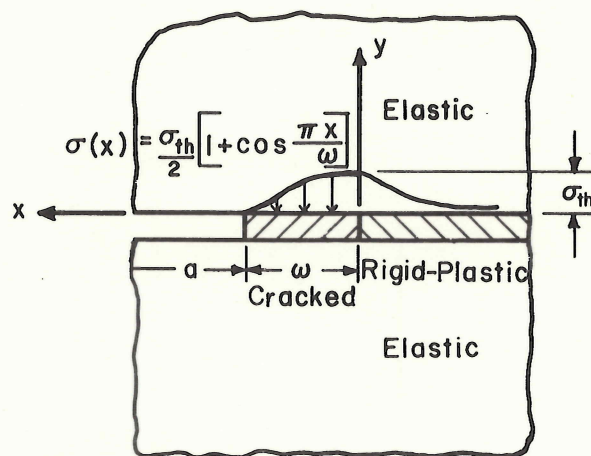


Fig. 115 Model for Fracture of Cement Paste